Technische Universität Braunschweig

emg

Jan Henrik Dieckhoff

Magnetic Nanoparticles in Rotating Magnetic Fields

Dissertation
Braunschweig 2015

Berichte aus dem **Institut für Elektrische Messtechnik und Grundlagen der Elektrotechnik** Band **52**

Hrsg. Prof. Dr. Meinhard Schilling

Magnetic Nanoparticles in Rotating Magnetic Fields

Von der Fakultät für Elektrotechnik, Informationstechnik, Physik
der Technischen Universität Carolo-Wilhelmina zu Braunschweig

zur Erlangung des Grades eines Doktors
der Ingenieurwissenschaften (Dr.-Ing.)

genehmigte Dissertation

von:	Jan Henrik Dieckhoff
aus:	Kassel

eingereicht am:	19.06.2015
mündliche Prüfung am:	27.11.2015

Referent:	Prof. Dr. Meinhard Schilling
Referent:	Prof. Dr. Andreas Hütten
Vorsitzender:	Prof. Dr. Erwin Peiner

2016

Dissertation an der Technischen Universität Braunschweig,
Fakultät für Elektrotechnik, Informationstechnik, Physik

Abstract

In this work, the rotational dynamics of magnetic nanoparticles (MNPs) in a size range from 12 nm to more than 100 nm was investigated with respect to its application in rotating magnetic field-based homogeneous bioassays. This concept enables the direct quantitative detection of proteins in solution, which is a promising technique owing to the increasing need for patient-side laboratory diagnostics.

A fluxgate-based measurement system was developed, which detects the stray field of the MNP sample magnetization induced by a rotating magnetic field (RMF). The gradiometric arrangement of two fluxgate magnetometers facilitates even outside a magnetically shielded environment a robust magnetic detection of various MNP types. The performance of the measurement system was characterized with different reference samples. For instance, iron oxide nanoparticle samples with iron concentrations below 0.005 g/L could be detected. For the analysis of the rotational dynamics, the phase lag between the rotating magnetic field and the MNP sample magnetization was calculated. This physical quantity enables in the investigated concentration range a particle concentration-independent characterization of the dissolved MNPs, for example the determination of their hydrodynamic size.

An accurate description of the measurement results for all field frequencies and amplitudes was given by a numerical solution of the Fokker-Planck equation, which is the basic equation for the description of the magnetization dynamics of a MNP ensemble in magnetic fields including thermal agitation. An empirical model derived from these results was discussed and applied for the evaluation of the RMF bioassay concept, which relies on the change of the phase lag caused by proteins specifically bound to the particle surface.

Measurements on various spherical and rod-shaped MNPs with single- and multi-cores matched perfectly with simulations based on the presented theory and were supported by additional characterization techniques, for example photon correlation spectroscopy and static magnetization measurements. Experiments with spherical single-core iron oxide nanoparticles dominated by the Brownian relaxation and conjugated with protein G demonstrated

the feasibility of the quantitative protein detection based on the RMF concept. For this single-core particle type a core diameter of 30 nm was found to be optimal since its dynamics is significantly affected by small proteins bound to the surface but it is still clearly dominated by the Brownian relaxation. Multi-core particles with a larger hydrodynamic size and partly dominated by the Néel relaxation process were less suitable for the direct detection of proteins in solution when avoiding cross-linking effects. Finally, measurements on streptavidin functionalized single-core particles demonstrated the principle quantitative analysis of samples containing the biomedical relevant biomarker HER2.

Symbols

$a_{n,m}$	temporal coefficient of spherical harmonics
a_s	distance to sample
A_a	system parameter of autocorrelation function
A_opt	optical absorbance
b	light path length in sample
B	magnetic flux density
B'	real part of magnetic flux density
B''	imaginary part of magnetic flux density
B_a	system parameter of autocorrelation function
B_M	magnetic flux density of measured stray field
B_S	magnetic flux density of MNP stray field
B_R	magnetic flux density of residual RMF component
c	concentration
c_0	initial concentration
C	Brownian time constant correction term
C_coil	capacity of Helmholtz coil
C_Curie	Curie constant
d	diameter
D	particle diffusion coefficient
DF	dilution factor
d_c	core diameter
d_h	hydrodynamic diameter
d_SD	single domain core diameter
d_spm	superparamagnetic core diameter
E_K	anisotropy energy
E_pot	potential energy
E_th	thermal energy
f	density distribution function
f_c	characteristic frequency
g	geometric factor of stray field coupling
G_a	autocorrelation function
H	magnetic field strength

H_0	DC magnetic field strength
H_c	coercive field
H_e	effective field
H_par	parallel component of magnetic field
H_perp	perpendicular component of magnetic field
H_S1	magnetic field of Helmholtz coil S1
H_S2	magnetic field of Helmholtz coil S2
I	luminous intensity
I_coil	coil current
I_comp	compensation current
I_exc	excitation current
I_R	intensity of Rayleigh scattering
I_0	intensity of incident light
k	fraction of Néel relaxation dominated particles
k_B	Boltzmann constant
k_coil	coil constant
K_a	association constant
K_eff	effective anisotropy constant
L	Langevin function
L_coil	inductance of Helmholtz coil
L_h	hydrodynamic length of rod shaped particle
m	magnetic moment
m_P	molecular mass of protein
M	magnetization
M'	real part of magnetization
M''	imaginary part of magnetization
M_∞	magnetization after infinite magnetization time
M_r	remanent magnetization
M_rel	magnetization relaxation
M_s	saturation magnetization
M_0	equilibrium magnetization
n	particle number density
N_coil	number of coil windings
N_cov	number of receptor proteins on MNP
n_r	refractive index
$P_n^{\lvert m\rvert}$	Legendre function
q	scattering vector
r	protein-to-MNP ratio

r_{coil}	middle Helmholtz coil radius
F	distance to particle
R_{coil}	resistance of Helmholtz coil
$Ref^{\star}$	frame of reference
S	physical measurement quantity in logistic function
S_{low}	minimum measurement quantity in logistic function
S_{high}	maximum measurement quantity in logistic function
S_{xy}	cross-spectral density
s_{x}	standard deviation of variable x
t	time
t_{mag}	magnetization time
T	particle temperature
T_B	blocking temperature
T_{env}	environment temperature
T_{SH}	sample holder temperature
u	standard uncertainty
u_{c}	combined standard uncertainty
u_{e}	expanded standard uncertainty
U_{in}	input voltage
U_{out}	output voltage
V_{c}	core volume
V_{h}	hydrodynamic volume
W	distribution function
$\bar{x}$	mean value of variable x
$\tilde{x}$	median value of variable x
Z_{coil}	absolute coil impedance
α	slope parameter of logistic function
α_{T}	tilt angle
$\Delta\varphi$	phase lag change
ΔE_{crit}	critical energy barrier
ε	molecular extinction coefficient
ζ	dimensionless effective field
η	dynamic viscosity
θ	measurement angle of Rayleigh scattering
Θ	angle between particle easy axis and magnetization
λ	wavelength
λ^{*}	modified interaction parameter
μ	location parameter of log-normal distribution
μ_0	vacuum permeability

μ_r	relative permeability
ξ	Langevin parameter
ϱ_P	protein density
σ	scale parameter of log-normal distribution
$\tau^\star$	delay time
τ_0	attempt period of the Néel time constant
τ_B	Brownian time constant
$\tau_\mathrm{B,H}$	field dependent Brownian time constant
$\tau_\mathrm{B,rod}$	Brownian time constant of rod shaped particle
τ_d	mechanical torque
τ_eff	effective time constant
$\tau_\mathrm{eff,H}$	field dependent effective time constant
τ_m	magnetic torque
τ_N	Néel time constant
$\tau_\mathrm{N,H}$	field dependent Néel time constant
ϕ	volume fraction of solid phase in solution
φ	phase lag
φ_H	phase position of RMF vector
φ_M	phase lag of measured signal
φ_R	phase lag of residual field component
Φ	angle between magnetic field and particle easy axis
χ	susceptibility
χ'	real part of susceptibility
χ''	imaginary part of susceptibility
χ_0	DC susceptibility
χ_1	field-dependent DC susceptibility
ω	angular frequency
ω_p	single particle angular velocity
Ω	angular velocity of whole suspension

Nomenclature

ACS	AC susceptibility
ACF	AC field
BSA	bovine serum albumin
CMSM	cluster moment superposition model
CRP	C-reactive protein
DLS	dynamic light scattering
ELISA	enzyme-linked immunosorbent assay
FFT	fast Fourier transform
FPE	Fokker-Planck equation
HRP	horseradish peroxidase
HRTEM	high resolution transmission electron microscopy
MARIA	magnetic relaxation immunoassay
MC	multi-core
MD	multi-domain
MNP	magnetic nanoparticle
MOSFET	metal oxide semiconductor field-effect transistor
MPI	magnetic particle imaging
MPMS	magnetic property measurement system
MRI	magnetic resonance imaging
MRX	magnetorelaxometry
MSM	moment superposition model
PCCS	photon cross-correlation spectroscopy
PCS	photon correlation spectroscopy
PI	proportional-integral
PVC	polyvinyl chloride
RMF	rotating magnetic field
R	receptor
RT	product of receptor and target
RTSI	real time system integration
S1	small Helmholtz coil
S2	large Helmholtz coil
SC	single-core

SD	single-domain
SEM	scanning electron microscopy
SNR	signal-to-noise ratio
SP	superparamagnetic
SPI	serial peripheral interface
SQUID	superconducting quantum interference device
SVD	singular value decomposition
T	target
TEM	transmission electron microscopy

Contents

Introduction

The combination of magnetic properties and a geometrical structure in the nanometer range results in some unique properties which make magnetic nanoparticles (MNPs) so interesting for science and practical applications. Although a lot of research was conducted in this field since the publication of Louis Néel's and William Fuller Brown's fundamental contributions for the understanding of fine magnetic particles [1, 2], still basic questions regarding their dynamic magnetic properties and their impact on practical applications exist, e.g. in the biomedical field.
In the project NAMDIATREAM, which is funded by the European Commission, magnetic nanoparticles are applied as **na**notechnological toolkits for **m**ulti-modal disease **dia**gnostics and **trea**tment **m**onitoring. One particular technology platform aims at the investigation and realization of a homogeneous bioassay concept for a high-sensitive optical biomolecule detection based on the magnetic manipulation of rod-shaped MNPs in rotating magnetic fields [3]. This point-of-care testing [4] is intended to satisfy the increasing need for patient-side laboratory diagnostics and supports an early disease detection as well as an effective therapy monitoring, which play a crucial role in our aging society. The homogeneous bioassay concept benefits from the direct detection of the biomolecules in solution, which requires no washing steps as it is often necessary for indirect detection methods, e.g. in the enzyme-linked immunosorbent assay (ELISA). Due to this simplicity it is also described as a mix and measure principle.
Magnetic nanoparticles are well applicable for this concept since they can be functionalized with specific biorecognition elements binding the biomolecules of interest. This interaction can be transduced into an analyzable signal by manipulating the particles with a magnetic field and measuring their response. The magnetic manipulation of the MNPs can be realized with various types of magnetic fields. For instance, switched magnetic fields are utilized in the case of magnetorelaxometry [5, 6] and alternating magnetic fields featuring one or more frequencies enable AC susceptibility based bioassays [7, 8, 9, 10]. The manipulation with a rotating magnetic field represents a comparable new approach which was so far only applied to realize

bioassays based on magnetic particles in the upper nanometer and the micrometer size range [11, 12] or to investigate the induced magnetic particle interactions [13] and the impact on highly concentrated ferrofluids [14].
Throughout this work the dynamic response of magnetic nanoparticles to rotating magnetic fields was investigated, which can be characterized by the occurring phase lag between the magnetization of the nanoparticle ensemble and the rotating magnetic field. Furthermore, adequate physical models for the analysis of the measurement results and the applicability of the concept for the direct detection of biomolecules in solution were studied. Since the rod-shaped nanoprobes for an optical detection had to be designed, synthesized and established during the project, a reference system based on a magnetic detection was required for the investigation of the rotational dynamics with reference particles. A detailed description of this system can be additionally found in the present work.
In **chapter 1** the fundamentals of magnetic nanoparticles with respect to their application, structure and especially their dynamics are described. In addition, the utilized characterization techniques are introduced and the term bioassay with a focus on magnetic nanoparticles and the applied principles is explained. After the definition of the rotating magnetic field (RMF) in **chapter 2**, theories describing the rotational dynamics of MNPs in a RMF are discussed. They range from a comparable simple mechanical model to the numerical solution of the Fokker-Planck equation, which is the basic equation for the description of the dynamics of the magnetization of an ensemble of MNPs in magnetic fields including thermal agitation. An empirical model derived from this equation is discussed and the basis of further simulations. The developed reference system based on fluxgate magnetometers for the detection of the MNP dynamics in a RMF is presented in **chapter 3**. This includes a detailed description of the system's single components, e.g. the field excitation unit and the sensors, the applied software and control concept as well as a characterization of the system's performance and errors based on measurements and simulations. **Chapter 4** deals with the measurement results of the RMF system for different magnetic nanoparticle systems. For instance, the results of spherical iron oxide single-core particles in the range of 25 nm to 40 nm and larger multi-core or rod-shaped particles are illustrated. A comparison with additional characterization techniques is carried out and the influence of the particle and environmental parameters on the RMF results is discussed. Finally, the detection of biomolecules in solution based on the RMF concept is presented with spherical MNPs and two biological test systems. On the basis of these

results, the quantitative detection and the influence of the particle systems and the binding reaction are examined. As an outlook, the quantitative detection of a medical relevant biomolecule is demonstrated.

1 Fundamentals

This chapter describes the fundamentals that are essential for the understanding of this work. First, the basic concepts of magnetic nanoparticle structure, synthesis and dynamics are introduced. This includes the description of the magnetization effects of single particles and particle ensembles. In addition, characterization methods, which are applied in this work for the independent determination of the particle parameters, are explained. Finally, a review about bioassays is given, the final application of this research.

1.1 Magnetic Nanoparticles

The basic structure of a magnetic nanoparticle (MNP) consists of a magnetic core in the nanometer range with a magnetic moment m and a protective shell with a thickness of some nanometers around the core. The core size is defined by the core volume V_c and the hydrodynamic size by the volume of core plus shell, the so called hydrodynamic volume V_h. For spherical particles the corresponding core and hydrodynamic diameter d_c and d_h can be used equivalently. The magnetic moment of the particle is specified as for any magnetic material by the material-dependent saturation magnetization M_s and the corresponding volume V_c:

$$m = M_\mathrm{s} V_\mathrm{c}. \tag{1.1}$$

Magnetic particles with a core diameter in the lower nanometer range are affected by finite-size effects. The two dominant effects are the superparamagnetism and the single-domain structure. In addition, surface effects become more important because more atoms of the magnetic core are surface ones, which can result in a surface anisotropy. These effects are explained in detail in the following sections. The purpose of the particle shell is to protect the magnetic core from aging, prevent the MNPs from agglomeration,

stabilize them in the surrounding media and enable a linking of different functional molecules. Fig. 1.1 displays, as an example, single-core MNPs whose magnetic moments are represented by red arrows. The gray zigzag lines depict a protective polymer shell. It is linked with antibodies, that can bind specifically proteins in the surrounding media. Due to the similar size range of proteins and MNPs the latter are still measurably affected in size by bound proteins.

1.1.1 Applications

The linking of functional molecules and the existence of a magnetic moment in combination with the finite-size and surface effects are the key characteristics of a MNP that facilitate various unique applications, especially in the biomedical field [15]. The magnetic separation is today one of the standard methods for the efficient extraction of biological substances from complex media [16, 17, 18], e.g. the collection of antibodies from serum. Magnetic drug targeting offers the possibility to deliver magnetically labeled drugs to a specific organ in the body by the application of magnetic field gradients [19]. This approach can even be combined with an imaging of the delivery process due to the contrast agent functionality of MNPs in magnetic resonance imaging (MRI) [20, 21] and a controlled drug release by the application of thermosensitive polymers [22]. In the cancer treatment magnetic hyperthermia is a promising approach. In the tumor region locally injected MNPs destroy the cancer cells via heat generation induced by an alternating magnetic field [23, 24]. As a new diagnostic in vivo application the magnetic particle imaging (MPI) is investigated [25]. In contrast to MRI the magnetic particles themselves are the source of the imaging signal. The physical detection principle enables in vivo real-time imaging of the magnetic particle distribution with positive contrast and significantly higher temporal resolution compared to MRI [26, 27]. In the field of in vitro diagnostics, e.g. bioassays for the quantification of proteins in biological media, magnetic nanoparticle based approaches were intensively studied and still attract researchers' focus. Especially, homogeneous bioassays based on MNPs as a direct magnetic label [28, 7] can satisfy the need for point-of-care diagnostics [4]. A detailed explanation of different bioassays can be found in section 1.3.

Besides the biomedical applications of magnetic nanoparticles several other technical ones exist. In these cases the term ferrofluid is frequently used, which describes an ensemble of highly concentrated MNPs in aqueous or oily

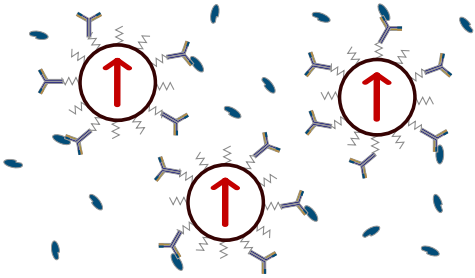

Figure 1.1: Single-core magnetic nanoparticles in solution, functionalized with antibodies and specifically bound to antigens.

media. Ferrofluids can be exploited as seals, dampers and heat transporters in pumps [29, 30] or loudspeakers [31]. Further uses are the investigation of energy harvesting approaches [32] or the recovery of enzymes in catalytic reactions [33].

1.1.2 Synthesis, stability, functionality

The magnetic materials that MNPs consist of are the elements cobalt, nickel and iron, alloys or oxidic compounds. The most common used magnetic nanoparticles in biomedicine to date are iron oxide MNPs [34] due to their biocompatibility, non-toxicity and relatively well-established synthesis processes. Fine iron oxide nanoparticles can be even found in different organisms, e.g. magnetotactic bacteria [35]. Iron oxide material exists in one of four phases: Wüstite (FeO), hematite (α-Fe_2O_3), maghemite (γ-Fe_2O_3) and magnetite (Fe_3O_4). Since wüstite and hematite show an antiferromagnetic or weakly ferromagnetic behavior at room temperature, magnetite and maghemite are the favorable phases. Iron oxide MNPs for biomedical applications are commonly synthesized with chemical procedures. The synthesis of iron oxides from aqueous Fe^{2+} and Fe^{3+} salts in a highly basic solution under inert atmosphere, the so called co-precipitation, is a convenient process [36, 34]. A better control of the particle size and shape, especially for small nanoparticles, can be achieved with the thermal decomposition of iron-oleate [37]. An comprehensive overview of different synthesis approaches for iron oxide nanoparticles is given by Laurent et. al. [34]. The experimentally determined saturation magnetizations of magnetite nanoparticles were found to be lower than the bulk literature value of 480 kA/m [36, 38], which

can be explained by the existence of biphasic particles or magnetic dead layers [39]. The deployment of a pure magnetic element or another alloy, e.g. cobalt iron oxide [40], would result in a significantly increased M_s [41]. For instance, cobalt exhibits a M_s of 1446 kA/m, which is more than three times higher. However, biocompatibility and toxicity problems as well as difficult stabilization and conjugation processes can hinder the synthesis or application. Another aspect that can be influenced by the synthesis process is the particle shape. Besides a spherical geometry, different other shapes are possible. For instance, cubic iron oxide [36, 34] and elongated cobalt [42, 43] as well as nickel [44] particle protocols are established.

Fig 1.2 illustrates that a magnetic nanoparticle does not necessarily consist of only one single-core. So called multi-core particles, which contain a cluster of several magnetic nanocrystals, are available from the lower nanometer range up to several micrometers [45]. These particles possess a reduced magnetic moment in relation to the material's saturation magnetization due to the interaction of the nanocrystals [46]. A further surface modification of the particles results in a shell or coating which is essential for the MNP stability. Attractive forces such as the van der Waals force and the magnetic dipole-dipole interaction, which let the particles agglomerate, have to be in equilibrium with the repulsive forces as the steric and electrostatic repulsion. Here, various compounds have been applied as coatings. The most common ones are monomeric stabilizers like carboxylates, phosphates and sulfates, inorganic materials like silica or gold as well as polymers like dextran, polyethylene glycol (PEG) or polyvinyl alcohol (PVA) [34, 47]. In some cases the coating even affected the magnetic properties, for instance, paramagnetic particles became ferromagnetic [48]. In order to give MNPs the functionality to interact specifically with their environment, they need to be conjugated with specific molecules. Different interaction systems exist in biomedicine: Antibody-antigen, avidin-biotin, DNA-DNA or ligand-receptor. In all cases a strategy for the coupling of one of the specific biomolecules to the MNP is necessary. This can range from electrostatic interactions to covalent bonds. An overview about different conjugation strategies was given by Kozissnik et al. [49].

Regarding the stability of suspended MNPs, different stabilization criteria exist which have first been formulated during the development of technical ferrofluids [50]. They deal with the stability in a magnetic gradient field, prevention of agglomeration induced by magnetic dipole-dipole interactions or van der Waals forces or the hindrance of sedimentation caused by the gravitational field. For a typical ferrofluid in water at room temperature

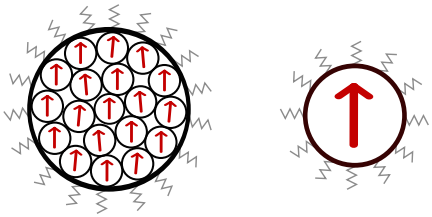

(i) (ii)

Figure 1.2: Multi-core (i) and single-core (ii) nanoparticles with protective polymer shell (gray lines) and magnetic moment (red arrow).

the hydrodynamic diameter which prevents the particles from sedimentation was calculated to be smaller than 12 nm [48]. The influence of the dipole-dipole interactions in relation to the particle thermal energy $E_{\mathrm{th}} = k_{\mathrm{B}}T$ can be estimated by the modified interaction parameter λ^* which is defined as [51]

$$\lambda^* = \frac{\mu_0 M_{\mathrm{s}}^2 \pi d_{\mathrm{c}}^3}{148 k_{\mathrm{B}} T} \frac{d_{\mathrm{c}}^3}{d_{\mathrm{h}}^3} \tag{1.2}$$

with the vacuum permeability μ_0, the Boltzmann constant k_{B} and the temperature T. An interaction parameter $\lambda^* \gg 1$ indicates a non-negligible magnetic particle interaction. For instance, an iron oxide MNP with a 12 nm core diameter, an additional shell with a thickness of 3 nm and a M_{s} of 480 kA/m yields at 300 K room temperature an interaction parameter of 0.76.

1.1.3 Nanomagnetism

The size reduction of a ferromagnet down to the nanometer regime results in the disappearance of the domain walls because surface energies, e.g. the domain wall energy, become more significant than the volume energies, e.g. the demagnetization energy. Finally, a single magnetic domain is energetically more favorable and the formation of single-domain (SD) nanoparticles at a distinct size is caused [52].

Magnetic anisotropy

The magnetization of a nanoparticle commonly favors one or more alignments inside the particle core due to the existence of energetically favorable states which are described by the anisotropy energy E_K. This magnetic anisotropy originates from different particle properties. For a MNP the main ones are the crystal and the shape anisotropy [53]. However, surface and exchange anisotropies can also contribute [54]. A domination of the shape anisotropy frequently causes an alignment of the magnetization along one axis, which is also referred to as the easy axis. The two possible orientations along the axis are consequently separated by the anisotropy energy. The corresponding energy E_K of such an uniaxial MNP anisotropy is represented by

$$E_\mathrm{K}(\Theta) = K_\mathrm{eff} V_\mathrm{c} \sin^2(\Theta) \tag{1.3}$$

with the effective anisotropy constant K_eff and the angle Θ between the easy axis and the magnetization. In the presence of a constant magnetic field H oriented at an angle Φ with respect to the easy axis (see Fig. 1.3(i)), the magnetization rotates and the anisotropy energy changes according to

$$E_\mathrm{K}(\vartheta) = K_\mathrm{eff} V_\mathrm{c} \sin^2(\Theta) - \mu_0 V_\mathrm{c} H M_\mathrm{s} \cos(\Theta - \Phi). \tag{1.4}$$

This equation, which describes the anisotropy energy of a single-domain particle possessing a coherent domain rotation in the presence of a magnetic field, is attributed to the Stoner-Wohlfarth model [52]. Fig. 1.3 (ii) illustrates the uniaxial anisotropy energy as a function of the angle Θ and in the absence of a magnetic field. The two similar energy minimums depict the two orientations along the easy axis. Thus, none of these two orientations is energetically favorable. However, under the action of a positive (Fig. 1.3 (iii)) or negative (Fig. 1.3 (iv)) magnetic field parallel to the easy axis the magnetization orientation in the direction of the field is favored. This originates from the absolute difference of the energy minimums at 0° and 180°. For non-parallel configurations of H and the easy axis energy minimums at other Θ can occur, especially for stronger magnetic fields [55]. Finally, this approach enables the calculation of a single-domain particle's magnetization curve and it explains why such a particle can possess a hysteresis (Fig. 1.4) although no irreversible effects originating from domain-wall pinning

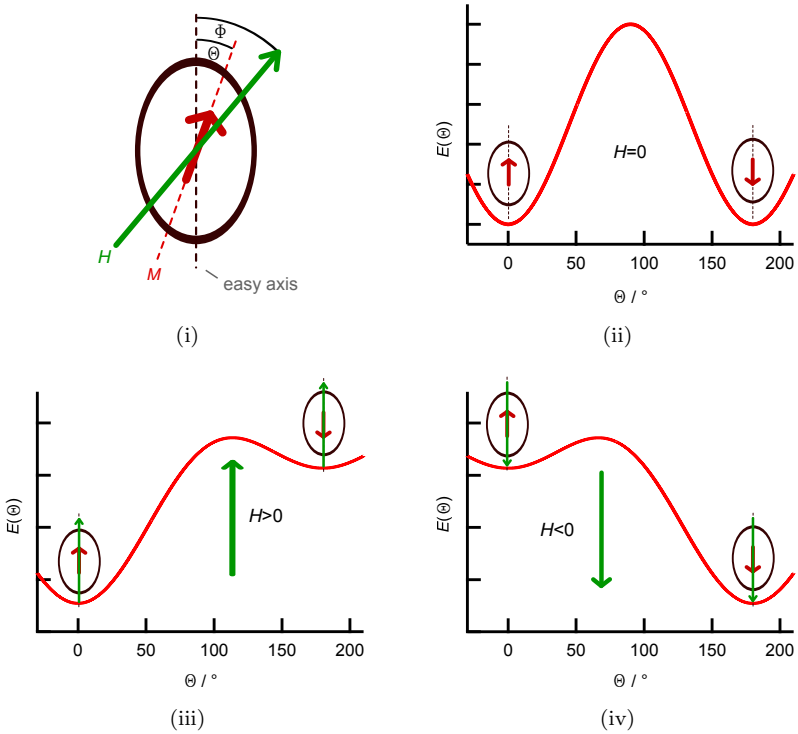

Figure 1.3: (i) Definition of the angles Φ and Θ for an MNP with uniaxial magnetic anisotropy in a magnetic field. (ii) Resulting anisotropy energy in the absence of a magnetic field as a function of Θ. In the presence of a magnetic field applied at an angle $\Phi = 0°$ to the easy axis only one global minimum exists: For a positive field (iii) at $\Theta = 0°$ and a negative field (iv) at $\Theta = 180°$.

exist. In the following subsections we assume an uniaxial anisotropy for the described MNPs.

Superparamagnetism

The hysteresis of a single-domain nanoparticle's magnetization curve vanishes with a further size reduction. Thus, the magnetization curve of an ensemble of such particles is represented by a single sigmoid function without a coercive field H_c and remanent magnetization M_r (Fig. 1.4). This regime is referred to as superparamagnetic. This term was first introduced by Bean and Livingston [56]. It is a consequence of the reduced anisotropy energy barrier between the two magnetization orientations (Fig. 1.3 (ii)) which shrinks in comparison to the thermal energy E_{th}. Thus, a flipping of the magnetization from one orientation to the other can be induced by the thermal energy and the nanoparticle acts like a paramagnet, however, with a significantly higher magnetic moment. Fig. 1.5 illustrates the nanoparticle coercivity as a function of the core diameter. Below the core diameter d_{spm} no coercivity exists, thus d_{spm} marks the upper superparamagnetic border. In the ferromagnetic regime the core diameter d_{SD} indicates the transition form a single-domain to a multi-domain (MD) nanoparticle. In addition, d_{SD} corresponds to the particle size which possesses the highest coercivity. This is a consequence of the increased anisotropy of a larger particle in the SD regime and the energetically more favorable domain-wall rotation in the MD regime. A rough estimation for magnetite nanoparticles [48] leads to a d_{spm} of 12.2 nm and a d_{SD} of 52.7 nm. For the classification of the superparamagnetic regime the blocking temperature T_B is frequently used. This temperature is related to the thermal energy which has to be exceeded in order to cross the energy barrier ΔE_{crit} and observe a change of the system's magnetization state in the given measurement time, a so called relaxation process. ΔE_{crit} is in the case of an uniaxial anisotropy and a measurement time of 100 s defined as [53]

$$\Delta E_{crit} = 25 k_B T_B = K_{eff} V_c. \tag{1.5}$$

As a second criterion for superparamagnetism, besides the absence of a hysteresis, the magnetization curves measured at different temperatures have to superimpose if plotted over the magnetic field normalized to the temperature H/T.

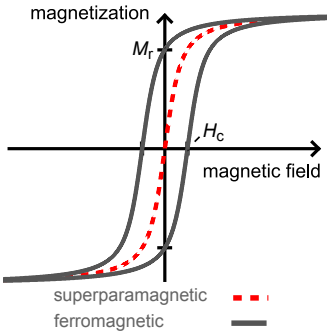

Figure 1.4: Magnetization curve of superparamagnet and ferromagnet. H_c and M_r denote the coercivity and the remanence.

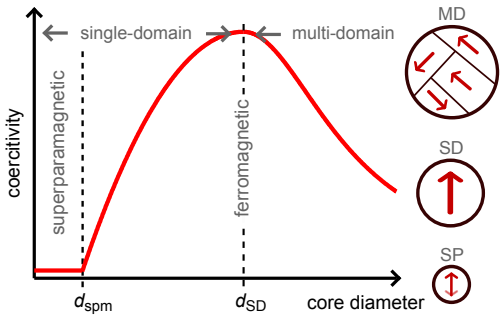

Figure 1.5: Dependency of coercivity on core diameter [57] for single- (SD) and multi-domain (MD) particles with classification of superpara- (SP) and ferro-/ferrimagnetic regimes.

Langevin function

The magnetization curve of an ensemble of magnetic nanoparticles expresses the magnetization's dependence on the applied magnetic field, the temperature and the particle core parameters d_c and M_s. As in the case of a paramagnet, the magnetization of an ensemble of noninteracting superparamagnetic particles can be described by the Langevin function $L(\xi)$, the particle magnetic moment m and the particle number density n:

$$M = nmL(\xi). \tag{1.6}$$

In addition, this approach is also valid for larger MNPs, which are suspended in a liquid, do align randomly in the absence of a magnetic field and do not interact with each other. In Fig 1.6 the Langevin function is plotted against the Langevin parameter ξ. The definition of $L(\xi)$ is

$$L(\xi) = \coth(\xi) - \frac{1}{\xi} \tag{1.7}$$

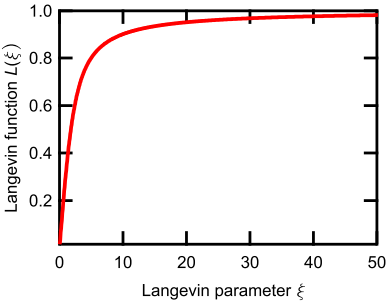

Figure 1.6: Langevin function $L(\xi)$ with dependence on Langevin parameter ξ.

with ξ representing the relation of magnetic to thermal energy:

$$\xi = \frac{\mu_0 m H}{k_\mathrm{B} T}. \tag{1.8}$$

Thus, the rise of the magnetization with respect to the magnetic field is increased by a higher magnetic moment and a lower particle temperature. The saturation value of the magnetization curve corresponds to the saturation magnetization M_s, which is a material-dependent property. The Langevin function can be approximated by $L(\xi) = \xi/3$ for $\xi \ll 1$ and $L(\xi) = 1 - 1/\xi$ for $\xi \gg 1$. In the case of small ξ values the rise of the Langevin function corresponds to the initial DC susceptibility χ_0.

Susceptibility

The susceptibility χ represents the relation of the sample's magnetization to the inducing magnetic field H:

$$M = \chi H \tag{1.9}$$

Thus, for a magnetizing static field, the initial DC susceptibility χ_0 is defined by

$$\chi_0 = \left.\frac{\delta M}{\delta H}\right|_{H=0}. \tag{1.10}$$

From these definitions Curie's law is derived as [52]

$$\chi_0 = \frac{n\mu_0 m^2}{3k_\mathrm{B}T} = \frac{C_\mathrm{Curie}}{T} \tag{1.11}$$

which explains the temperature dependence of a paramagnet with respect to the Curie constant C_Curie. It is important to note, that this relation is only valid for small fields and $\chi_0 \ll 1$. Otherwise the magnetic field in the sample is reduced by the induced magnetic moments' field and a deviation between the field inside and outside the sample arises. This phenomenon is named demagnetization and is taken into account by the demagnetization factor [58]. The magnetic flux density B of an ensemble of MNPs under the action of a magnetic field takes with Eq. 1.9 and the relative permeability μ_r of the given material the form

$$B = \mu_0 (H + M) = \mu_0 (1 + \chi) H = \mu_0 \mu_\mathrm{r} H. \tag{1.12}$$

Relaxation processes

The observable change of the magnetization state of an ensemble of MNPs towards an equilibrium state in a given measurement time is characterized as relaxation process. There exist two relaxation processes for a magnetic nanoparticle: The Brownian and the Néel relaxation. If a MNP is suspended in a liquid, capable to undergo Brownian motion and the particles' magnetic moments are thermally blocked ($T \ll T_\mathrm{B}$), then the MNPs are dominated by the Brownian relaxation. This process correlates with a rotation of the whole mobile particles in the liquid (see Fig. 1.7). The corresponding Brownian time constant τ_B is defined as

$$\tau_\mathrm{B} = \frac{3\eta V_\mathrm{h}}{k_\mathrm{B}T} \tag{1.13}$$

with the liquid's dynamic viscosity η. For MNPs with a non-spherical shape τ_B needs to be modified, because the rotational drag of a particle is shape dependent. For instance, based on a model by Tirado et al. [59] the time constant of a rod-shaped particle with the hydrodynamic length L_h and

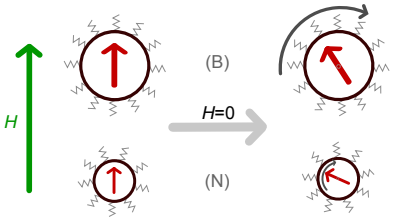

Figure 1.7: After an alignment of the particle moments along the magnetic field H, the particle magnetizations relax via the Brownian (B) or Néel (N) relaxation process.

diameter d_h can be expressed by

$$\tau_{\mathrm{B,rod}} = \frac{\pi\eta L_\mathrm{h}^3}{6k_\mathrm{B}T}\left[\ln(\frac{L_\mathrm{h}}{d_\mathrm{h}}) + C\right]^{-1} \tag{1.14}$$

with

$$C = -0.662 + 0.891\frac{d_\mathrm{h}}{L_\mathrm{h}}. \tag{1.15}$$

If the MNPs are immobilized or the magnetic moments are not thermally blocked, then the MNPs are dominated by the Néel relaxation. This process correlates with a rotation of the magnetic moment in the particle core (see Fig. 1.7). Thus, the Néel time constant is expressed as

$$\tau_\mathrm{N} = \tau_0 \exp\left(\frac{K_\mathrm{eff}V_\mathrm{c}}{k_\mathrm{B}T}\right) \tag{1.16}$$

with the constant τ_0 which is usually quoted to be 1×10^{-9} s [60]. If both relaxation processes are present for one particle type and the two time constants differ only slightly, then the application of the effective time constant τ_eff is appropriate:

$$\tau_\mathrm{eff} = \frac{\tau_\mathrm{B}\tau_\mathrm{N}}{\tau_\mathrm{B} + \tau_\mathrm{N}}. \tag{1.17}$$

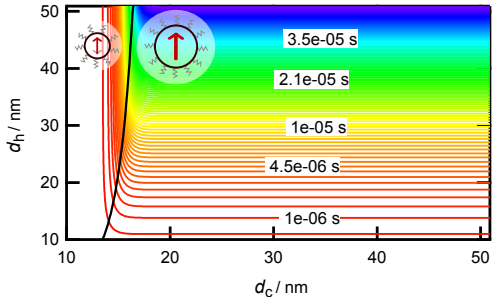

Figure 1.8: Effective time constant in relation to hydrodynamic and core diameter. Black line represents border between particles dominated by the Néel and Brownian relaxation.

If τ_B and τ_N differ significantly from each other, then the relaxation process with the shorter time constant dominates. This is in accordance with Eq. 1.17. Thus, not only the relaxation time but also the process can be influenced by a variation of the particle core and hydrodynamic parameters. In this work, particles dominated by the Brownian and the Néel relaxation process are named Brownian and Néel particles, respectively. Fig. 1.8 illustrates τ_{eff} as a function of the core and hydrodynamic diameter for a viscosity of $1\,\text{mPa}\cdot\text{s}$, an effective anisotropy constant of $20\,\text{kJ/m}^3$ and a temperature of 300 K. The black line corresponds to the border between the Brownian and Néel particle regime, which is specified by the shorter time constant. Due to the exponential dependence of the Néel time constant on the core diameter, the regime of the Néel particles is in this representation comparably small. For instance, a core diameter of 20 nm ensures for all hydrodynamic diameters smaller than 50 nm a domination of the Brownian relaxation process. However, the influence of the viscosity, anisotropy constant and temperature is not considered in Fig. 1.8. Furthermore, the time constants possess a dependence on the strength of the magnetic field which aligns the particles [61, 62].

1.1.4 Size distribution

The synthesis process of a batch of magnetic nanoparticles is not absolutely controllable regarding the uniformity of the different particle parameters. They exhibit size distributions with quite different forms and characteris-

tics. For instance, Gaussian, log-normal and even gamma distributions are applied [63] and the width of the distribution can range from almost mono- to significantly polydisperse.
In this work, the distributions of the particle magnetic moment m as well as the core and hydrodynamic diameter d_c and d_h are described by the log-normal distribution density functions $f_\mathrm{m}(m)$, $f_\mathrm{c}(d_\mathrm{c})$, $f_\mathrm{h}(d_\mathrm{h})$ with the parameters μ_m, μ_c and μ_h as well as σ_m, σ_c and σ_h. The log-normal distribution is well applicable for parameters with a fixed lower border which causes an asymmetric distribution [64]. Thus, it is commonly found for magnetic nanoparticle parameters [48, 65] where natural limits exist, for instance, the particle core size. The log-normal density function of the variable x is defined as

$$f(x) = \frac{1}{\sigma\sqrt{2\pi}} \frac{1}{x} \exp\left[-\frac{(\ln(x)-\mu)^2}{2\sigma^2}\right]. \tag{1.18}$$

The median and mean value of the distribution $\tilde{x}$ and $\bar{x}$ as well as the standard deviation s_x are defined by

$$\tilde{x} = e^{\mu}, \tag{1.19}$$

$$\bar{x} = e^{\mu+\sigma^2/2} \tag{1.20}$$

and

$$s_\mathrm{x} = \bar{x} \cdot \sqrt{e^{\sigma^2}-1}. \tag{1.21}$$

Fig. 1.9 displays log-normal density functions for $\mu = 1$ and different σ. Whereas for $\sigma = 0.05$ the density function is almost identical to the one of a Gaussian distribution, the asymmetric shape is more and more pronounced with increasing σ. This effect is also found for the distribution parameters. For small σ the median value $\tilde{x}$ equals the mean value $\bar{x}$, while for an increasing σ the mean value is growing.

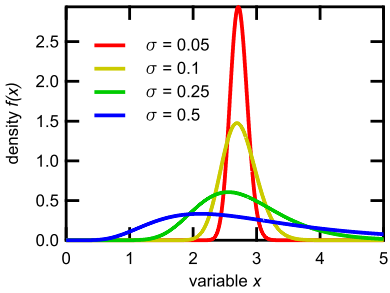

Figure 1.9: Lognormal density functions for median value $\mu = 1$ and different log-normal standard deviations σ.

1.2 Characterization methods

In this work, the rotational dynamics of suspended magnetic nanoparticles are investigated. In this context, the particle hydrodynamic volume and magnetic moment are the main parameters of interest. For the analysis of these parameters a variety of physical measurement techniques exist. This section provides a short overview about the mainly applied techniques.

1.2.1 Electron microscopy

The electron microscopy is based on the quantum mechanical effect, that electrons posses wave-like characteristics, which can be expressed by the de Broglie wavelength. In order to generate electrons with a wavelength that enables the observation of objects in the nano- and even subnanometer range the electrons are accelerated through voltages of up to 400 kV. The scanning electron microscopy (SEM) is based on the measurement of the secondary or backscattered electrons of the primary electron beam, which is irradiating the sample. Thus, the surface of the object is scanned and in the case of nanoparticles the core and shell are imaged. Due to the sample preparation process the MNP shell changes its structure and an accurate determination of the hydrodynamic shell width is hindered. The electron beam of a transmission electron microscope (TEM) is aligned through the sample and detected on the backside. The beam is scattered in dependence on the material density which causes the contrast of a TEM image. For this reason, only the MNP core can be reasonably imaged with a TEM.

A high resolution transmission electron microscope (HRTEM) even enables the analysis of the crystallographic MNP core structure. For the electron microscopy the samples are placed in a vacuum chamber to ensure that no interactions of the electron beam with the air occurs. A detailed description of the operation of electron microscopes was published by Chescoe and Goodhew [66].
For this work, TEM measurements were performed with the Philips CM12 with an acceleration voltage of 100 kV. A drop of suspended MNPs was slowly dried on a carbon coated copper grid to ensure the formation of only one single MNP layer. The MNP suspensions were diluted to an iron concentration of 0.1 g/L. The size distribution of the MNP cores was determined via a software analysis of the TEM images.

1.2.2 Photon correlation spectroscopy

The photon correlation spectroscopy (PCS), which is also known as dynamic light scattering (DLS), facilitates the determination of the hydrodynamic size of suspended nanoparticles via the measurement of light scattered by the particles diffusing in solution [67]. For particles with a diameter d significantly smaller than the wavelength λ of the incident beam the scattered light is dominated by the Rayleigh scattering, while for particles in the size range of λ the more complex Mie scattering has to be taken into account. The intensity I_R of the scattered light (Rayleigh scattering) in the distance F from the causative nanoparticle is expressed by [68]

$$I_\mathrm{R} = \frac{I_0 \pi^4 d^6}{8\lambda^4 F^2} \left(\frac{n_\mathrm{r}^2 - 1}{n_\mathrm{r}^2 + 2} \right)^2 \left(1 + \cos^2 \theta\right). \tag{1.22}$$

Here, I_0 denotes the initial intensity of the incident unpolarized light, θ the measurement angle with respect to the direction of the incident light and n_r the particle refractive index. In addition, I_R depends on d^6 and consequently bigger particles cause a significantly stronger scattering intensity. However, this effect is not analyzed to determine the particle size. The determination is based on the effect that the wavelength of the scattered light exhibits a distribution which correlates with the particle diffusion coefficient D. For spherical noninteracting particles the diffusion coefficient can be expressed

via the Stokes-Einstein expression [67]

$$D = \frac{k_\mathrm{B} T}{3\pi\eta d_\mathrm{h}} \tag{1.23}$$

which incorporates the particle hydrodynamic diameter. In practice, the autocorrelation function of the measured scattering light signal $G_\mathrm{a}(\tau^\star)$ is calculated depending on the delay time $\tau^\star$. This function can be modeled for non-interacting monodisperse particles by

$$G_\mathrm{a}(\tau^\star) = A_\mathrm{a} + B_\mathrm{a} \exp\left(-2Dq^2\tau^\star\right) \tag{1.24}$$

with the scattering vector's amplitude q defined as

$$q = \frac{4\pi n_\mathrm{r}}{\lambda} \sin\left(\frac{\theta}{2}\right). \tag{1.25}$$

The system parameters A_a and B_a define the start and end value of the autocorrelation function. One approach to analyze $G_\mathrm{a}(\tau^\star)$ regarding the hydrodynamic size distribution is the method of cumulants [67, 69]. This method results for mono-modal particles in a reliable determination of the mean particle size and the related polydispersity. However, this approach is not applicable to multi-modal particle distributions. For a known particle distribution type, Eq. 1.24 in combination with the corresponding distribution function can be fitted with a nonlinear least-squares approach to the measurement results [70]. Alternatively, the Contin and the non-negative least-squares (NNLS) methods are utilized [67], which require additional prior knowledge. The size distribution directly determined from the measurement results is intensity weighted due to the scattered light based measurement principle of PCS. This necessitates a conversion of the directly determined distribution function to a volume or number weighted one if a comparison with other measurement techniques or the usage in other physical models is intended [70]. Furthermore, PCS measurement results can be easily affected by various physical or chemical effects. For instance, multiple scattering between the diluted particles can significantly influence the decay of $G_\mathrm{a}(\tau^\star)$, resulting in a wrong determined particle size. Other manipulating aspects that have to be avoided are number fluctuations of the

particles in the measurement window, interactions between the particles in the solution or a change of the sample temperature and viscosity. Moreover, the size distribution of small particles determined via PCS is sensitive to some few larger particles in solution [71]. Due to the intensity weighted measurement signal, larger particles can dominate the signal and cause the size distribution to exhibit a shift or tail to larger sizes which does not reflect the reality. Thus, the size determination of magnetic nanoparticles with PCS is also influenced by non-magnetic contamination.
For the investigations of this work, the photon cross-correlation spectrometer (PCCS) system Nanophox from Sympatec GmbH was utilized. In this measurement system, two laser-detector pairs are installed which enable the calculation of the cross-correlation spectrum. The analysis of this spectrum for the investigation of the particle size significantly reduces the negative influence of multiple-scattering [72], because single- and multiple-scattering events can be distinguished. As sample cuvette the UVette from Eppendorf AG was applied for all measurements. The sample volume was 100 µL and the particle iron concentration ranged from 1 mg/L to 50 mg/L.

1.2.3 Static magnetization curve

The measurement of the static magnetization curve is an essential tool for the determination of the particle magnetic moments. Furthermore, it can be exploited to investigate the particle core size [73] and to specify the blocking temperature [48] or the material phase composition [74] by performing temperature-dependent measurements. In principle, an ensemble of MNPs is placed in the system, aligned along a stepwise increasing static magnetic field and the resulting magnetization is measured with a magnetic field sensor. In order to reach the saturation of the MNP ensemble's magnetization, magnetic fields of up to 5 T are required. Thus, superconducting coils are built into a corresponding measurement system. As magnetic field sensors superconducting quantum interference devices (SQUIDs) are commonly used to ensure the measurement of even weak paramagnetic material. So, for both processes, the field generation and the magnetization detection, a cryogenic cooling is required, which is usually realized with liquid helium. The analysis of the measurement data can be performed by fitting the Langevin equation (Eq. 1.7) incorporating an appropriate distribution function to the measured static magnetization curve. However, this method requires the knowledge of the distribution type. A physically more adequate way to estimate the distribution can be achieved by the reconstruction of the

magnetization curve via the Langevin function applying singular value decomposition (SVD). The SVD method was already successfully employed for this purpose by Berkov et al. [65]. The static magnetization measurements in this work were performed with the Magnetic Property Measurement System (MPMS) from Quantum Design International on liquid samples with a particle iron concentration in the range of 0.1 g/L to 0.5 g/L.

1.2.4 AC susceptibility

An ensemble of MNPs in a time-varying magnetic field possesses a frequency-dependent susceptibility χ. Fannin et al. [75] studied this effect on ferrofluids and presented a description of the so called AC susceptibility (ACS) based on Debye's theory for dielectric effects in dipolar fluids [76]. In the case of MNPs dominated by the Brownian relaxation process the measurement of the complex AC susceptibility χ facilitates the determination of the particles hydrodynamic size. The susceptibility's real and imaginary part χ' and χ'' are described by

$$\chi'(\omega) = \frac{\chi_0}{1 + (\omega\tau_\mathrm{B})^2} \tag{1.26}$$

and

$$\chi''(\omega) = \frac{\chi_0\,\omega\tau_\mathrm{B}}{1 + (\omega\tau_\mathrm{B})^2} \tag{1.27}$$

as a function of the angular frequency $\omega = 2\pi f$, the Brownian time constant as well as the initial DC susceptibility (see subsection 1.1.3). The real part possesses a drop with increasing frequency, whereas the imaginary part exhibits a global maximum at a distinct frequency (Fig. 1.10). The position of the imaginary part maximum coincides in the ideal case with the one of the real part dropped to half of its start value. At this point the product of the time constant and the angular frequency $\omega\tau_\mathrm{B}$ is one. Therefore, the MNP dynamics are also specified by the characteristic frequency f_c, which is defined as

$$f_\mathrm{c} = \frac{1}{2\pi\tau_\mathrm{B}} \tag{1.28}$$

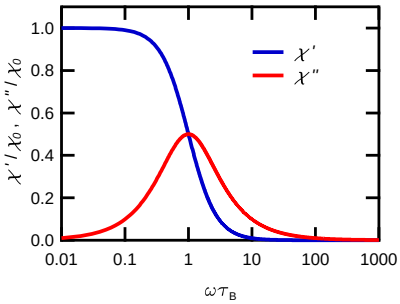

Figure 1.10: Real and imaginary part χ' and χ'' of complex AC susceptibility as a function of angular frequency and Brownian time constant.

and gives an estimation of the maximum frequency of a dynamic alternating magnetic field that a MNP can follow. Eq. 1.26 and 1.27 are well applicable for a Langevin parameter $\xi \ll 1$ which ensures a linear dependence of the ensemble magnetization on the magnetic field. However, for larger ξ, for instance, caused by an increased field strength, the model needs to be extended. One approved extension was introduced by Yoshida et al. [62] and subsequently improved by solving the Fokker-Planck equation [77]:

$$\chi'(\omega) = \frac{\chi_1(0)}{1 + (\omega\tau_{\mathrm{B,H}})^2} \tag{1.29}$$

and

$$\chi''(\omega) = k'' \frac{\chi_1(0)\,\omega\tau_{\mathrm{B,H}}}{1 + (\omega\tau_{\mathrm{B,H}})^2} \tag{1.30}$$

with

$$\chi_1(0) = \chi_0 \left[1 - \frac{0.0636\xi^2}{1 + 0.18\xi + 0.0659\xi^2}\right], \tag{1.31}$$

$$k'' = 1 + \frac{0.024\xi^2}{1 + 0.18\xi + 0.033\xi^2} \tag{1.32}$$

and

$$\tau_{\mathrm{B,H}} = \frac{\tau_B}{\sqrt{1 + 0.126\xi^{1.72}}}. \tag{1.33}$$

With this set of equations incorporating the field-dependent Brownian time constant $\tau_{\mathrm{B,H}}$ an approximate description of the MNPs' dynamic magnetization in an alternating magnetic field even for $\xi > 1$ is possible. The consideration of the particle size distribution enables a correct modeling of real MNP samples. For instance, Chung et al. [8] introduced for the theoretical description of spherical MNPs' complex ACS independent core and hydrodynamic size distributions. The adoption of this approach to Eq. 1.29 and 1.30 results in

$$\chi'(\omega) = \int_{d_\mathrm{h}} f_\mathrm{h}(d_\mathrm{h}) \int_{d_\mathrm{c}} f_\mathrm{c}(d_\mathrm{c}) \frac{\mu_0 n m^2(d_\mathrm{c})}{3k_\mathrm{B}T} \frac{\chi_{1,\mathrm{n}}(0)}{1 + (\omega\tau_{\mathrm{B,H}})^2} dd_\mathrm{c} dd_\mathrm{h} \tag{1.34}$$

and

$$\chi''(\omega) = \int_{d_\mathrm{h}} f_\mathrm{h}(d_\mathrm{h}) \int_{d_\mathrm{c}} f_\mathrm{c}(d_\mathrm{c}) \frac{\mu_0 n m^2(d_\mathrm{c})}{3k_\mathrm{B}T} k'' \frac{\chi_{1,\mathrm{n}}(0)\omega\tau_{\mathrm{B,H}}}{1 + (\omega\tau_{\mathrm{B,H}})^2} dd_\mathrm{c} dd_\mathrm{h} \tag{1.35}$$

with $\chi_1(0)$ normalized to χ_0:

$$\chi_{1,n}(0) = 1 - \frac{0.0636\xi^2}{1 + 0.18\xi + 0.0659\xi^2}. \tag{1.36}$$

The presence of MNPs dominated by the Néel relaxation also affects the measured AC susceptibility. In the case of a pure Néel particle sample similar real and imaginary parts occur and for a theoretical description with the Debye model τ_B is replaced by τ_N. For a sample with both particle types present in solution two cases exist: If the time constants fulfill the condition $\tau_\mathrm{N} \ll \tau_\mathrm{B}$ the complex AC susceptibilities of the Brownian and Néel particles can be treated independently as theoretically shown by Fannin and Charles [75] and supported with measurements by Lak et al. [78]. Consequently, these samples are characterized as bi-modal. For $\tau_\mathrm{N} \approx \tau_\mathrm{B}$ the single real and imaginary parts overlap each other with the result that no clear dis-

tinction is possible. A theoretical description with the Debye model can be performed if τ_B is replaced by τ_{eff} [8]. A clear distinction between the ACS of the Brownian and the Néel particles can be achieved by performing additional measurements on the same sample after it is freeze-dried. Thus, all suspended particles are immobilized and Brownian rotation is blocked. In this work, a self-constructed ACS measurement setup was applied. It is based on a cylindrical inductor for the generation of the homogeneous alternating excitation field with an magnitude of 95 µT and an integrated detection coil. For the realization of a gradiometric detection principle both coils are set up twice with parameters as similar as possible. The frequency range of the measurement setup is 0.2 kHz to 1000 kHz. A detailed description of the applied setup was given by Ludwig et al. [40]. The samples for the ACS measurements are placed into a cylindrical glass vial with an outer diameter of 7.8 mm or a conical plastic vial usually used for microtiter plates. The sample volume was 150 µL and the particle iron concentration ranged from 0.1 g/L to 5 g/L.

1.2.5 Magnetorelaxometry

The measurement of the magnetization relaxation process $M_{rel}(t)$ of an ensemble of MNPs is the basis of the magnetorelaxometry (MRX). For this reason, the MNPs are aligned in a static magnetic field H, which causes after a distinct time t_{mag} the MNP magnetization M (see Fig. 1.11). In the ideal case the magnetizing field is switched off instantaneously and the induced relaxation process is measured and analyzed to characterize the applied MNPs. The magnetization of Néel particles in a so called switched magnetic field can be described by the moment superposition model (MSM) [79, 80]. For monodisperse non-interacting Néel particles the MSM is simplified and $M_{rel}(t)$ can be expressed by

$$M_{rel}(t) = M_\infty \left[1 - \exp\left(-t_{mag}/\tau_{N,H}\right)\right] \exp\left(-t/\tau_N\right) \tag{1.37}$$

with the MNP magnetization M_∞ after $t_{mag} = \infty$ for the given field strength. The first part of this equation with the field-dependent Néel time constant $\tau_{N,H}$ describes the magnetization process, whereas the second part the magnetization relaxation process. Different expressions of $\tau_{N,H}$ based on one approach were discussed in detail by Chantrell [79], Eberbeck [80] and Ludwig [55]. The general form of the MSM, which incorporates the core size

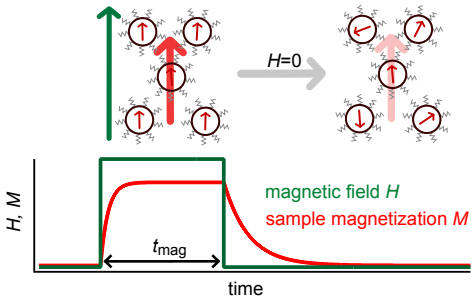

Figure 1.11: Magnetorelaxometry (MRX) principle based on the alignment of an MNP ensemble in a switched DC field and the measurement as well as analysis of the resulting magnetization relaxation process.

density function $f(d_c)$, is described by

$$M_{rel}(t) = nM_s \int_{d_c} f(d_c) \frac{\pi}{6} d_c^3 L(d_c) \left[1 - \exp\left(-\frac{t_{mag}}{\tau_{N,H}}\right)\right] \times \exp\left(-\frac{t}{\tau_N}\right) dd_c. \tag{1.38}$$

This model was extended by Eberbeck et al. [81] for the description of MNPs suspended in a carrier liquid, which are additionally affected by the Brownian relaxation process. The resulting cluster moment superposition model (CMSM) incorporates τ_{eff} (see section 1.1.3) and the corresponding field-dependent effective time constant $\tau_{eff,H}$:

$$M_{rel}(t) = nM_s \int_{d_h} f(d_h) \int_{d_c} f(d_c) \frac{\pi}{6} d_c^3 L(d_c) \left[1 - \exp\left(-\frac{t_{mag}}{\tau_{eff,H}}\right)\right] \times \exp\left(-\frac{t}{\tau_{eff}}\right) dd_c dd_h. \tag{1.39}$$

Here, the particle hydrodynamic size distribution is represented by the density function $f(d_h)$. Consequently, this model can be fitted to the measured magnetization relaxation curves to determine the particle parameters and binding state with respect to a possible functionalization [82]. A reduction of the number of free fitting parameters can be achieved by the determination

of the core size distribution parameters from an independent measurement on a freeze-dried reference sample with Eq. 1.38.
The magnetic field strength in a MRX setup usually accounts to some millitesla, because no magnetization saturation is required. Thus, air coils powered by an fast switching electronics are utilized. For the detection of the MNPs' magnetization decay SQUIDs, fluxgates and magnetoresistive sensors are applied. The MRX measurements in this work were performed with a fluxgate-based setup [83]. The field strength was set to 2 mT and t_{mag} as well as the measurement time to some seconds, depending on the particle properties.

1.3 Bioassays

The application of receptors for the identification and quantification of biological targets in a sample is described as bioassay. The receptor displays a bio-recognition molecule, for instance an antibody, that specifically binds to the biological target molecule of interest, for instance a biomarker indicating a medical condition. If antibodies are utilized as receptors the term immunoassay is commonly used. The recognition or formation of a receptor-target complex is the first step in a bioassay. The second one is the detection and analysis of the complexes in the solution. Therefore, additional processing steps and instrumentation are required, which enable the transduction of the recognition process into an analyzable electrical signal. Thus, the second step is also characterized as transducer and based on an electrochemical, optical, mass sensitive, thermometric, radioactive, magnetic or other physical effect [84, 85].
In the context of bioassays the term biosensor is frequently applied. In principle both display the same application: The identification and quantification of biological material. However, a difference exists which is expressed by the definition of electrochemical biosensors given by the International Union of Pure and Applied Chemistry [86]: "An electrochemical biosensor is a self-contained integrated device, which is capable of providing specific quantitative or semi-quantitative analytical information using a biological recognition element (biochemical receptor) which is retained in direct spatial contact with an electrochemical transduction element." Due to this spatial proximity any other processing step is not required. The receptors in a biosensor directly induce the electrical transducer signal. Fig. 1.12 illustrates this difference compared to the general concept of a bioassay that

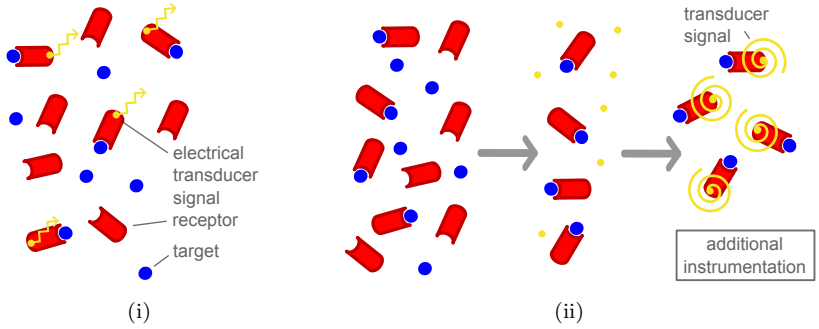

Figure 1.12: Comparison of biosensor and bioassay concept: (i) Receptor-target complexes induce directly the electrical biosensor output signal. (ii) Different processing steps and instrumentation are required to receive analyzable electrical signals in a bioassay.

incorporates different steps and instrumentation. Furthermore, a biosensor which is disposable or at least unable to monitor continuously the concentration of the biological material is also defined as bioprobe. The most popular examples for a biosensor are glucose and pregnancy testing [87]. At this point it should be mentioned, that the given definitions are not adopted one-to-one by all users [85]. However, this work will employ them and, therefore, introduce the following two groups: Homo- and heterogeneous bioassays. If the recognition and transduction process are realized in one step, but still further instrumentation is required for the generation of an analyzable electrical signal, than it is characterized as a homogeneous bioassay. This assay type is the intended application of the work's research and enables a faster process and a real-time analysis of the sample solution compared to the classical heterogeneous bioassays, for example the enzyme-linked immunosorbent assay. In the following sections a short overview about different assay types is given. In addition, the law of mass action is presented, which describes the dependence of the receptor-target complex concentration on the initial ones. Finally, the logistic function is introduced. It facilitates a calibration of the assay.

1.3.1 Enzyme-linked immunosorbent assay

The enzyme-linked immunosorbent assay (ELISA) is one of the standard methods for the quantification of biological material in samples as proteins, peptides, hormones and other small molecules [84]. As recognition molecules antibodies are used. The transduction process is based on enzymes which amplify the reaction of a substrate into products. The products themselves cause optically detectable effects, for example a colorimetric one. The standard enzyme for the catalytic reaction is horseradish peroxidase (HRP). The instrumentation for the detection of the optical effect is commonly a photometer which enables the determination of the product concentration via the Beer–Lambert law [84]:

$$A_{\text{opt}} = -\ln(\frac{I}{I_0}) = \varepsilon bc. \tag{1.40}$$

The absorbance A_{opt}, which is measured by the photometer, is proportional to the natural logarithm of the relative intensity attenuation $\frac{I}{I_0}$. If this attenuation depends only on the molecular absorption of the sample's products, then A_{opt} is directly proportional to the molecular extinction coefficient ε, the light path length in the sample b and the product concentration c. Finally, the target molecule concentration depends directly on the optically measured amount of products in solution. A calibration of the whole assay ensures a correct relation of the different quantities.
There exist several configurations of ELISA. In the direct format (see Fig 1.13(i)) the target molecule (antigen) is linked to a plate by covalent bonds or adsorption. Then the enzyme-linked antibody is added to the plate. After the equilibrium of the antibody-antigen reaction is reached, not reacted antibody is washed out through several washing steps. Finally, the substrate is added and converted into its products, if linked enzymes are present in the solution. The direct ELISA display the fastest format, however, it requires extra effort for the linking of the enzymes to each target-specific antibody type. This problem can be solved by the application of an enzyme-linked secondary antibody (see Fig 1.13(ii)) which binds the enzyme-free primary target-specific antibody (indirect ELISA). A higher specificity and consequently signal-to-noise ratio is achieved by the sandwich assay. Here, the antigen in the investigated solution is captured by another primary antibody which is initially bound to the plate. Further ELISA formats exist with different advantages and drawbacks.

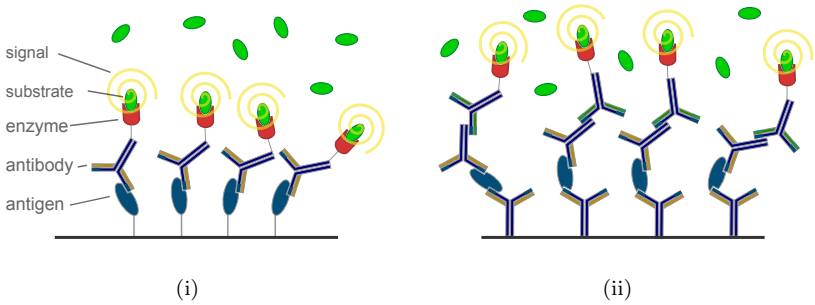

Figure 1.13: ELISA in a direct configuration (i) and as a sandwich type (ii) with two primary and one secondary antibody for each antigen.

In general, ELISA displays an excellent method for the quantification of biological material and it has been dominating the laboratory immunoassays for more than 20 years. However, it is limited to the operation in climate-controlled laboratories with skilled personnel due to the in parts complex and time-consuming preparation steps [4], which are characteristic for a heterogeneous bioassay.

1.3.2 Magnetic assays

The application of antibody functionalized Brownian MNPs enables the realization of homogeneous bioassays. The basic principle consists of one preparation step, the mixture of the sample and the MNPs, as well as a measurement step after the binding reaction reached its equilibrium. For the second step, the MNPs are manipulated with a magnetic field and their dynamic response is analyzed in order to determine the amount of bound target molecules, because a change of the particle hydrodynamic size affects directly the Brownian particle dynamics in solution. The whole procedure is also named as a mix-and-measure principle. The hydrodynamic size of the MNPs is typically below 100 nm to ensure a measurable hydrodynamic size change also for small bound target molecules. If the detection is based on the agglutination of the MNPs via the target molecules also larger particles are applied. The investigated particles have either a single- or a multi-core. The detection of the particle dynamics can be performed magnetically or optically. However, some optical detection schemes, e.g. the direct measurement of light scattered or transmitted by the particles, require MNPs

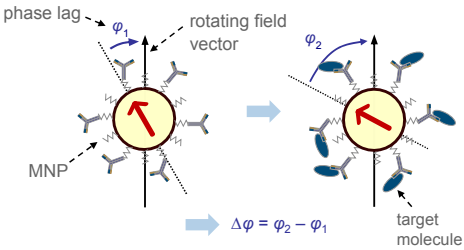

Figure 1.14: Principle of the homogeneous bioassay based on MNPs in a rotating magnetic field. The phase lag between the particle magnetic moment and the field is increased by bound target molecules.

with a shape anisotropy. For the manipulation of the MNPs different magnetic field types were investigated. One of the first approaches, the so called magnetic relaxation immunoassay (MARIA) [5, 28], adopts the MRX technique with the switched magnetic DC fields (see section 1.2.5). Besides the quantification of small target molecules, the MRX technique was employed for the tumor cell detection and imaging [88, 89]. Connolly et al. [7] proposed an approach which is based on the measurement of the ACS in alternating magnetic fields (see section 1.2.4). This manipulation technique was transfered by several researchers into practical applications and continuously improved [9, 8, 90, 91, 92]. For instance, the generation of two alternating fields with different frequencies and the measurement of the mixed frequency ACS facilitates the detection of a highly MNP specific signal [93, 94]. A comparable new approach is based on a rotating magnetic field (RMF), which is subject of this work. The initial idea was presented and realized by Schrittwieser et al. [3, 95] with elongated MNPs and an optical detection scheme. However, it is also applicable for other particle shapes and a magnetic detection scheme as presented in this work. The assay principle is depicted in Fig. 1.14. The phase lag φ between the particle magnetic moment and the RMF is measured before and after the target molecules are bound. Due to the dependence of φ on the particle hydrodynamic size, the phase lag change $\Delta\varphi$ is analyzed for the quantification of the bound targets. The further chapters of this work will deal with theories describing the magnetization dynamics of MNPs in a RMF, the construction of a measurement setup for the analysis of the dynamics, measurements on real samples and a realization of the bioassay principle.

A wide variety of other magnetic particle based bioassays has been presented in the literature. Some of them even facilitate rotating magnetic fields but with particles in the upper nanometer or micrometer range. Thus, bacteria cells instead of small proteins were detected [11] or a cluster formation process was required [12]. Heterogeneous bioassays in combination with magnetic particles have also been intensively studied, e.g. the so called micro- or biochip based assays [96]. Another promising biosensor format which can be combined with MNPs are the lateral flow techniques which require almost no sample preparation [97].

1.3.3 Law of mass action

The recognition process of the receptor R with respect to the target T in a bioassay displays a reversible binding reaction between the two reactants R and T that form the product RT:

$$\mathrm{R} + \mathrm{T} \rightleftharpoons \mathrm{RT}. \tag{1.41}$$

This reaction can be modeled at its equilibrium via the law of mass action [98]:

$$K_\mathrm{a} = \frac{c\,(\mathrm{RT})}{c\,(\mathrm{R})\;c\,(\mathrm{T})}. \tag{1.42}$$

Here, K_a represents the association constant which describes the strength of the affinity in a binding reaction. The reactant concentrations $c\,(\mathrm{R})$ and $c\,(\mathrm{T})$ are related to the initially applied concentrations c_0 as follows:

$$c\,(\mathrm{R}) = c_0\,(\mathrm{R}) - c\,(\mathrm{RT}) \tag{1.43}$$

and

$$c\,(\mathrm{T}) = c_0\,(\mathrm{T}) - c\,(\mathrm{RT})\,. \tag{1.44}$$

Finally, the concentration of the product $c\,(\mathrm{RT})$ as a function of the initial reactant concentrations and the association constant can be expressed by [84]

$$c\,(\mathrm{RT}) = 0.5\,(c_0\,(\mathrm{T}) + c_0\,(\mathrm{R}) + 1/K_\mathrm{a}) - 0.5\left[(c_0\,(\mathrm{T}) + c_0\,(\mathrm{R}) + 1/K_\mathrm{a})^2 - 4\,c_0\,(\mathrm{T})\,c_0\,(\mathrm{R})\right]^{1/2}. \quad (1.45)$$

Here, it can be seen that the concentration of the product does not scale linearly with the initial concentrations of the reactants. In fact, below the concentration range of the inverse association constant, the concentration relation of the product to the initial reactants starts to shrink significantly. Thus, a high affinity constant and a high receptor concentration are desirable for the creation of enough receptor-target complexes (products) and a strong transducer signal. In addition, Eq. 1.45 can be utilized to determine the binding reaction's association constant. Therefore, a sample series with different known target molecule concentrations and a fixed amount of receptors is analyzed regarding the resulting product concentrations and Eq. 1.45 is fitted to these results with K_a as a free parameter.

1.3.4 Assay calibration with logistic function

A logistic function (see Fig. 1.15) is commonly used to analyze the results of bioassays to provide a relation between the physical transduction effect and the target molecule concentration [99] and corresponds to the Hill equation [100] which is directly derived from a binding reaction scheme between molecules and receptors. In contrast to the law of mass action it incorporates the possibility of multiple receptor binding sites. The logistic function was also used to model the measurement effect versus target molecule concentration in the susceptibility reduction method by Yang et al. [91]. For the physical effect S of a bioassay as a function of the initial target molecule concentration c_0, the logistic function takes the form

$$S = \frac{S_\mathrm{low} - S_\mathrm{high}}{1 + \left(\frac{c_0}{c_{0,\mathrm{half}}}\right)^\alpha} + S_\mathrm{high} \quad (1.46)$$

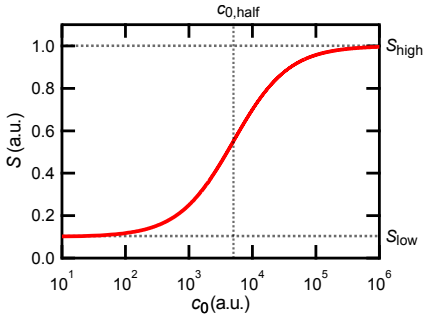

Figure 1.15: Logistic function in a half logarithmic representation illustrating the dependence of the physical effect S on the initial target molecule concentration c_0.

with the minimal and maximal possible physical effect S_{low} and S_{high} as well as the target molecule concentration which causes the physical effect $(S_{\mathrm{high}} - S_{\mathrm{low}})/2$. The parameter α affects the slope of the curvature [99] and can correlate in the case of a binding reaction scheme with the number of target molecules bound to one receptor [100]. A calibration of the bioassay is performed as follows. A series of samples with a fixed receptor concentration and a varying amount of target molecules is prepared. Here, a wide concentration range has to be investigated, which covers a not measurable change of S and its saturation. The transducer effect is analyzed for each sample and plotted against c_0. Finally, the logistic function is fitted to the measurement result. The gained parameters enable the definite translation of any measured physical effect into the target molecule concentration.

2 Rotating magnetic field

In this chapter, theories describing the rotational dynamics of a MNP ensemble magnetization in a rotating magnetic field are presented. The models are based on the assumption that the MNPs are single-core particles dominated by the Brownian relaxation process also referred to as rigid magnetic dipole [101]. A mechanical model based on the equilibrium of forces [102] can be applied to describe the principle dependencies of the magnetization on the parameters. However, a realistic model including thermal agitation is based on magnetization equations as clarified by Shliomis [103]. These can either be phenomenological magnetization equations [101, 104] or a model derived microscopically from the Fokker-Planck equation via the effective-field method [105, 106]. Finally, Yoshida et al. [107] published numerical solutions of the Fokker-Planck equation adapted to MNP in RMF and derived an empirical model with a high accuracy for the analysis of RMF measurements. The corresponding set of equations is applied for the analysis of the measurement results in the present work. The modeling of the complete MNP ensemble magnetization in a rotating magnetic field represents a vectorial problem. Thus, the according vector quantities are identified by an arrow.

2.1 Definition of a rotating magnetic field

The RMF is defined as a magnetic field which rotates with a constant field magnitude H and angular frequency ω in the (x,y)-plane:

$$\vec{H} = [H\cos(\omega t), H\sin(\omega t), 0]. \tag{2.1}$$

The dynamic MNP ensemble magnetization $\vec{M}$ rotates in the steady-state with the same angular frequency as explained by Zaitsev and Shliomis [108]. However, $\vec{M}$ lags behind $\vec{H}$ with a characteristic phase lag φ, which is expressed by the difference of the RMF and magnetization phase angles φ_{H}

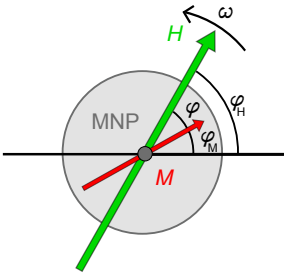

Figure 2.1: Magnetic nanoparticle with magnetization $\vec{M}$ (rigid magnetic dipole) in rotating magnetic field $\vec{H}$ with phase lag φ and angular frequency ω.

and φ_{M} (see Fig. 2.1). Thus, $\vec{M}$ is expressed as

$$\vec{M} = [M\cos(\omega t - \varphi), M\sin(\omega t - \varphi), 0]. \tag{2.2}$$

In the following sections theories are introduced which can be adopted to describe the dependence of φ on the field strength and frequency as well as the particle and suspension characteristics.

2.2 Mechanical model

A mechanical model for the description of the rotational motion of magnetic nanoparicles in rotating magnetic fields was introduced by Keshoju et al. [102, 109] for elongated particles, so called nanorods. Additionally, a similar approach was applied by Günther et al. [44] to determine the rotational diffusion coefficient of nickel nanorods in suspension. Here, the mechanical model is adopted for spherical magnetic nanoparticles.
In a RMF a magnetic torque $\vec{\tau}_{\mathrm{m}}$ acts on a MNP which is defined as

$$\vec{\tau}_{\mathrm{m}} = \vec{m} \times \mu_0 \vec{H}. \tag{2.3}$$

Thus, the absolute value τ_{m} can be calculated with

$$\tau_{\mathrm{m}} = \mu_0 M_{\mathrm{s}} \frac{\pi}{6} d_{\mathrm{c}}^3 H_0 \sin(\varphi). \tag{2.4}$$

Due to the rotational drag that a rotating spherical MNP possesses, an opposite viscous torque $\vec{\tau}_\mathrm{d}$ exists [110] whose absolute value is given by

$$\tau_\mathrm{d} = \pi\omega\eta d_\mathrm{h}^3. \tag{2.5}$$

In the steady state τ_m and τ_d are equal. Thereby, the phase lag φ is related to the rotating field, particle and suspension characteristics via the following expression:

$$\varphi = \arcsin\left[\frac{6\eta\omega d_\mathrm{h}^3}{\mu_0 M_\mathrm{s} d_\mathrm{c}^3 H_0}\right]. \tag{2.6}$$

This equation gives an impression of the dependence of the phase lag on the mentioned parameters. However, the inverse sinus dependence is not reflected by measurements of the nanoparticles' magnetization in a RMF. As mentioned by Rosensweig [50], Eq. 2.6 is only valid for larger nanoparticles which are not disturbed by a reorientation process induced by the Brownian motion. In fact, for magnetic nanoparticles applied in this work an inverse tangent relation is observed which can be described by the following theories.

2.3 Magnetization equations

The application of a phenomenological magnetization equation developed for the description of the dynamics of ferrofluids - suspended MNPs - in magnetic fields enables a physical correct method to model the MNP ensemble magnetization in a RMF. Shliomis presented in 1972 a phenomenological magnetization equation [101] as a modification of the Debye relaxation model [76] and consequently generalized it [103]. The model is based on different ideas: The allowance of internal rotation explains the existence of a visible and a non-visible internal angular momentum of the ferrofluid. The former can be expressed by the local angular velocity of the whole fluid $\vec{\Omega}$ and the latter by the angular velocity of the single particles $\vec{\omega}_\mathrm{p}$. A deviation of these angular velocities can be maintained by the torque of a magnetic field acting on the MNP ensemble magnetization which is expressed by

$$6\eta\phi(\vec{\omega}_\mathrm{p} - \vec{\Omega}) = \vec{M} \times \vec{H}. \tag{2.7}$$

Here, ϕ represents the volume fraction of solid phase in solution and η the dynamic viscosity. A local frame of reference $\Sigma^\star$ is introduced to keep the single particles quiescent. Thus, the frame rotates with the angular velocity $\vec{\omega}_\mathrm{p}$ and any change of the magnetization vector in the rotating frame of reference $\mathrm{d}^\star\vec{M}/\mathrm{d}t$ is attributed to the fixed observer frame of reference Σ by

$$\frac{\mathrm{d}\vec{M}}{\mathrm{d}t} = \vec{\omega}_\mathrm{p} \times \vec{M} + \frac{\mathrm{d}^\star\vec{M}}{\mathrm{d}t}. \tag{2.8}$$

In addition, the magnetization relaxation in the system follows the Debye-like equation

$$\frac{\mathrm{d}^\star\vec{M}}{\mathrm{d}t} = -\frac{1}{\tau_\mathrm{B}}(\vec{M} - \vec{M}_0) \tag{2.9}$$

with the Brownian time constant τ_B for the rigid dipoles and the equilibrium magnetization $\vec{M}_0$. After the substitution of Eq. 2.7 and 2.9 into 2.8, one can split small magnetization deviations from its equilibrium $\vec{M} - \vec{M}_0$ into the components parallel and perpendicular to the magnetic field. Finally, the general form of the magnetization equation is expressed by [103]

$$\frac{d\vec{M}}{dt} = \vec{\Omega} \times \vec{M} - \frac{\vec{H}\left[\vec{H} \cdot (\vec{M} - \vec{M}_0)\right]}{H^2\tau_\parallel} - \frac{\vec{H} \times (\vec{M} \times \vec{H})}{H^2\tau_\perp}. \tag{2.10}$$

$\vec{M}_0$ is described by the Langevin equation $L(\xi)$ as $\vec{M}_0 = nmL(\xi)\vec{\xi}/\xi$, where n represents the particle number density. For the splitting of the magnetization deviation into the components parallel and perpendicular to the field $\vec{H}$, the two time constants $\tau_\parallel$ and $\tau_\perp$ are introduced as

$$\tau_\parallel = \tau_\mathrm{B} \tag{2.11}$$

and

$$\tau_{\perp} = \frac{2\tau_{\mathrm{B}}}{2 + \xi L(\xi)}. \tag{2.12}$$

A further magnetization equation for the description of the magnetization process of suspended MNPs is based on a microscopical derivation from the Fokker-Planck equation via the effective-field method [105, 106]. This approach was successfully used to describe measurements on ferrofluids [111, 112, 113]. Moreover, it coincides with numerical solutions of the Fokker-Planck equation [114] and was applied as a reference for comparisons with other magnetization equations [103, 115]. It is given by:

$$\frac{d\vec{M}}{dt} = \vec{\Omega} \times \vec{M} - \left[1 - \frac{(\vec{\xi} \cdot \vec{\zeta})}{\zeta^2}\right] \frac{\vec{M}}{\tau_{\mathrm{B}}} - \frac{1}{L(\zeta)} \left[\frac{1}{L(\zeta)} - \frac{1}{\zeta}\right] \frac{\vec{M} \times (\vec{M} \times \vec{H})}{6\eta\phi}. \tag{2.13}$$

Here, $\vec{M}$ is related to the effective field $\vec{H}_{\mathrm{e}}$ via $\vec{M} = nmL(\zeta)\vec{\zeta}/\zeta$ with the dimensionless effective field $\vec{\zeta} = m\mu_0\vec{H}_{\mathrm{e}}/k_{\mathrm{B}}T$ and the true dimensionless field $\vec{\xi} = m\mu_0\vec{H}/k_{\mathrm{B}}T$ based on the definition of the Langevin parameter. This magnetization equation is certainly more complex for analyzing MNP magnetization dynamics. Hence, Eq. 2.13 can be linearized if the effective field $\vec{H}_{\mathrm{e}}$ departs only slightly from the equilibrium and it reduces to Eq. 2.10 incorporating the parallel and perpendicular time constants [103]

$$\tau_{\parallel} = \frac{d \ln L(\xi)}{d \ln \xi} \tau_{\mathrm{B}} \tag{2.14}$$

and

$$\tau_{\perp} = \frac{2L(\xi)}{\xi - L(\xi)} \tau_{\mathrm{B}}. \tag{2.15}$$

This set of times constants results compared to the previous ones (Eq. 2.12 and 2.11) in a slightly preciser description of the MNP magnetization dynamics which is demonstrated by a comparison of the phase and magnitude errors of MNPs in a RMF in section 2.5.

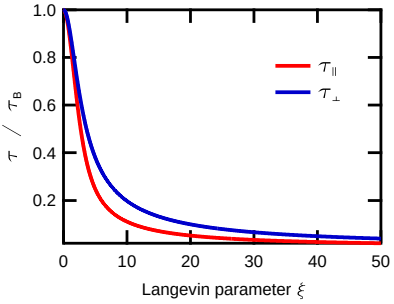

Figure 2.2: Relaxation time constants $\tau_{\parallel}$ (Eq. 2.14) and $\tau_{\perp}$ (Eq. 2.15) normalized to τ_{B}.

Whereas Eq. 2.10 and 2.13 provide a general description of the MNP magnetization dynamics in various magnetic fields, they considerably simplify for a MNP ensemble in a RMF as expressed by Eq. 2.1 and 2.2. In this case, one can introduce a frame of reference for the magnetization equation rotating with the angular frequency ω [103]. Thus, $\vec{H}$, $\vec{M}$ and $\vec{M}_0$ become constant vectors

$$\vec{H} = [H, 0, 0], \tag{2.16}$$

$$\vec{M} = [M\cos(\varphi), -M\sin(\varphi), 0], \tag{2.17}$$

$$\vec{M}_0 = [M_0, 0, 0] \tag{2.18}$$

and the angular velocity of the whole MNP suspension $\vec{\Omega}$ is reduced by the RMF angular velocity $\vec{\omega}$. Under the condition that a MNP suspension in a homogeneous RMF is quiescent with $\vec{\Omega} = \vec{0}$ [108] Eq. 2.10 results in:

$$\begin{aligned}\vec{0} = &[-M\sin(\varphi)\omega, -M\cos(\varphi)\omega, 0] - \frac{1}{\tau_{\parallel}}\left[M\cos(\varphi) - M_0, 0, 0\right] \\ &- \frac{1}{\tau_{\perp}}\left[0, -M\sin(\varphi), 0\right].\end{aligned} \tag{2.19}$$

Consequently φ can be defined via the y-component of Eq. 2.19 as

$$\varphi = \arctan(\omega\tau_\perp). \tag{2.20}$$

The magnitude of the magnetization M results from the x-component of Eq. 2.19 with $\tau_\perp \approx \tau_\parallel$ for $\xi < 1$ (see Fig. 2.2) and Eq. 2.20 in

$$M = M_0 \cos(\varphi). \tag{2.21}$$

Due to these simplifications the real and imaginary part of the MNP magnetization M' and M'' in a RMF can be described with a Debye-like model:

$$\frac{M'}{M_\mathrm{s}} = \frac{L(\xi)}{1 + (\omega\tau_\perp)^2} \tag{2.22}$$

and

$$\frac{M''}{M_\mathrm{s}} = \frac{L(\xi)\omega\tau_\perp}{1 + (\omega\tau_\perp)^2}. \tag{2.23}$$

These equations reduce for $\xi \ll 1$ to the Debye model which is utilized for the theoretical description of the complex AC susceptibility in low fields. Thus, the dynamic MNP magnetization in a RMF and alternating magnetic field are identical for $\xi \ll 1$. Finally, it can be seen that the phase lag of the MNP magnetization in a RMF reveals an inverse tangent dependence on the perpendicular time constant and RMF angular frequency. The direct proportionality of $\tau_\perp$ to τ_B leads to an increase of φ with growing hydrodynamic particle size. In contrast, φ decreases with H and m due to the inverse proportionality of $\tau_\perp$ to ξ. Furthermore, Eq. 2.20 clarifies that the suspension parameters, T and η, also effect the phase lag. The magnitude of the MNP magnetization possesses in comparison to φ a contrary dependence on the particle, field and suspension parameters (see Eq. 2.21). Regarding the angular frequency of the single MNPs ω_p, Zaitsev and Shliomis pointed out that it does not necessarily coincide with the angular frequency of the field ω. [108, 103]. Due to the Brownian motion of the single particles in solution their average angular frequency is reduced depending on the particle,

suspension and field parameters. Magnetic and optical measurements on diluted MNP suspensions confirmed the physical dependencies of the MNP magnetization phase lag in a RMF [116, 3]. However, it turned out that for high field magnitudes ($\xi \gg 1$) and frequencies ($\omega\tau_\mathrm{B} \gg 1$) deviations from the model appeared which are caused by the applied approximations.

2.4 Fokker-Planck equation

The thermal induced variations that occur in an ensemble of nanoparticles, the Brownian motion, can be explained by the method of Fokker-Planck [117]. This diffusion equation method results in the Fokker-Planck equation (FPE) which is a linear partial differential equation describing the temporal development of a probability density function in the presence of diffusion and drift [118]. The FPE can be applied to describe adequately the magnetization dynamics of suspended magnetic nanoparticles that are essentially affected by the Brownian motion [105, 119, 103]. Yoshida et al. [107] presented numerical solutions of the FPE adopted to MNPs in a RMF in order to determine the MNP magnetization. In this case, the FPE is defined as

$$2\tau_\mathrm{B}\frac{\partial W}{\partial t} = \frac{1}{k_\mathrm{B}t}(\nabla^2 E_\mathrm{pot})W + \frac{1}{k_\mathrm{B}T}(\nabla E_\mathrm{pot})\cdot(\nabla W) + \nabla^2 W \tag{2.24}$$

with the potential energy E_pot which is given by

$$E_\mathrm{pot}(\theta,\phi,t) = -mH\sin(\theta)\cos(\omega t - \phi) \tag{2.25}$$

and the distribution function W which - expanded into spherical harmonics - reads

$$W(\theta,\phi,t) = \sum_{n=0}^{\infty}\sum_{m=-n}^{n} a_{n,m}(t)P_n^{|m|}\cos(\theta)e^{im\phi}. \tag{2.26}$$

$P_n^{|m|}$ represents the associated Legendre functions and $a_{n,m}(t)$ the temporal coefficients of the spherical harmonics. E and W are expressed in spherical coordinates. The detailed steps of the performed numerical solution are ex-

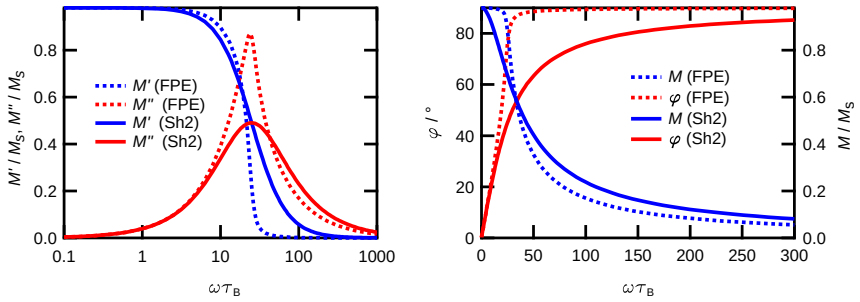

(i) (ii)

Figure 2.3: Comparison of simulation results based on numerical solution of FPE (Eq. 2.24) and magnetization equation model (Eq. 2.22 and 2.23) with perpendicular time constant (Sh2: Eq. 2.14) for $\xi = 50$ in real and imaginary part (i) as well as phase and magnitude (ii) representation. [107] © 2012, AIP Publishing LLC.

plained in [107]. The results are displayed as real and imaginary part of the MNP magnetization M' and M'' in relation to the product of angular frequency and Brownian time constant $\omega\tau_B$. In Fig. 2.3(i) one can see that M' and M'' for $\xi = 50$ exhibit curvatures qualitatively similar to the ACS spectra from section 1.2.4, however, with an imaginary part maximum around $\omega\tau_B = 20$. By comparison, the corresponding results of the magnetization equation model (Eq. 2.22 and 2.23) with the perpendicular time constant (Eq. 2.14) show a significant deviation for $\xi = 50$ (Fig. 2.3(i)). On the other hand, for small Langevin parameters ($\xi < 1$) the deviations between the numerical simulation results and the magnetization equation model are negligible [107]. The corresponding phase lags and normalized magnitudes are calculated by

$$\varphi = \arctan(M''/M') \tag{2.27}$$

and

$$M = \sqrt{M'^2 + M''^2}. \tag{2.28}$$

The phase and magnitude representation in Fig. 2.3 (ii) confirms the deviations of the linearized magnetization equation from the numerical FPE solutions. Furthermore, one can see the mentioned dependencies of the phase lag and magnitude on the field frequency and the particle hydrodynamic size because φ and M are plotted against $\omega\tau_{\mathrm{B}}$. In addition, the numerical FPE solutions have been successfully applied to describe the measured MNP magnetization dynamics in a RMF. The corresponding MNP parameters were determined with independent measurement techniques [107]. Due to the observed deviations of the linearized magnetization equation and the difficult real-time analysis of measurement results with the FPE, Yoshida et al. [107] expanded Eq. 2.22 and 2.23 for a higher modeling and analysis accuracy. These equations are stated in the following as empirical model and presented in the next section.

2.5 Empirical model

The empirical model is an extension of the Debye-like equations 2.22 and 2.23. They take the form

$$\frac{M'}{M_{\mathrm{s}}} = \frac{L(\xi)}{1+(\omega\tau_{\perp})^2}\left[\frac{1+a_4(\omega\tau_{\perp})^2+a_5(\omega\tau_{\perp})^{a_3}}{1+a_1(\omega\tau_{\perp})^2+a_2(\omega\tau_{\perp})^{a_3}}\right] \tag{2.29}$$

and

$$\frac{M''}{M_{\mathrm{s}}} = \frac{L(\xi)(\omega\tau_{\perp})}{1+(\omega\tau_{\perp})^2}\left\{b_1+b_2\frac{\left[1+(\omega\tau_{\perp})^2\right](\omega\tau_{\perp})^{(0.4b_3-1)}}{1+0.25(\omega\tau_{\perp})^{2b_3}}\right\} \tag{2.30}$$

with the Langevin parameter dependent coefficients

$$a_1 = \frac{3.76\xi^2+0.029\xi^4}{1+29.6\xi+7.61\xi^2+0.00382\xi^4}, \tag{2.31}$$

$$a_2 = 0.13\xi^{1.1}, \tag{2.32}$$

$$a_3 = 4 + 16\left(\frac{\xi}{\xi + 17}\right)^2, \tag{2.33}$$

$$a_4 = 0.1\xi, \tag{2.34}$$

$$a_5 = \frac{0.0865\xi + 0.205\xi^2 + 0.000397^4}{1 + 0.88\xi + 0.606\xi^2 + 0.00652\xi^4}, \tag{2.35}$$

$$b_1 = 1 - \frac{0.2\xi^{1.2}}{\xi^{1.2} + 5.5}, \tag{2.36}$$

$$b_2 = \frac{0.6\xi^{1.5}}{\xi^{1.5} + 16} \tag{2.37}$$

and

$$b_3 = 1.4 + \frac{3.2\xi}{\xi + 5}. \tag{2.38}$$

These equations enable a modeling of the MNP magnetization in a RMF with a high accuracy in a reasonable time. Fig. 2.4 displays a comparison of the simulation results based on the numerical FPE solution and the empirical model. For $\xi = 50$ only slight differences in the real and imaginary part as well as phase and magnitude representation are discernible. A detailed illustration of the according phase and magnitude errors of the MNP magnetization in a RMF is presented in Fig. 2.5. Here, the true value accords to the results of the numerical FPE solution. In addition to the empirical model the errors of the magnetization equation model (Eq. 2.22 and 2.23) with the two different perpendicular time constants (Eq. 2.12 and 2.15) are displayed. The analysis of the errors confirms the accuracy of the empirical model compared to the magnetization equation model. Especially, for the latter a dramatic error growth is observed when the Langevin parameter

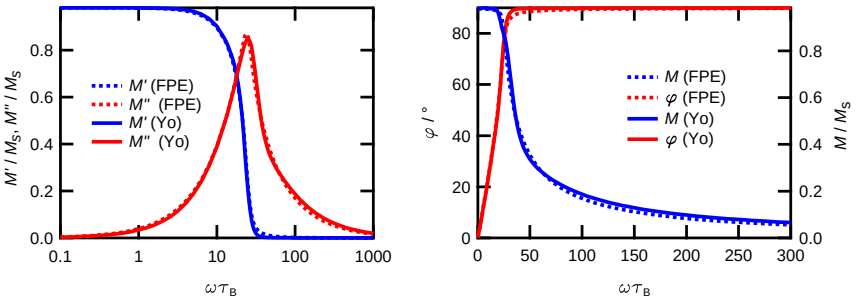

Figure 2.4: Comparison of simulation results based on numerical solution of FPE (Eq. 2.24) and empirical model (Yo: Eq. 2.29 and 2.30) for $\xi = 50$ in real and imaginary part (i) as well as phase and magnitude (ii) representation. [107] © 2012, AIP Publishing LLC.

increases from 1 to 50. Whereas for $\xi = 1$ the maximum phase and magnitude error of the magnetization equation model amount to $-1.5^\circ/-2.8^\circ$ and $3\,\%/8.6\,\%$, for $\xi = 50$ maximum errors of $-35.1^\circ/-35.6^\circ$ and $46.9\,\%/49.8\,\%$ occur. In contrast, the maximum errors of the empirical model increase only from -0.13° and $-0.12\,\%$ to 2.3° and $18.9\,\%$.

2.6 System considerations

A solution of magnetic nanoparticles dominated by the Brownian relaxation process contains frequently a small fraction of fast Néel dominated particles. Especially, particle ensembles with a mean diameter slightly larger than the threshold d_{spm} (see section 1.1.3) exhibit this effect due to their size distribution. A reduction of the core size can cause a reduced anisotropy energy, which results in a Néel particle although the majority of particles is dominated by the Brownian relaxation. Furthermore, multi-core particles can show a similar effect caused by an amount of nanocrystals in the magnetic core that are thermally not blocked. These fast particles possess a phase lag of almost zero degree in the investigated frequency range ($\omega\tau_{\mathrm{B}} < 50$) which is not affected by a change of the hydrodynamic diameter. However, they contribute to the sample magnetization and resulting magnetic flux density.

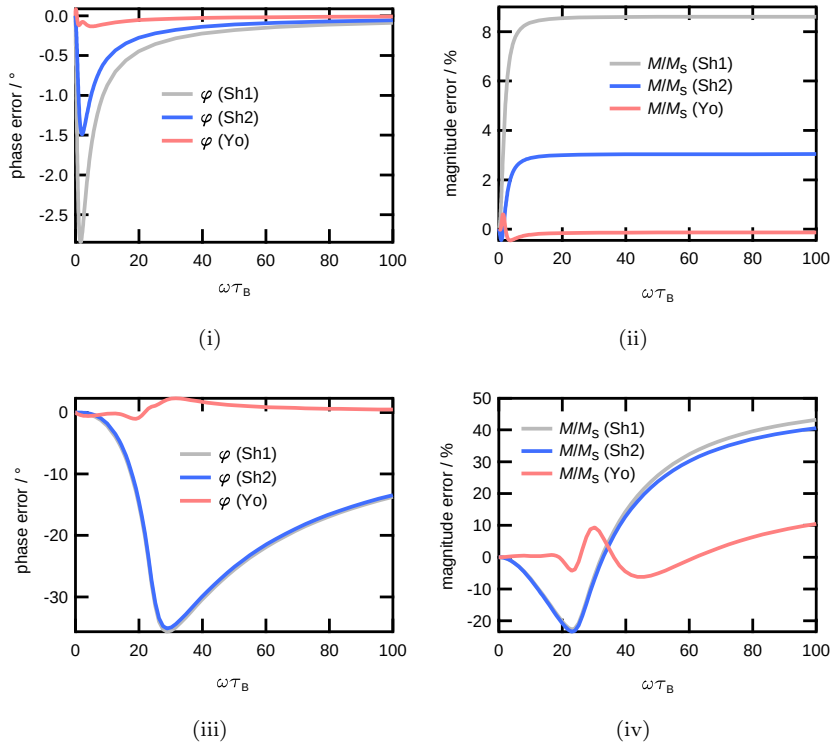

Figure 2.5: Comparison of phase and magnitude errors of simulation results based on the empirical model (Yo: Eq. 2.29 and 2.30) and the magnetization equation model (Eq. 2.22 and 2.23) with the perpendicular time constants defined by Eq. 2.12 (Sh1) and Eq. 2.15 (Sh2). The Langevin parameter ξ amounts to 1 (i+ii) and 50 (iii+iv). The true values are given by the numerical solution of the FPE.

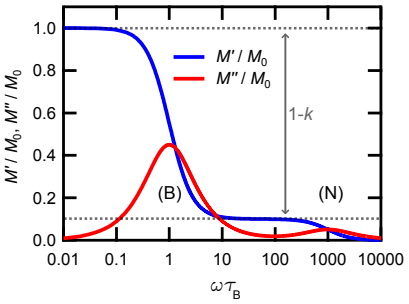

Figure 2.6: Illustration of factor k determination from the ACS spectrum for a MNP sample with Brownian relaxation dominated particles (B) and small portion of fast Néel relaxation dominated ones (N).

In order to correct this effect in the modeling the factor k is introduced:

$$k = n_{\mathrm{N}}\overline{m_{\mathrm{N}}^2} / \left(n_{\mathrm{B}}\overline{m_{\mathrm{B}}^2} + n_{\mathrm{N}}\overline{m_{\mathrm{N}}^2}\right). \tag{2.39}$$

This factor represents the relation of Néel to all particles with respect to the Néel and Brownian particle number densities n_{N} and n_{B} as well as the mean square of the corresponding magnetic moments m_{N} and m_{B} which is defined as

$$\overline{m^2} = \int_{\mathrm{m}} f_{\mathrm{m}}(m) m^2 dm. \tag{2.40}$$

Fig. 2.6 illustrates the determination of the factor k from the complex spectrum of the AC susceptibility. Hence, the imaginary part peaks of the Brown and Néel dominated particles have to be clearly distinguishable which satisfies the condition $\tau_{\mathrm{N}} \ll \tau_{\mathrm{B}}$. The factor k is then calculated from the relation between the Néel dominated particles' and whole sample's DC susceptibility. Thus, only the complete ACS of the Brownian particle fraction needs to be measured.
The developed measurement system detects the magnetic flux density B_{S} of the MNP samples. Considering the particle parameter distributions and the contribution of the fast Néel dominated particles in solution the real

and imaginary part of $B_{\mathrm{S}}(H,\omega)$ can be expressed by

$$\begin{aligned}\frac{B'_{\mathrm{S}}(H,\omega)}{B_{\mathrm{S}}(H_0,0)} &= (1-k)\frac{3k_{\mathrm{B}}T}{H_0\overline{m_{\mathrm{B}}^2}}\int_{d_{\mathrm{h}}} f_{\mathrm{h}}(d_{\mathrm{h}}) \\ &\quad\times\int_{m_{\mathrm{B}}} f_{\mathrm{m}}(m_{\mathrm{B}})m_{\mathrm{B}}\frac{M'(H,\omega)}{M_{\mathrm{s}}}dm_{\mathrm{B}}dd_{\mathrm{h}} + k\frac{H}{H_0}\end{aligned} \tag{2.41}$$

and

$$\begin{aligned}\frac{B''_{\mathrm{S}}(H,\omega)}{B_{\mathrm{S}}(H_0,0)} &= (1-k)\frac{3k_{\mathrm{B}}T}{H_0\overline{m_{\mathrm{B}}^2}}\int_{d_{\mathrm{h}}} f_{\mathrm{h}}(d_{\mathrm{h}}) \\ &\quad\times\int_{m_{\mathrm{B}}} f_{\mathrm{m}}(m_{\mathrm{B}})m_{\mathrm{B}}\frac{M''(H,\omega)}{M_{\mathrm{s}}}dm_{\mathrm{B}}dd_{\mathrm{h}}\end{aligned} \tag{2.42}$$

normalized to the sample's magnetic flux density for a given DC excitation field H_0 which is defined by

$$B_{\mathrm{S}}(H_0,0) = n_{\mathrm{B}}\overline{m_{\mathrm{B}}^2}\frac{gH_0}{3k_{\mathrm{B}}T} + n_{\mathrm{N}}\overline{m_{\mathrm{N}}^2}\frac{gH_0}{3k_{\mathrm{B}}T}. \tag{2.43}$$

The factor g represents the geometries and the arrangement of the sensor and sample, which influence the strength of B_{S} coupling into the sensor.

3 Measurement system

In this chapter, the developed measurement system for the investigation of the dynamics of magnetic nanoparticles in a rotating magnetic field is presented. First, the system requirements are defined. Then, the hard- and software components, e.g. the coils, sensors and control program, as well as their interaction are explained. Finally, the performance of the measurement system is characterized regarding systematic and random errors and a maximal measurement uncertainty of the phase lag determination for a defined set of measurement parameters is estimated.

3.1 System requirements

In order to investigate the rotational dynamics of MNPs as potential markers for a homogeneous bioassay based on a RMF, the magnetic field generation and the detection system need to fulfill some requirements. These are the RMF frequency range, magnitude and homogeneity as well as the sensor noise performance, frequency bandwidth and geometry. Furthermore, practical aspects as the sample handling and environmental influences have to be taken into account.

Rotating magnetic field

The hydrodynamic size and the magnetic moment define the modified Brownian relaxation time constant $\tau_\perp$ of MNPs in a RMF (see Eq. 2.15) assuming that they are dissolved in an aqueous medium at room temperature. Thus, the minimum upper frequency of the measurement system is specified by these parameters corresponding to Eq. 1.28 which defines a relation between $\tau_\perp$ and the modified characteristic frequency $f_{\mathrm{ch},\perp}$. In addition, $\tau_\perp$ incorporates the RMF magnitude via the Langevin parameter. Hence, the magnitude has an additional influence on $f_{\mathrm{ch},\perp}$. Fig. 3.1 depicts the modified characteristic frequency as a function of the hydrodynamic diameter and the Langevin parameter for spherical particles. While for $\xi < 1$ field

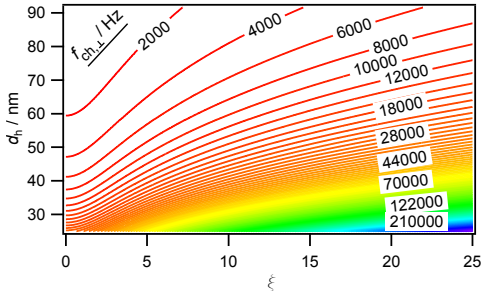

Figure 3.1: Characteristic frequency $f_{\mathrm{ch},\perp}$ as a function of the hydrodynamic diameter d_h and the Langevin parameter ξ for spherical magnetic nanoparticles suspended in an aqueous medium with $\eta = 1\,\mathrm{mPa\,s}$ and $T = 300\,\mathrm{K}$.

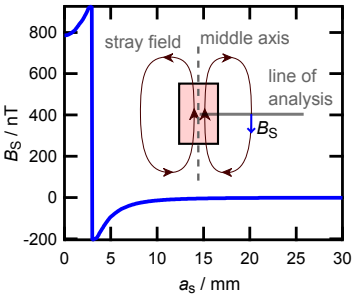

Figure 3.2: Simulated stray field B_S of iron oxide single-core particle sample ($d_c = 30\,\mathrm{nm}$, $c(\mathrm{Fe}) = 0.5\,\mathrm{g/L}$) in a 1 mT field plotted against the distance to the middle axis a_s. The schematic illustrates the location of the analyzed stray field.

frequencies of up to 10 kHz facilitate the investigation of particles with hydrodynamic diameters down to 35 nm, the same frequency scope results for $\xi = 20$ in a significantly increased lower limit of 75 nm. The initial motivation of this measurement system development is based on the investigation of elongated cobalt nanoparticles with a hydrodynamic length of 90 nm and diameter of 16 nm [3] which results in a modified characteristic frequency of 2.3 kHz for $\xi = 1$. With a system frequency range of 1 Hz to 5 kHz a measurement of the complete spectrum of the magnetization dynamics is ensured and even smaller particles can be analyzed. The field strength required for a Langevin parameter $\xi = 1$ amounts in the case of the elongated cobalt particle to 1.3 mT. Hence, a maximum system field strength of up to 10 mT fulfils this requirement and additionally enables the investigation of the magnetization dynamics field dependence. Finally, a homogeneous magnetic field has to be generated in the area of the MNP sample. Deviations of the field magnitude from its desired value smaller than 1 % are necessary to ensure the negligence of disturbing field components and guarantee the applicability of the physical model for the description of the measurement results.

Detection

The main requirements of the sensor system for the detection of the MNP dynamics are given by the system frequency range (sensor bandwidth) and the magnetic flux density B_S induced by the MNP ensemble magnetization (magnetic noise). Furthermore, geometric aspects have to be considered due to limited space in the measurement system and the desired sample handling (sensor geometry). The frequency range has been discussed in the former section and was defined to range from 1 Hz to 5 kHz. The measurement quantity B_S depends on the particle magnetic moment and concentration, which define the sample magnetization (see Eq. 1.6). Additional influences result from the RMF magnitude and the spatial measurement arrangement, e.g. the distance between sample and sensor. With the discussed field magnitudes of up to 10 mT B_S depends strongly on the investigated sample. In the case of highly concentrated samples ($\phi \gg 0.1$) with a high M_s, flux densities in the millitesla range can be detected in close proximity to the sample. On the other hand, for samples with comparable low particle concentrations ($\phi \ll 0.1$), as they are subject of this research, flux densities in the nanotesla range can be induced. Fig. 3.2 displays the simulated stray field of a sample with iron oxide single-core particles possessing a core diameter of 30 nm and an iron concentration c(Fe) of 0.5 g/L ($\phi = 0.014$) in a homogeneous 1 mT field. This simulation was performed with the program FEMM [120] and is based on a magnetization curve measurement of the corresponding sample with a MPMS. The stray field along the blue line is plotted over the distance a_s to the sample's middle axis. Inside the sample solution, B_S amounts to field strengths of more than 800 nT. However, outside the sample a maximum value of 200 nT is observed and decays quickly in accordance with the $1/a_\mathrm{s}^3$ dependence of a magnetic dipole far field [121]. The size of the sensor geometry is directly limited by the size and arrangement of the field generation unit. In this work, the desired field homogeneity requires a coil system with minimum radii of some centimeters. Thus, the upper sensor geometry limit lies in the same range. The handling of the samples is discussed in the following section.

Sample handling

Fig. 3.3 displays the two types of vials that are applied for the measurement of the MNP magnetization dynamics in MRX and ACS as well as the storage of the samples in a cooled environment. The left vial is manufac-

tured out of glass and closed with a polyethylene cap. The outer diameter amounts to 7.8 mm and the height is 35 mm. It is distributed by the neoLab Migge Laborbedarf-Vertriebs GmbH (Heidelberg, Germany) under the identifier 7-0736. The right vial is a conical polystyrene vessel manufactured by the Nunc GmbH & Co. KG (Wiesbaden, Germany) under the brand BreakApart^{TM} PolySorp^{TM}. It is sealed with a blue polyethylene cap. The largest diameter of this vial is found in the height of the cap with 8.8 mm. Both vial types have to fit into the measurement system. In addition, a fast and uncomplicated change of the samples in the system has to be enabled. In the optimal case, the sample can be placed manually into the measurement system in one step.

3.2 Hardware and Construction

A sketch of the measurement system hardware and interplay of the components, which fulfill the described requirements, can be found in Fig. 3.4. A photograph of the whole system including all components is shown in Fig. 3.5. It consists of a 2-axis Helmholtz coil system that is powered by a current control unit for the generation of a rotating magnetic field. Inside the coil system two fluxgate magnetometers are set up in a gradiometric arrangement. Between these two sensors the sample is placed in a holder which can control the sample temperature and position along the sensitive measurement axis of the fluxgate magnetometers. Additional electronics and a measurement and control interface, which is equipped with analog-to-digital as well as digital-to-analog converters, enable an automation of the whole measurement process. A side and top view of the system with the gradiometric fluxgate arrangement in the center of the 2-axis Helmholtz coil is displayed in Fig. 3.6 and 3.7.

3.2.1 Fluxgate magnetometer

The utilized fluxgate magnetometer system MAG-03IEL from Bartington Instruments Limited (Witney, United Kingdom) provides magnetic sensors which facilitate the measurement of weak magnetic fields down to the picotesla range at room temperature. Their magnetic noise amounts to values smaller than $< 6\,\mathrm{pT}/\sqrt{\mathrm{Hz}}$ at 1 Hz and the frequency bandwidth ranges from DC to 5 kHz. A list with further parameters is shown in Table 3.1 [123]. The whole sensor system consists of three single sensors, each housed in-

Figure 3.3: Photograph of sample vials utilized for measurements on magnetic nanoparticle suspensions.

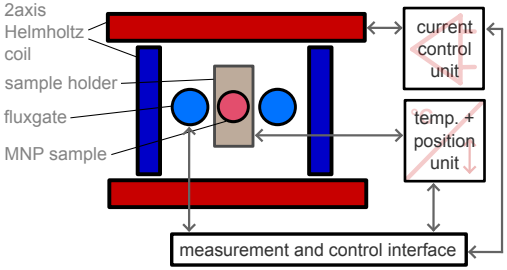

Figure 3.4: Schematic of the measurement system with interaction between the single components.

Figure 3.5: Photograph of RMF measurement system with all components.

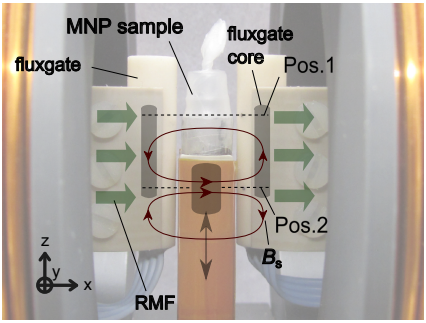

Figure 3.6: Side view of the measurement system. A MNP sample is placed between two fluxgates. The stray field of the sample is coupling into the fluxgate cores with respect to the sample position. [122] © 2014, AIP Publishing LLC.

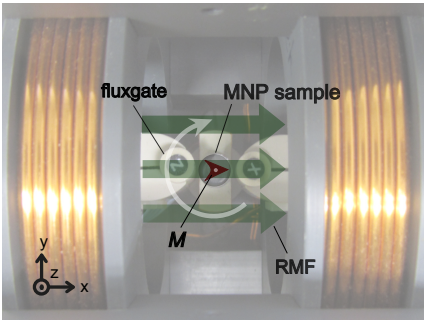

Figure 3.7: Top view of the measurement system. A MNP sample is placed between two fluxgates. A homogeneous RMF is aligning the sample magnetization.

side a ceramic cylinder with an diameter of 8 mm and a length of 30 mm. The construction of the single sensor unit is illustrated in Fig. 3.8 and called Vacquier type. Here, the two magnetic cores are excited by their primary coil fields in opposite directions, however, with the same symmetric saturated magnetization profile. These non-linear core magnetizations compensate each other in the absence of an external magnetic field. In the presence of a field, the magnetization profiles do not coincide anymore and the detection coil wound around this configuration detects a signal which can be analyzed to determine the causative field. In practice, the second harmonic of the measurement coil‘s output signal is processed which occurs only in the presence of the external magnetic field. The compensation coil extends the linear measurement range of the sensor by keeping the cores’ magnetization profile symmetric. A detailed explanation of fluxgates, their different configurations and operation is given by Ripka [124]. The three sensor units are connected with a measurement and supply electronics. Two units are used for the gradiometric arrangement which is shown in Fig. 3.6. The stray field of a MNP sample placed in between couples into the sensor on the left side with an reversed direction compared to the one on the right side. If the output signals of the two units are subtracted from each other, power line interferences, the DC earth magnetic field and other global

disturbances are compensated and the signal caused by the sample is doubled. This gradiometric measurement results in a more robust measurement process which enables an operation of the measurement system outside a magnetic shielding. The signal-to-noise ratio (SNR) is increased by a factor of $\sqrt{2}$ [125]. The relative height (z-position) of the sample with respect to the cores in one unit defines the direction of the coupling stray field. Thus, the gradiometric signal in the upper position (Pos.1, Fig. 3.6) posseses an reversed direction compared to the lower position (Pos.2, Fig. 3.6). Therefore, it is important to align the two sensor units with respect to their core positions inside the coil system and not with respect to the ceramic cylinder. The ends of the cores in each unit are determined with the help of a small magnetic dipole which is moved along the sensors measurement axis (z-direction). The relative position of each end causes a maximum in the sensor's output signal. The existence of these two positions (Pos.1 and Pos.2) facilitates a further improvement of the measurement process, if one measurement in each position is performed and both signals are subtracted from each other:

$$U_{\mathrm{out}} = (U_{\mathrm{x,1}} - U_{\mathrm{z,1}}) - (U_{\mathrm{x,2}} - U_{\mathrm{z,2}}) = 4U_{\mathrm{MNP}}. \tag{3.1}$$

The output signal of this measurement procedure U_{out} equals the signal induced by a MNP sample in one sensor U_{MNP} multiplied by four, if the single signals of fluxgate X and Z in the positions Pos.1 and Pos.2 $U_{\mathrm{x,1}}$, $U_{\mathrm{z,1}}$, $U_{\mathrm{x,2}}$ and $U_{\mathrm{z,2}}$ correspond to U_{MNP} as follows

$$U_{\mathrm{x,1}} = U_{\mathrm{z,2}} = U_{\mathrm{MNP}} \tag{3.2}$$

and

$$U_{\mathrm{x,2}} = U_{\mathrm{z,1}} = -U_{\mathrm{MNP}}. \tag{3.3}$$

Besides the amplification of the measurement signal, this process compensates again environment and system disturbances and facilitates an automated repetition of the sample measurement. The components providing the positioning of the sample in the z-direction are presented in section 3.2.4. If quick measurement repetitions are required or a movement of the sample should be avoided, the positioning unit can be deactivated and the

Table 3.1: Parameters of 3-axes fluxgate magnetometer MAG-03IEL.

bandwidth:	0 kHz to 5 kHz
measurement range:	±100 µT
sensitivity:	$10^5 \frac{\mathrm{V}}{\mathrm{T}}$
magnetic noise (at 1 Hz):	$< 6\,\mathrm{pT}/\sqrt{\mathrm{Hz}}$
zero field offset:	<5 nT

measurement in the second position is replaced by a measurement without sample (blank measurement). This procedure is analogous to the one of the fluxgate based MRX measurement system [83].

The sensor units are oriented perpendicularly to the plane of the rotating magnetic field, so that the sensors measure only the magnetic nanoparticle's stray field. Otherwise the sensors measurement range would be exceeded by the coupling component of the RMF H_{par}. Due to production inaccuracies, the cores in the fluxgate units are not perfectly orientated parallel to the axis of the ceramic cylinder (see Fig. 3.9). Thus, the sensor units have to be aligned manually into their vertical positions with the help of special sensor mountings. Applying a rotating field with a magnitude of 1 mT, the field H_{par} detected by each single fluxgate in the absence of a sample can be minimized to below 100 nT, i.e., the sensors can be balanced to better than $1 \cdot 10^{-4}$. This corresponds to a tilt angle α_{T} of less than 0.003° which is defined by

$$\alpha_{\mathrm{T}} = \arcsin\left(\frac{H_{\mathrm{par}}}{H}\right). \tag{3.4}$$

The limited fluxgate frequency bandwidth causes a frequency response of the single sensor units, that results in a significant phase shift and magnitude drop. The measured frequency response of the sensor units X and Z is presented in Fig. 3.10. Whereas the magnitude drops at 5 kHz to 70 % of its start value which is in agreement with the specified −3 dB cutoff frequency, the phase shifts to almost 180°. Thus, the frequency response of the fluxgates has to be corrected to ensure an exact determination of the phase and magnitude of the MNP samples. The applied software procedure is explained in section 3.3.2. Measurements describing the influence of the RMF on the sensor's frequency response are presented in section 3.4.1.

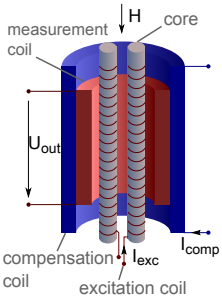

Figure 3.8: Principle setup of fluxgate magnetometer with double core (Vacquier) configuration and compensation coil.

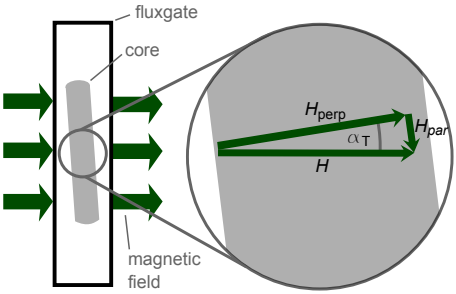

Figure 3.9: Component H_{par} of magnetic field H coupling into misaligned fluxgate core. The tilt angle α_{T} defines the misalignment and the relative strength H_{par}/H.

The fluxgate sensor units induce stray fields via their compensation coils. Whereas the effect of this field on the sample was studied in the absence of an exciting magnetic field for a fluxgate-based MRX system [83] and found to be subordinate, it was not investigated in the presence of a rotating magnetic field. In the ideal case of a perfect perpendicularity between the sensor axis and the RMF plane, no stray field is induced. However, the existing tilt angle and the coupling RMF component H_{par} cause a stray field. Fig. 3.11 (i) illustrates a measurement arrangement of the corresponding analysis. A pick up coil with the geometry of the desired 150 µL samples is placed between the two fluxgate units and detects the sensor stray field in the z-direction while a rotating field is generated. In order to eliminate any component of the RMF seen by the pick up coil, the voltage difference between measurements with fluxgates switched on and off is calculated. The measurement results in Fig. 3.11 (ii) show a negligible voltage difference compared to the induction voltage u_{AC} of the pick up coil in a 1 mT AC field. Measurements with the pick up coil in the x- and y-direction result in a similar relation of the possible stray field and RMF excitation. The maximum relation of $\Delta u/u_{\mathrm{AC}}$ amounts to $1 \cdot 10^{-3}$ for all configurations and frequencies larger than 1 kHz. Thus, no significant stray field component from the sensor is present which may affect the whole sample and cause noticeable errors in the RMF excitation.

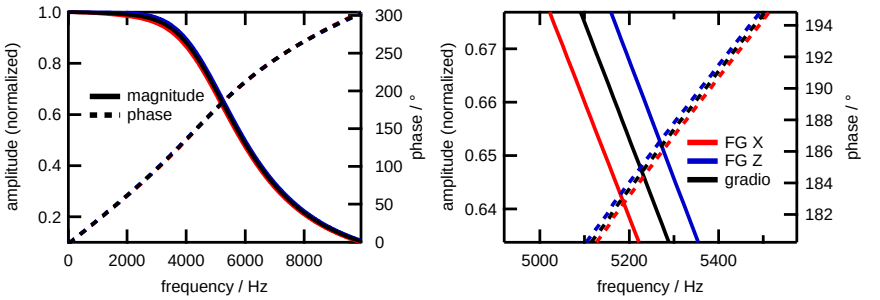

(i) (ii)

Figure 3.10: Measured frequency response of fluxgate X and Z as well as their gradiometric configuration in a wide (i) and narrow (ii) frequency range. The amplitudes are normalized to the dc value.

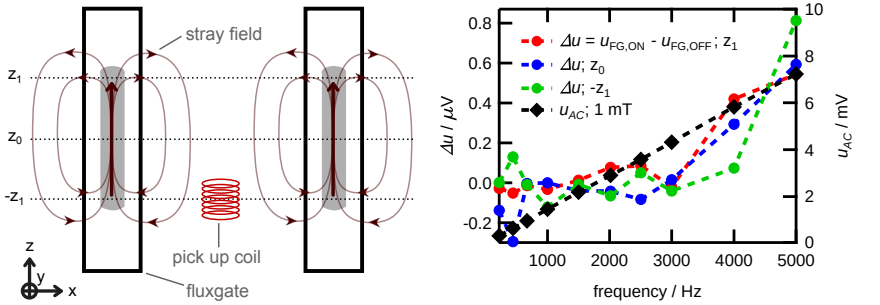

(i) (ii)

Figure 3.11: (i) Schematic of pick up coil measuring the fluxgate stray field in z-direction induced by a perpendicular rotating magnetic field. (ii) Voltage difference Δu of pick up coil between measurements with fluxgates switched on and off for different heights and as a function of frequency. The RMF magnitude amounts to 1 mT. For comparison the coil's induction voltage in a homogeneous 1 mT AC field is shown.

3.2.2 2-axis Helmholtz coil system

Rotating magnetic fields can be realized with permanent magnets [126, 127] or electromagnets [14, 128]. The application of permanent magnets enables the generation of high field strengths ($\mu_0 H \gg 10\,\mathrm{mT}$), however, results in limited field homogeneities. Furthermore, for the rotation an electromotive unit is required, whose rotational frequency is limited by its mechanics. The operation of a coil system also necessitates additional hardware, e.g. an electrical unit which provides the coil current. Here, the resulting maximum current of the system restricts the field strength. However, the operation of rotation frequencies of 5 kHz and more requires less effort compared to a permanent magnet in combination with an electromotive unit. In addition, less vibrations are induced which reduces mechanical disturbances.
In this work, Helmholtz coils are applied which consist of a pair of identical coils with a middle radius r_{coil} and facilitate the generation of a homogeneous magnetic field [129]. The cross-sectional area of an corresponding field simulation is presented in Fig. 3.12. The space between the two single coils displays the relative homogeneous area, whose optimum is achieved for a distance between the two coils equal to their radius. Consequently, the sample has to be placed in this center. For the generation of the rotating magnetic field, a second, larger Helmholtz coil is set up perpendicular to the first one. If both coils are driven by sinusoidal currents with a phase shift of 90° to each other, a rotating magnetic field results (see Eq. 2.1). Fig. 3.13 depicts a schematic of this configuration with an illustration of the corresponding field components H_{S1} and H_{S2} of the small (S1) and large (S2) Helmholtz coil. The superimposition of these two components results in a RMF with a constant field magnitude H_{RMF}.
The mechanical and electrical parameters of the single coils are summarized in Table 3.2. The given radii and number of windings are optimized with respect to the required space, field homogeneity, field strength and frequency range. The material of the coil bodies is polyvinyl chloride (PVC) and the windings consist of a 2 mm diameter copper wire. The electrical parameters result in a resonance frequency of the single Helmholtz coils which is significantly larger than the system's maximum frequency of 5 kHz. Fig. 3.14 displays the measured absolute value of the coil impedances. Here, one can see a resonance frequency of 1.02 MHz and 0.66 MHz for S1 and S2, respectively. The field homogeneity was determined by simulating the field distribution of the two coils as shown in Fig. 3.12. In a cylindrical space with a length and diameter of 20 mm lying on the axis of the Helmholtz

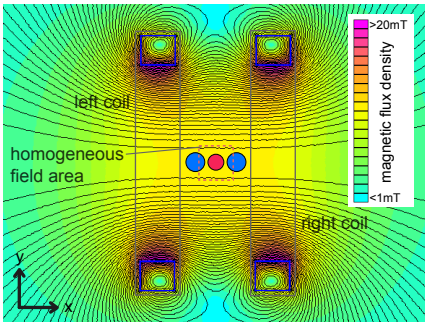

Figure 3.12: Simulated magnetic flux density distribution of small Helmholtz coil (S1). The blue squares represent the winding package cross sections and the black lines the field distribution.

Table 3.2: Parameters of the 2-axis Helmholtz coil system.

Parameter	coil S1	coil S2
middle radius r_{coil}:	50 mm	67.5 mm
number of windings N_{coil}:	39	46
resistance R_{coil}:	267 mΩ	247 mΩ
inductance L_{coil}:	433.7 µH	881.9 µH
capacity C_{coil}:	56.6 pF	65.6 pF
coil constant k_{coil}:	0.707 mT/A	0.613 mT/A

coil in the center of the system a maximum deviation from the desired field component in the direction of the coil axis of 0.3 % (S1) and 0.15 % (S2) was found. The maximum component perpendicular to the coil axis amounts to 0.25 % (S1) and 0.05 % (S2) of the desired field strength. Thus, negligible field inhomogeneities exist and guarantee a correct modeling of the magnetization dynamics in a RMF.

3.2.3 Current control

The coil current is provided by the high power operational amplifier DCP780 from SERVOWATT Gmbh (Gerlingen, Germany). The amplifier's rated permanent current is ±15 A with a maximum permanent output voltage of ±50 V and a power bandwidth of 25 kHz. The circuit of the amplifier unit is

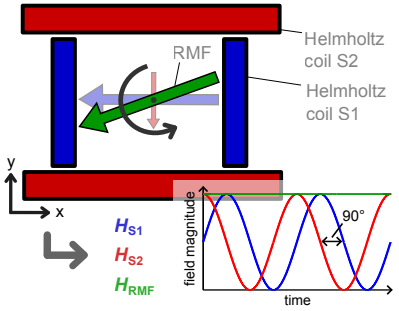

Figure 3.13: Schematic of the RMF generation with two perpendicular Helmholtz coils. The inset shows the field magnitudes of the single Helmholtz coil fields and the resulting RMF.

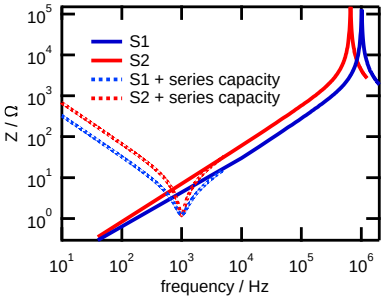

Figure 3.14: Absolute value of measured impedance of Helmholtz coil S1 and S2 with and without series capacity as a function of frequency.

shown in Fig. 3.15. The circuit is identical for both coils except capacity C_g. It amounts to 470 pF for coil S1 and to 1 nF for coil S2. With this circuit the amplifier behaves as a current regulator. The current of the amplifiers load, the coil current I_{coil}, is directly defined by the input voltage U_{in}:

$$I_{coil} = -U_{in} \frac{R_1}{R_2 R_{shunt}}. \tag{3.5}$$

The amplitude response of this current regulator possesses in practice errors of up to 10 %. Hence, the magnitude of the single coil currents $I_{coil,S1}$ and $I_{coil,S2}$ as well as the phase between these currents is controlled additionally by a proportional-integral (PI) controller implemented in the measurement and control software (see section 3.3). The maximum field frequency as a function of the field strength which can be generated by one coil and the corresponding current control unit is illustrated in Fig. 3.16. Coil S2 in combination with the presented current control unit limits the maximum RMF frequency for a given field strength due to its higher impedance. Whereas for 1 mT a 5 kHz field can be generated, for 5 mT it is restricted to 1 kHz. In order to overcome the limiting coil impedance, for distinct frequencies (1 kHz to 5 kHz with a step size of 0.5 kHz) series capacities can be activated, which - in the ideal case - reduce the absolute value of the coil impedance for one frequency to its real part R_{coil}. This is shown in Fig. 3.14 for 1 kHz

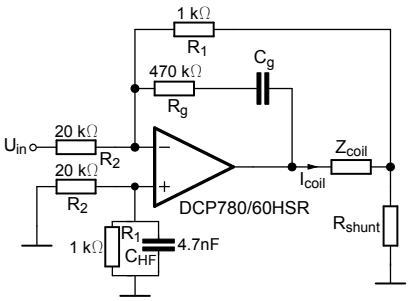

Figure 3.15: Circuit of current control unit based on high power operational amplifier DCP780.

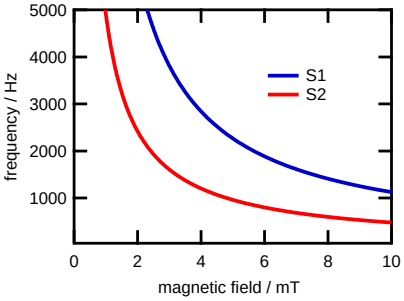

Figure 3.16: Calculated maximum field frequency of Helmholtz coil S1 and S2 in combination with current control unit as a function of field strength.

and enables with this system the generation of a RMF with a permanent maximum magnitude of 9.1 mT up to 5 kHz. The activation of the series capacities is realized with capacity switches that are automatically controlled by the measurement and control software.
The relative errors of the 90° phase shift between the single coil fields and the resulting RMF magnitude plotted against the angle φ_H of the RMF vector are displayed in Fig. 3.17. The measurements were performed with a pick up coil which is mounted inside a glass vessel and whose geometry accords with the standard 150 µL sample volume. The presented values are based on the average of the relative error of eleven different measurements with increasing frequency. The error bars represents the average deviation between these measurements. Whereas the phase error is almost negligible, the magnitude possesses slight errors of up to 2 % depending on the field angle.

3.2.4 Automatic sample positioning

A software-controlled positioning of the sample along the system's z-direction offers the possibility to perform the described measurement procedure with the two sample positions Pos.1 and Pos.2 (see Fig. 3.6) fully automated. The hardware required for this automation consists of the stepper motor QSH4218 and the driver IC TMC261 from Trinamic Motion Control GmbH & Co. KG (Hamburg, Germany) as well as a mechanical unit (Fig. 3.18)

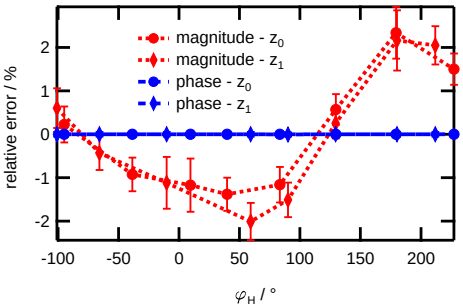

Figure 3.17: Relative phase and magnitude error of 1 mT RMF measured with a pick up coil at different field angles φ_H and the two heights z_0 and z_1. The values represent the average of the relative error of eleven measurements with various frequencies in the range from 22 Hz to 5000 Hz. The error bars correspond to the relative average deviation between the frequencies.

and limit switches with a corresponding electronics. The driver IC communicates directly via the Serial Peripheral Interface (SPI) with the measurement and control software. The limit switch signals are additionally monitored by the software in order to calibrate the sample position and prevent it from mechanical damages. A detailed description of the single components is given by Markiewicz [130].
The unit can position the sample in a range from 0 mm to 24.5 mm with a minimal step size of 0.02 mm. For a twenty-five time repeated positioning process over the whole range no missing step could be detected. Fig. 3.19 presents the output signal of the gradiometric fluxgate arrangement detecting a test sample in a 1 mT RMF with a frequency of 666 Hz in different z-positions. The recorded signal shows two maximums which correlate with the measurement positions Pos.1 and Pos.2 and confirm the determined end positions of the fluxgate cores. Thus, for each sample geometry this trace is recorded and analyzed regarding the two positions with the highest output signal.

3.2.5 Sample temperature control

The sample temperature represents an important parameter which affects the magnetization dynamics of a MNP ensemble. Thus, it is important to control this parameter and ensure a correct modeling of the measurement

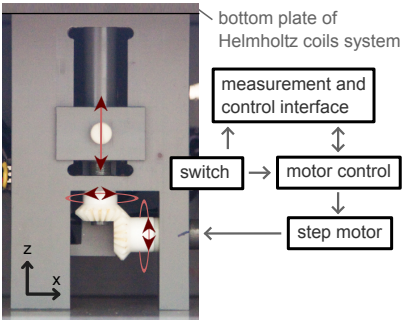

Figure 3.18: Photograph of sample positioning mechanics. The rotation of the horizontal drive shaft is transfered to the vertical shaft inducing an movement of the MNP holder in the z-direction. The step motor is controlled by two limit switches and a motor control electronics.

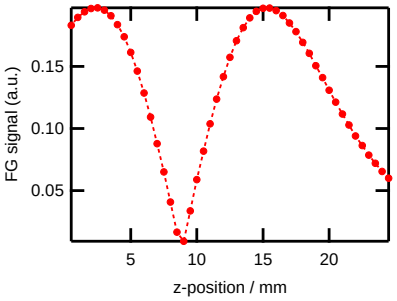

Figure 3.19: Output signal dependence of gradiometric fluxgate (FG) arrangement on MNP sample z-position. The sample is excited in a 1 mT RMF with a frequency of 666 Hz and the amplitude induced by the sample stray field coupling into the fluxgate sensors is recorded.

data. In addition, a controlled change of this temperature enables the investigation of the magnetization temperature dependence.
The system's sample holder, shown in Fig. 3.20, is manufactured from the non-magnetic material SHAPAL^{TM}. This is an aluminum nitride ceramic with a comparably high thermal conductivity of 90 W m^{-1} K^{-1} which lies in the range of metals, e.g. iron or brass. The holder is designed to place the sample between the two sensor units as close as possible to the sensor housing. Therefore, a thin wall of less than 1 mm can be found on the sides where the sensors are positioned. The two other sides of the holder have a width of 6 mm to ensure a good heat transfer from the heating coil on the bottom to the sample on the top of the holder. In addition to the distance of 90 mm between sample and coil, a bifilar winding compensates the magnetic field of the heating coil current and prevents the measurement process from magnetic disturbances. The windings of the heat coil consists of constantan. The coil current is provided and controlled by the circuit shown in Fig. 3.22, which is based on a MOSFET and operational amplifier. A resistance temperature sensor of the type PT100 is mounted inside the sample holder close to the heating coil in order to monitor the holder temperature T_{SH}. Due to heat dissipation along the ceramic, T_{SH} and the sample temperature

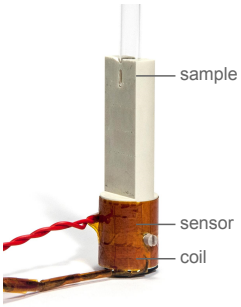

Figure 3.20: MNP sample holder manufactured from SHAPAL™.

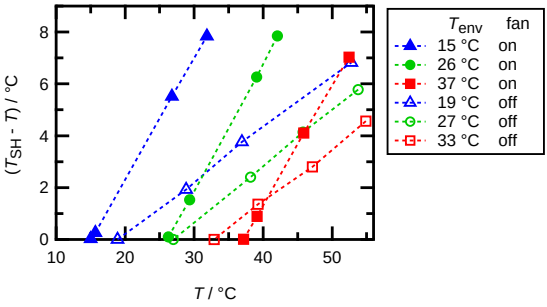

Figure 3.21: Temperature drop between sensor and sample ($T_{SH} - T$) depending on the sample temperature for different environment temperatures with and without convection (en-/disabled fan).

T do not coincide. The difference between these temperatures was measured and analyzed for different environment temperatures T_{env} with and without convection induced by a fan (see Fig. 3.21). The temperature difference can be described as a linear function of T with T_{env} as an offset. The slope of this function depends in a first approximation only on a possible convection in the sample holder environment. With a container around the measurement system external convection can be reduced to a negligible level and the temperature T_{SH} which needs to be controlled to achieve the desired sample temperature can be described by

$$T_{SH} = 0.1973(T - T_{env}) + T. \tag{3.6}$$

The control of T_{SH} is performed by a PI software controller. An analysis of this process and the sample's temperature response yields an heating up process time of 20 min to guarantee for the whole temperature range a stabilized sample temperature. Finally, T can be controlled in a range from T_{env} to $T_{env} + 40\,°C$. Taking into account the uncertainties of the sensors and the control process as well as environmental disturbances and the inhomogeneity of the sample's temperature distribution an overall uncertainty of $\pm 1\,°C$ can be assumed. A detailed description and analysis of this sample temperature control unit is given by Streibel [131].

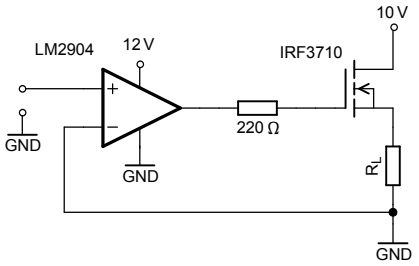

Figure 3.22: Circuit of heating coil current control based on MOSFET and operational amplifier.

3.2.6 Measurement and control interface

The measurement and control interface consists of the data acquisition cards PCIe-6323 and PCI-4462 (Table 3.3 [132]) from National Instruments (Austin, Texas, USA). The PCI-4462 card is utilized to record the output signals of fluxgate X and Z as well as the current signals of Helmholtz coils S1 and S2 via its four 24 bit analog inputs with a sampling rate of 200 kS/s. Due to a voltage noise of $S_\mathrm{v}(1\,\mathrm{kHz}) \leq 8\,\mathrm{nV}/\sqrt{\mathrm{Hz}}$ and an interchannel phase mismatch of 0.015° (gain: 0 dB) an adequate signal sampling for the determination of the phase lag and magnitude of signals in the milli- and upper microvolt range is guaranteed. Additionally, a maximum crosstalk of −138 dB and a simultaneous sampling prevent the signal analysis from significant systematic phase errors originating from the interface. The control of the coil currents, sample position and temperature is realized with the 16 bit resolution in- and outputs as well as the digital interface of the PCIe-6323 card. Both acquisition cards are synchronized via the Real Time System Integration (RTSI) bus and housed inside an desktop computer.

3.3 Software

The software program controlling the measurement process and analyzing the detected signals is based on the graphical programming environment LabVIEW from National Instruments. An interface for the direct communication with the data acquisition cards is directly integrated in LabVIEW. In the following sections the main concept of the measurement and control

Table 3.3: Parameters of measurement and control interface.

Parameter	PCIe-6323	PCI-4462
resolution:	16 bit	24 bit
analog inputs (AI):	16	4
analog outputs (AO):	4	-
simultaneous sampling:	no	yes
maximum AI sampling rate:	250 kS/s	204.8 kS/s
maximum AO sampling rate:	900 kS/s	-
multiplexer settling time:	4 µs to 7 µs	-

program is explained. In addition, the subroutines are described in detail, which directly affect the correct determination of the phase lag.

3.3.1 Concept

The principle sequence of operations of the measurement and control program is presented in Fig. 3.23. First, the sample positioning unit needs to be initialized. This incorporates the exact determination of the 0 mm z-position via the limit switches as well as the positions Pos.1 and Pos.2 for the given sample geometry. If samples with the same volume and vial have been investigated, this step can be omitted and the old positions loaded. Then, the desired sample temperature has to be set. After the sample holder reaches its temperature T_{SH}, the measurement parameters can be chosen, e.g. the field frequencies and magnitude, the number of measurement repetitions N or the measurement time of the single frequency steps. The Helmholtz coil currents are controlled by a PI software controller with respect to their magnitudes and a phase shift of 90° between each other. The resulting control values can be saved for the measurement repetitions. Finally, the measurement index i is set to one and the RMF measurement is started. Thereafter, the sample is moved to position Pos.1, the controlled RMF with the set frequencies is generated and the output signals of fluxgate X and Z as well as the coil currents $I_{\mathrm{coil,S1}}$ and $I_{\mathrm{coil,S2}}$ are recorded. Then, the sample is moved to position Pos.2 and the RMF measurement is repeated. In a next step the measurement index is increased and compared to N. If the index is less than N, the described measurement process is repeated. Otherwise, the recorded signals are filtered, if the subroutine is activated. The gradio-

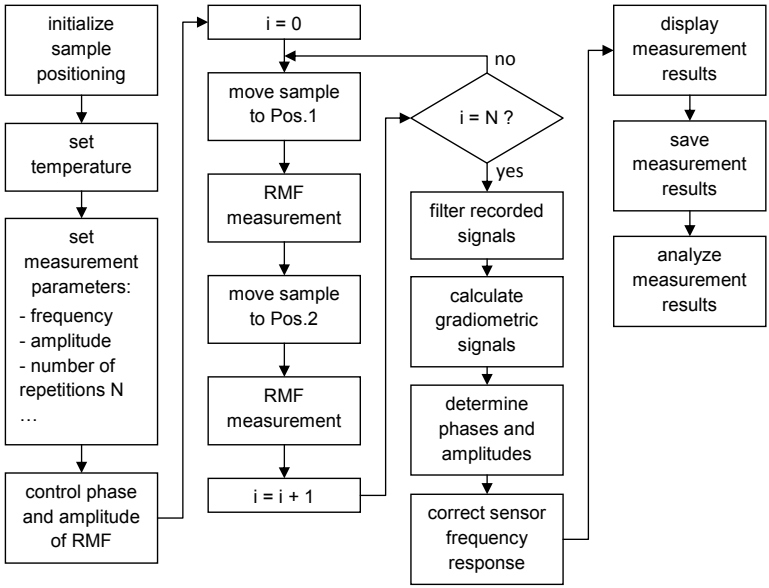

Figure 3.23: Principle sequence of operations of measurement and control program.

metric signals are calculated according with Eq. 3.1 for each measurement process. Then, the phase and magnitude are determined for each process via the calculation of the cross-spectral density. The frequency response of the fluxgates, which influences the measurement results, is corrected and the phase and magnitude spectra of the single measurement processes can be displayed, saved and analyzed.

3.3.2 Data processing

The recorded data, the fluxgate signals and the coil currents, are processed in order to accurately determine the phase lag between the sample magnetization and the RMF vector, which correlates with the phase shift between the measured sensor and coil time signals. In addition, the magnitude of all signals is determined. The frequency of the analyzed phase and magnitude coincides with the RMF excitation frequency. A sample rate of 200 kS/s, which is set for the data acquisition, clearly satisfies the Nyquist–Shannon

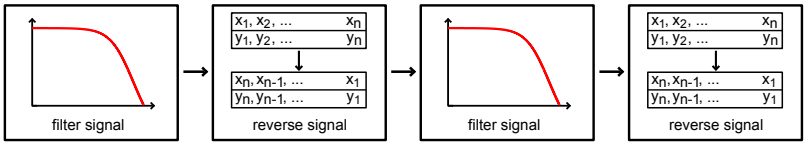

Figure 3.24: Zero-phase filter based on bidirectional filtering technique.

sampling theorem since the system's maximum frequency amounts to 5 kHz. In a first step, the signals can be filtered with a zero-phase filter to suppress disturbing frequency components, e.g. the fluxgate excitation frequency of 15.8 kHz. The filter facilitates a graphical analysis of the single signals. However, it is not necessary for the automated determination of the phase lag via the calculation of the cross-spectral density. The magnitudes are extracted from a fast Fourier transform (FFT) analysis. Finally, a correction of the fluxgate frequency response is realized via a look-up table and interpolation approach.

Digital filter

The amplitude and phase response of a signal filter follow different curve progressions. Often, the phase of the filter's transfer function starts to change at lower frequencies compared to the magnitude. In the case of a first-order low pass filter the magnitude is diminished by 0.5 % at one tenth of the cut-off frequency, whereas the phase changed from 0° to −5.7°. Thus, a standard filter would cause a significant phase error. A zero-phase filter with the concept shown in Fig. 3.24 solves this problem. It is based on a bidirectional filtering technique [133]. The signal is digitally filtered with the proper filter type and reversed. This procedure is repeated one time and the phase change caused by the first filter is corrected by the second one. The magnitude of the overall transfer function equals the squared magnitude of the single filter's one.

Determination of phase and magnitude

Under the assumption that the MNP sample magnetization rotates with the same frequency as the rotating magnetic field (see section 2.1), the phase lag φ represents the phase shift between the components of the RMF and magnetization in the x- or y-direction (see Fig 3.25). Thus, the phase lag

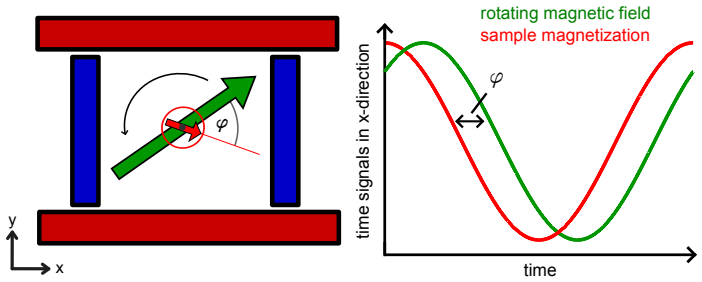

Figure 3.25: Illustration of the phase lag between the RMF and the sample magnetization vector. The time graph depicts the phase shift between the signals of the components in x direction.

can be found by comparing the coil current of the Helmholtz coil S1 and the output signal of the gradiometric fluxgate arrangement, which measures the magnetization component in the x-direction.
An adequate technique to determine the phase lag between the two time signals $x(t)$ and $y(t)$ is the calculation of the cross-spectral density S_{xy} based on the FFT of the two signals, also referred to as cross power spectrum. The principle formula is given by

$$S_{xy} = \frac{\mathrm{FFT}(x(t)) \cdot \mathrm{FFT}(y(t))}{n_\mathrm{s}^2} \tag{3.7}$$

with the common length of the signals n_s. This spectrum represents a complex quantity, which can be split into a magnitude and phase spectrum. Here, the value of the phase spectrum with the frequency of interest gives the phase lag between the signals. In the case of a noisy or by other frequencies disturbed magnetization signal, the phase lag can still be determined, if the reference signal, the coil current, is dominated by the frequency of interest. An optimized, automated determination is realized by additionally analyzing the magnitude spectrum and performing an interpolation. The mathematical concept of this approach is similar to the one of a digital lock-in amplifier.

Frequency response correction

The significant phase change and magnitude drop in the fluxgate frequency response necessitates a correction of the determined phase shifts between the fluxgate and coil current signals and the measured sample flux density magnitudes. Hence, the frequency response of the single fluxgates X and Z and the gradiometric output were recorded (see Fig. 3.10) in a frequency range from 1 Hz to 10 kHz with a step size of 10 Hz and saved in a look-up table. Here, the amplitude response is normalized to its DC value. The fluxgate measurement of the MNP sample magnetization in a RMF with different frequencies can be described by a multiplication of the sensor's complex transfer function and the magnetization dynamics in the frequency-domain. Thus, the correction of the phase and the magnitude is realized by a subtraction and a division, respectively. A correction of the measurement results for all frequencies is based on a linear interpolation between the phase and magnitude values of the recorded frequency response. The formula for this calculation is given by

$$y_{\mathrm{corr}}(f) = y_i + f\frac{y_{i+1} - y_i}{f_{i+1} - f_i} \tag{3.8}$$

with

$$f_i < f < f_{i+1}. \tag{3.9}$$

Here, y_{corr} represents the phase or magnitude value for the correction as a function of the frequency f. The corresponding values from the look-up table are identified by the index i. The maximum error of this correction procedure without the linear interpolation amounts for the phase and magnitude to 0.4° and 0.2 %, respectively. Due to the 10 Hz steps of the recorded frequency response, the linear interpolation reduces the errors at least by a factor of 10.

3.4 Performance

In this section, the performance of the measurement system is characterized. This includes a characterization of the system's accuracy (systematic error) of the phase lag determination by performing measurements on different

calibration samples. In a next step the phase lag accuracy with respect to the minimal measurable magnetic flux density (particle concentration) based on random or at least non-correctable errors is discussed. Finally, an estimation of the system's extended measurement uncertainty for a set of defined parameters is presented.

3.4.1 Systematic error

The calibration of the measurement system can be performed with a reference sample whose magnetization dynamics is known for the given frequency range. Thus, paramagnetic materials can be applied which possess a zero phase and constant magnitude at audio frequencies. One appropriate paramagnetic material is dysprosium oxide (Dy_2O_3) which exhibits a comparably high susceptibility and was investigated as a calibration sample for AC susceptometers [134]. Furthermore, small copper cylinders can be utilized for the calibration. Their response to dynamic magnetic fields is based on eddy-current effects and can be simulated for the given cylinder geometry and magnetic field. This was presented for AC susceptibility measurements [135]. In addition, a MNP sample can be applied, whose characteristic frequency is significantly higher than the systems frequency range. This ensures a nearly zero phase and a constant magnitude.
In this section, calibration measurements with two dysprosium oxide samples and one single-core iron oxide nanoparticle sample are presented. All samples are prepared in glass vials and possess a volume of 150 µL. The dysprosium oxide is filled as a powder into the vials, balanced and sealed with epoxy glue to prevent it from hydrating. The effective Dy_2O_3 densities are $2.4566\,\mathrm{g/cm^3}$ (Dy_2O_3-1) and $2.339\,\mathrm{g/cm^3}$ (Dy_2O_3-2). The MNP is an iron oxide single-core particle with a core diameter of 15 nm (SHP15). Thus, it is dominated by the Néel relaxation process and possesses a characteristic frequency larger than 1 MHz [136]. The iron concentration of the MNP sample amounts to 5 g/L. The parameters of the RMF calibration measurements with a magnitude of 1 mT are defined as following:

- frequency range: 22 Hz to 5 kHz
- measurement time per frequency: 500 ms
- number of repetitions: 5
- repetition pause: 90 s
- sample temperature: 24 °C

This set of standard parameters is reused for further measurements, if not otherwise stated. Fig. 3.26 depicts the performed calibration measurements of the phase lag and magnitude as a function of frequency. The magnitudes are normalized to the average value of each measured spectrum which is in the range of 300 nT and 600 nT for the dysprosium oxide and the iron oxide particle sample, respectively. In principle, all samples show the same behavior, only at higher frequencies small deviations are noticeable between the measured phase lags (<0.06°). In general, an average offset of 3° is observed which is caused by an imperfect alignment of the fluxgate sensors and sample holder along the axis of the small Helmholtz coil S1 (see Fig. 3.7). A slight shift of the sensors or sample holder in the y-direction can result in an additional phase lag between the measured sample magnetization and RMF since the field rotation is monitored indirectly via the coil current. The deviations of the phase lag from this offset value amount to maximal 0.1°. The magnitudes of all three samples show deviations of up to 1.5 % from the average value.
The system's measurement results were additionally compared with the results of a similar system whose sensor is based on a gradiometric air coil and the excitation on a compact 2-axis Helmholtz coil system with a reduced homogeneity [137]. The advantage of this system is the sensor's simplicity and insensitivity to the exciting magnetic field as well as an increased upper frequency limit. However, the lower limit is also increased due to Faraday's law of induction. As can be seen in Fig. 3.27, no systematic differences between the measurement results recorded with the two systems are observable. The maximum deviation of the phase lags is 0.5° and of the magnitudes 2 %. This supports the small errors found in the calibration measurements with the reference samples.
Fig. 3.28 illustrates further RMF measurements on the calibration sample Dy_2O_3-2 with increased field magnitudes of up to 9 mT and the set of standard parameters. In this case, the phase lags are offset corrected and the

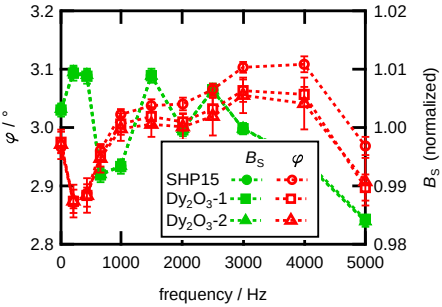

Figure 3.26: Measurement of phase lag φ and magnitude B_S as a function of frequency of iron oxide single-core particle (SHP15) with 15 nm core diameter and dysprosium oxide (Dy2O3) samples in RMF with 1 mT magnitude. The magnitudes are normalized to the average value of each measured spectrum. The error bars represent the standard deviation of five measurements.

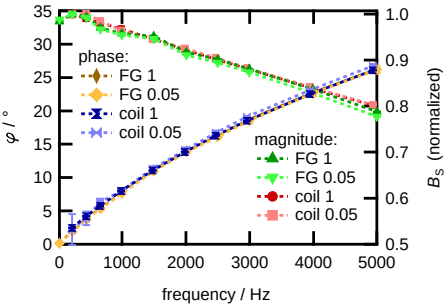

Figure 3.27: Comparison of fluxgate (FG) and measurement coil detection. An iron oxide single-core particle (SHP30) with 30 nm core diameter in a 1 mT RMF is investigated. The magnitudes are normalized to the value at 222 Hz. The two samples possess iron concentrations of 1 g/L and 0.05 g/L. The error bars represent the standard deviation of five measurements.

magnitudes are normalized to the magnitude at 22 Hz. One can see that up to 3 mT no significant changes of the phase lag and magnitude spectra occur compared to Fig. 3.26. However, a further increase of the field strengths results in noticeable changes. The phase lags display a maximum at around 3 kHz which grows up to 2° for 9 mT and the magnitude drops continuously with frequency, e.g. for 9 mT and 5 kHz the magnitude is reduced by 8 % compared to 22 Hz. These measurements are supported by repetitions with the 15 nm iron oxide nanoparticle sample, which show the same effect on the phase lag and magnitude. Thus, sample related effects which may cause the observed changes can be excluded. In fact, thermal effects and/or influences on the core magnetization in the fluxgate sensors induced by the comparably high RMF strength display reasonable explanations. In general, sample measurements in a RMF with a magnitude of more than 3 mT need to be corrected with the corresponding calibration measurements. This can be performed analogously to the fluxgate frequency response correction explained in section 3.3.2.

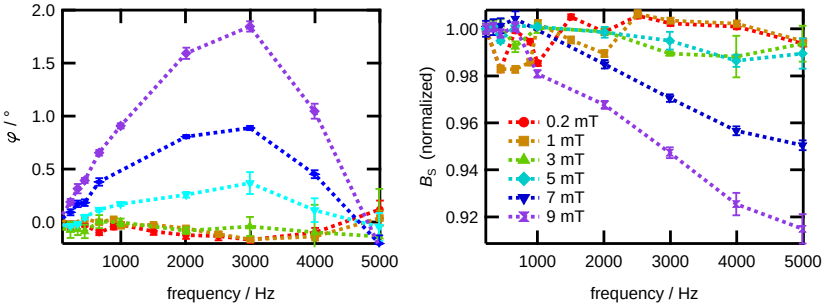

(i) (ii)

Figure 3.28: Measurement of (i) phase lag and (ii) magnitude as a function of frequency of dysprosium oxide sample in RMF with increasing magnitude. The phase lag is offset corrected and the magnitude normalized. The error bars represent the standard deviation of five measurements.

3.4.2 Random error

The limitation of the measurement system regarding the minimal detectable and correctly analyzable particle concentration is mainly caused by the residual field component of the exciting magnetic field in the measurement system's output signal. The phase φ_R and magnitude B_R induced by this disturbance are not long-term stable and consequently cause random errors. The noise performance of the system (sensor, data acquisition), which additionally affects the system's random error, would result in a noticeable lower limit. In the following, the influence of φ_R and B_R as a component of the measured signal, which is in this section expressed by the phase φ_M and magnitude B_M, on the phase lag φ and magnitude B_S of a MNP sample in a RMF is examined.

The exciting magnetic field component in the output signal is clearly reduced by the perpendicular sensor alignment and the gradiometric measurements at the two different z-positions. The residual component can be quantified by performing measurements without a sample. In this case, φ_M and B_M equal φ_R and B_R, respectively. Fig. 3.29 illustrates such measurements in a 0.2 mT, 1 mT and 5 mT RMF. The 5 mT results are additionally split up into the ones with and without activated series capacities. The field dependence of the residual component's magnitude can be clearly seen. Whereas for the

0.2 mT RMF, magnitudes in the range of 0.1 nT to 0.15 nT are present, for the 1 mT RMF the magnitudes are increased by a factor of five, which accords with the ratio of the excitation field strengths. For the 5 mT RMF the residual component's magnitudes are again enlarged by the corresponding ratio of the excitation field strengths, however, an influence of the sample temperature control and the sample positioning unit can be observed. A deactivation of these units results in a reduced residual component. The measurements with a 5 mT magnitude and frequencies above 1 kHz (activated series capacities) possess further increased magnitudes, which can be minimized by an extension of the pause between the measurement repetitions to 180 s. This effect can be explained by thermal drifts of the fluxgate sensors induced by high field magnitudes and frequencies. The field dependence of the residual RMF component is nearly compensated when a measurement on a MNP sample is performed whose magnetization follows - for the given field strength - the linear regime of the Langevin function. In this case, the relation of B_R to B_s remains constant.
In order to estimate the influence of the residual RMF component on the accuracy of the measurement results, the difference between φ_M and φ and the relation of B_M to B_S are calculated as a function of $\varphi - \varphi_\mathrm{R}$ varying from 0° to 360° and $B_\mathrm{R}/B_\mathrm{S}$ ranging from 0 to 0.1 (see Fig. 3.30). The corresponding formulas are given in appendix A.1. In the case of $B_\mathrm{R}/B_\mathrm{S} = 0.1$ and phase differences $\varphi - \varphi_\mathrm{R}$ of 90° or 270°, phase errors of up to 5° occur. Thus, for the RMF measurements the condition $B_\mathrm{R}/B_\mathrm{S} < 0.01$ should be met. With this condition the resulting phase and magnitude errors are smaller than 0.5° and 0.5 %, respectively, for all values of $\varphi - \varphi_\mathrm{R}$.
RMF measurements on two MNP concentration series support the found limitation of the measurement system. Each concentration series consists of several samples with one MNP type and a decreasing iron concentration. The SHP30 particles possess single iron oxide cores with a diameter of 30 nm. The BNF80 MNP represents an iron oxide multi-core particle with an approximately hydrodynamic diameter of 80 nm. The single iron concentrations as well as the amount of iron (Fe) per sample are listed in Table 3.4. The measured phase lags φ_M and magnitudes B_M as a function of frequency follow the discussed arc tangent and cosine dependence, respectively. Further information on the particle parameters and particle-specific measurement results can be found in chapter 4. The RMF magnitude amounts to 1 mT and the standard measurement parameters (see section 3.4.1) are applied.

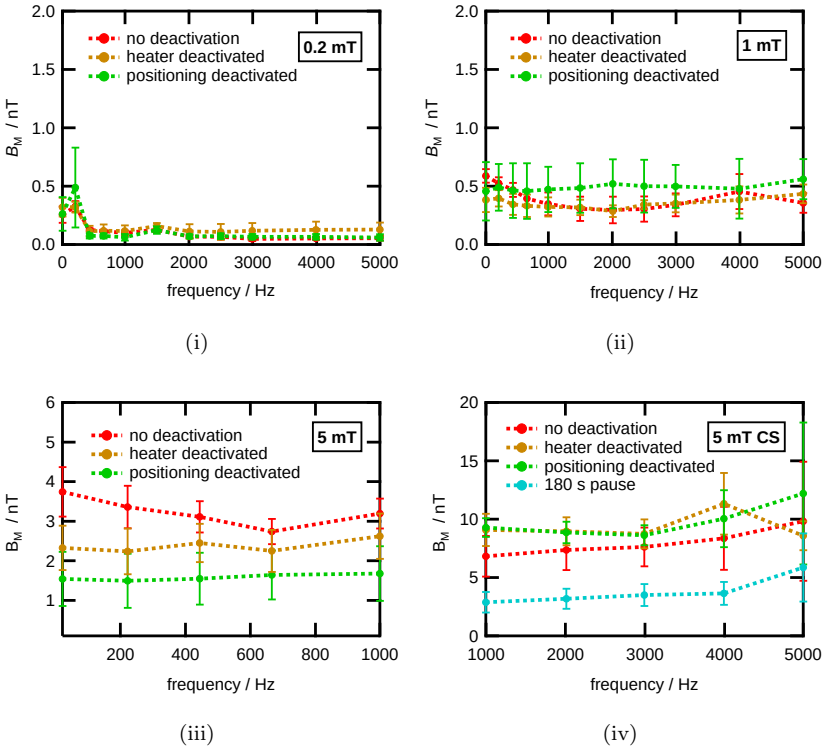

Figure 3.29: Measurement of residual RMF component: The magnetic flux density B_{M} is measured without any sample in the RMF system for different field magnitudes (i-iii). Each measurement is performed with a deactivated sample temperature control or positioning unit and without any deactivation. For the 5 mT RMF the results are split into the measurements with (iv) and without (iii) series capacities. The error bars represent the standard deviation of five measurements. Between each measurement repetition a pause of 90 s exist. The sample temperature is set to 24 °C.

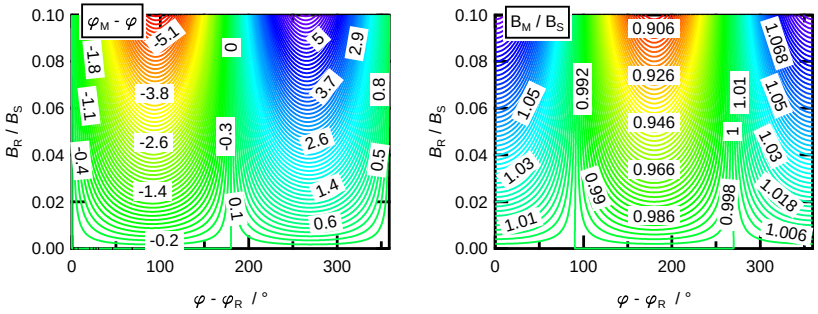

(i) (ii)

Figure 3.30: Calculation of (i) the deviation of the MNP sample phase φ from the measured phase φ_{M} and (ii) the relation of the measured stray field B_{M} to the sample stray field B_{S} caused by a residual RMF component with the phase φ_{R} and magnitude B_{R}.

Fig. 3.31 depicts for the BNF80 samples the measured phase lags and magnitudes. The latter is multiplied by the dilution factor DF for the graphical comparison of the different samples since the absolute values of B_{M} vary by several orders of magnitude. The starting sample with the highest iron concentration of 8 g/L possesses a DF of 1 (see Table 3.4). Noticeable deviations of the measured phase lag and magnitude spectra from the average curve progression can be found for the BNF80 samples with iron concentrations of 0.013 g/L and 0.0053 g/L. This is a consequence of the clearly reduced magnetic flux densities of these samples. Especially for high frequencies, the magnetic flux densities drop below 1 nT and, thus, the measurement results are significantly affected by the residual RMF component taking into account the calculations shown in Fig. 3.30. In the case of the single-core particle samples (SHP30, Fig. 3.32) lower iron concentrations can be measured without observing significant deviations, especially for the phase lag. Only the sample with an iron concentration of 0.001 67 g/L results in deviations of more than 5° from the average curve progression. The corresponding magnitude is the only one of the SHP30 samples that drops below 1 nT. The difference between the two particle systems is mainly attributed to the core structure and the hydrodynamic size: The multi-core particles possess a reduced magnetic moment in relation to the material's saturation magnetization (see section 1.1.2). The comparably large hydrodynamic size

results in a clear drop of the magnitude in the observed frequency range. Thus, lower B_M values are measured for BNF80 although the iron concentration is the same.
Table 3.4 additionally presents the measured phase lags and magnitudes of the SHP30 and BNF80 samples for a RMF frequency of 1 kHz. The mean values and standard deviations are based on ten measurement repetitions. The deviation of the mean values of the samples with the lower iron concentrations from the ones with higher iron concentrations reflects the impact of the residual field component. A correction of this effect is hard to realize since the magnitude and especially the phase of the residual RMF component possess no long-term stability. In contrast, the standard deviation represents the random errors caused by the measurement hardware, e.g. the analog-to-digital converter, the magnetic field sensor and the mechanics, as well as environmental effects, e.g. the temperature or electromagnetic disturbances. The sample preparation and manual positioning of the sample in the system is not included because for each measurement repetition the same sample is automatically positioned. A detailed description of the influence of the sample preparation on the measurement uncertainty of a fluxgate based MRX system is given by Heim [83]. These results are also valid for the RMF measurement system since an analog sensor arrangement and similar MNP samples are deployed. The standard deviations listed in Table 3.4 clearly indicate that the measurement uncertainty of the phase lag, which can be calculated based on the standard deviations [138], increases with decreasing magnetic flux density. The relative uncertainty of B_M increases as well, which is identified by the relation of the standard deviation to the mean value. Further measurement values of the concentration series samples for frequencies of 222 Hz and 5 kHz are presented in appendix A.2 supporting this discussion.
An exact specification of the RMF system's measurement uncertainty primarily of the determined phase lag and also of the magnitude is hard to realize. The so-called bottom-up approach based on the law of error propagation [138] requires a reliable equation describing the relation of the system's output quantity to all input parameters, including mechanical drifts and environmental disturbances. As shown by Heim for the fluxgate-based MRX system [83], this bottom-up approach does not satisfy the complexity of such an measurement process with multi-modal input parameters. In this context, the Research Training Group 1952/1 "Metrology for Complex Nanosystems" funded by the Deutsche Forschungsgemeinschaft is mentioned, which actually deals with the investigation of the uncertainty deter-

mination of complex nanosystems with multi-modal input parameters.
An uncertainty determination based on measurement repetitions (top-down approach) results only in an estimate of a general valid measurement uncertainty because the phase and magnitude as well as the non-correctable influence of the residual RMF component depend strongly on the investigated sample and affect each other. In order to specify at least a maximum measurement uncertainty for the phase lag determination the following conditions are defined:

- particle temperature T between 20 °C and 25 °C
- environment temperature T_{env} between 20 °C and 25 °C
- 1 mT RMF with set of standard parameters (no repetitions)
- relation $B_{\mathrm{R}}/B_{\mathrm{S}} < 0.01$

In this case, the combined measurement uncertainty u_{c} results in 0.375° based on following single standard uncertainties:

- calibration sample measurement (rectangular distribution): $u_{\mathrm{cal}} = 0.1^{\circ}/\sqrt{3} = 0.058^{\circ}$
- simulation of the maximal error caused by the residual RMF component for $B_{\mathrm{R}}/B_{\mathrm{S}} < 0.01$ (rectangular distribution): $u_{\mathrm{res}} = 0.5^{\circ}/\sqrt{3} = 0.289^{\circ}$
- estimated standard deviation for $B_{\mathrm{R}}/B_{\mathrm{S}} \approx 0.01$ based on the concentration series measurements (t-distribution, 95.45 %): $u_{\mathrm{cs}} = 0.2^{\circ}2.32/2 = 0.232^{\circ}$

Finally, the maximal expanded uncertainty u_{e} with a coverage factor of 2 based on a normal distribution with a probability of 95.45 % amounts to 0.75° with respect to the defined conditions.

Table 3.4: Dilution factor DF, iron concentration c(Fe) and iron amount per 150 µL sample volume of BNF80 and SHP30 concentrations series samples. The phase lag and magnitude are measured for each sample in a 1 mT RMF with a frequency of 1 kHz. The corresponding mean values and standard deviations are based on ten measurements.

particle	DF	c(Fe) / g/L	Fe/sample / nmol	$\varphi_{\mathrm{M,1\,kHz}}$ / °	$B_{\mathrm{M,1\,kHz}}$ / nT
BNF80	1	8	1785.24	53.701 ± 0.044	1108.41 ± 0.17
BNF80	2.5	3.2	21486.12	53.876 ± 0.030	448.821 ± 0.16
BNF80	7.5	1.067	8594.45	53.933 ± 0.042	150.22 ± 0.07
BNF80	15	0.533	2864.82	54.050 ± 0.109	75.94 ± 0.12
BNF80	60	0.133	1432.41	55.006 ± 0.249	18.31 ± 0.06
BNF80	150	0.053	358.10	57.568 ± 0.883	7.13 ± 0.08
BNF80	600	0.013	143.24	66.442 ± 8.591	1.73 ± 0.13
BNF80	1500	0.0053	35.81	106.479 ± 17.314	0.77 ± 0.12
SHP30	1	5	13428.83	11.981 ± 0.006	3294.99 ± 0.57
SHP30	3	1.667	4476.28	11.931 ± 0.008	1070.38 ± 0.722
SHP30	7.5	0.667	1790.51	11.752 ± 0.011	432.66 ± 0.12
SHP30	15	0.333	895.26	11.770 ± 0.018	206.47 ± 0.20
SHP30	37.5	0.133	358.10	11.907 ± 0.056	82.56 ± 0.17
SHP30	100	0.05	134.288	11.845 ± 0.122	30.28 ± 0.08
SHP30	300	0.0167	44.763	11.835 ± 0.483	7.89 ± 0.09
SHP30	600	0.0083	22.381	11.878 ± 0.917	4.66 ± 0.06
SHP30	1500	0.0033	8.953	10.762 ± 1.388	1.79 ± 0.08
SHP30	3000	0.00167	4.476	15.183 ± 4.347	0.71 ± 0.07

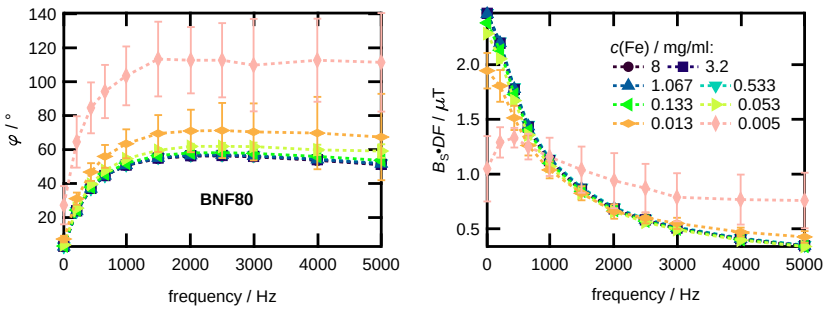

Figure 3.31: Measurement of phase lag (i) and magnitude (ii) as a function of frequency of iron oxide multi-core particle samples with decreasing iron concentrations in RMF with 1 mT magnitude. The phase lag φ_M is offset corrected and the magnitude B_M multiplied by the dilution factor DF. The approximate core diameter of the MNP (BNF80) amounts to 80 nm. The error bars represent the standard deviation of ten measurements.

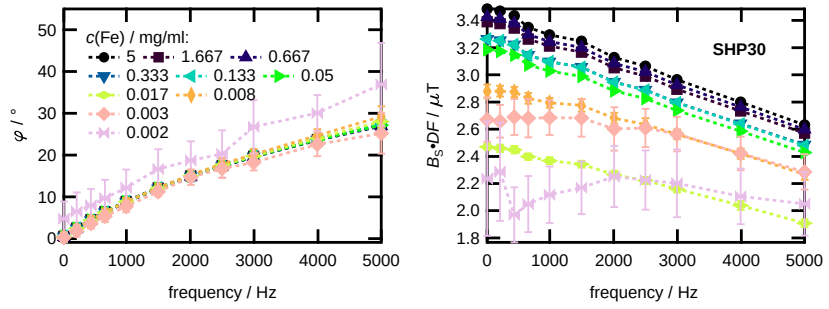

Figure 3.32: Measurement of phase lag (i) and magnitude (ii) as a function of frequency of iron oxide single-core particle samples with decreasing iron concentrations in RMF with 1 mT magnitude. The phase lag φ_M is offset corrected and the magnitude B_M multiplied by the dilution factor DF. The core diameter of the MNP (SHP30) amounts to 30 nm. The error bars represent the standard deviation of ten measurements.

4 Results and discussion

The dynamic response of magnetic nanoparticles to rotating magnetic fields depends on various parameters. This chapter will introduce different nanoparticle systems which differ in their core and hydrodynamic size as well as their material composition. The influence of their parameters on the dynamic response is explained with measurements of the phase lag and compared with simulations and supporting independent characterization techniques. Finally, an outlook is given on the utilization of these dynamics for the realization of homogeneous bioassay applications.

4.1 Nanoparticle systems

The main difference between the nanoparticle systems are their material composition and the core and hydrodynamic size in relation to the shape. Furthermore, two different core types depending on the synthesis are established: The single- and the multi-core. Here, measurements on different spherical and rod-shaped single- (SC) and multi-core (MC) nanoparticles are presented. Table 4.1 gives an overview about the applied particles and their producers.
The MNP type with the code **ALP** represents a single-core particle based on an iron oxide composition. The core diameter of the particles investigated in this work ranges from 12 nm to 25 nm. They are suspended in a non-polar solvent, e.g. chloroform, and possess an oleic acid shell of 2 nm to 4 nm thickness. The particles are provided by the Institut für Elektrische Messtechnik and Grundlagen der Elektrotechnik at Technische Universität Braunschweig (Braunschweig, Germany) and were subject to an elaborate development and investigation process, e.g. for further biomedical applications they were transfered to water via a PEGylation process and functionalized with antibodies [37].
A commercially available product is the particle type with the code **BNF**. It is manufactured by micromod Partikeltechnologie GmbH (Rostock, Germany) and distributed as a bionized nanoferrite particle with the product

name BNF-Starch. The particle core consists of several single iron oxide crystals (d_c : 10 nm to 20 nm) embedded in hydroxyethyl starch. Thus, BNF represents a polydisperse multi-core particle with average hydrodynamic diameters of 80 nm and 100 nm suspended in water [139]. For a TEM image of the 80 nm particle type see Fig. 4.1 (ii). Different functionalizations of the BNF particle are available, e.g. with streptavidin.
The particle type with the code **ENP** is an iron oxide MNP provided by the Department of Electrical Engineering of Kyushu University (Fukuoka, Japan). Its single crystals with an average core diameter of 30 nm and a polymer shell aggregated during the synthesis process forming clusters with a mean hydrodynamic diameter of more than 100 nm [140]. Thus, the particle can be treated as a multi-core system. The particles are suspended in water.
The MRI contrast agent FeraSpin™ R (**FSR**) manufactured by nanoPET Pharma GmbH (Berlin, Germany) represents another iron oxide multi-core particle with a broad size distribution. Its mean hydrodynamic diameter amounts to 60 nm, whereas the single crystallite diameter ranges from 5 nm to 8 nm. The particles are dissolved in an aqueous medium and were additionally functionalized with streptavidin.
A rod-shaped particle type (Fig. 4.1 (iii)) synthesized from nickel is identified with the code **NNR**. It was manufactured and provided by the division Experimentalphysik at Universität des Saarlandes (Saarbrücken, Germany). The approximate core length and diameter of the received batch are 271 nm and 19 nm, respectively. These so-called nanorods are stabilized by a polyvinylpyrrolidone (PVP) layer of several nanometer thickness which enables a single particle dispersion in an aqueous solution. This particle type was subject to investigations of its rotational dynamics with an optical measurement setup [95, 141].
The MNP type with the code **SHP** represents an iron oxide single-core particle from Ocean NanoTech (San Diego, CA, USA). It is distributed with core diameters ranging from 5 nm to 40 nm [142] and consequently different iron oxide phase compositions of the particle core due to the synthesis process. A polymer coating (4 nm to 5 nm layer) stabilizes the particle in different media, e.g. aqueous and buffer solutions. For a TEM image of the 30 nm core diameter particle see Fig. 4.1 (i). These MNPs are additionally available with different functionalizations, e.g. with streptavidin or protein G.
The particle suspensions with the codes BNF, ENP and NNR are clearly dominated by the Brownian relaxation process, thus called Brownian par-

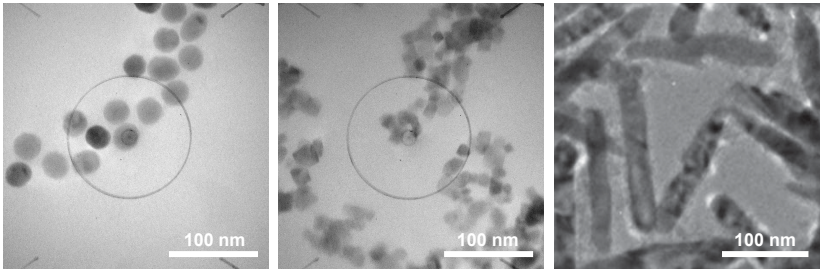

(i) (ii) (iii)

Figure 4.1: TEM images of different nanoparticle systems: Spherical single- (i) and multi-core (ii) as well as rod-shaped (iii) particles.

Table 4.1: Overview of investigated nanoparticle systems.

code	producer	shape	material	core
ALP	TU Braunschweig (Braunschweig, Germany)	spherical	iron oxide	SC
BNF	micromod (Rostock, Germany)	spherical	iron oxide	MC
ENP	Kyushu University (Fukuoka, Japan)	spherical	iron oxide	MC
FSR	nanoPET (Berlin, Germany)	spherical	iron oxide	MC
NNR	Universität des Saarlandes (Saarbrücken, Germany)	rod-shaped	nickel	SC
SHP	Ocean NanoTech (San Diego, CA, USA)	spherical	iron oxide	SC

ticles. In the case of the iron oxide single-core particle suspensions (ALP, SHP), only those particles with core diameters larger than 20 nm are clear Brownian particles. The FSR particle suspension shows a significant overlap of Brownian and Néel relaxation processes due to its broad particle size distribution. In the following sections the samples are identified via the introduced codes including the particle core diameter or length in nanometers determined from TEM images. For instance, SHP25 represents the corresponding iron oxide single-core particle from Ocean NanoTech with an mean core diameter of 25 nm. In contrast, for the multi-core particles the given value specifies the hydrodynamic diameter since an absolute core diameter of the whole particle is hard to define. The preparation of the samples with respect to the required sample volumes and concentrations is performed with Reference® pipettes from Eppendorf AG (Hamburg, Germany).

4.2 RMF measurement results

This section provides measurements of the phase lag and magnitude of the different particle systems. These RMF measurement results are compared with simulations and additional independent characterization techniques, e.g. ACS, PCS or magnetization curve measurements. After the clarification of the influence of the particle parameters on the phase lag and magnitude, the influence of the sample temperature and the Néel relaxation is examined. Finally a comparison with an alternating field excitation is presented. In all RMF measurements, the constant phase offset caused by the measurement system is corrected. If it is beneficial for the presentation or comparison, the magnitudes are normalized to their start values. The error bars in the RMF measurements represent the standard deviation based on five measurements. The dynamic viscosity of the water-based MNP suspensions accords with the viscosity of water for small particle volume fractions ($\phi < 0.01$) [143]. Thus, the viscosity for the RMF simulations is calculated based on the sample temperature. In general, the measurement results in the figures are represented by markers. Solid lines describe simulation results based on a corresponding model. Dashed lines are guides to the eyes. All RMF simulation results are based on the empirical model except the one of sample ENP100, which are the direct result of a numerical solution of the FPE. The distribution functions applied for the description of the particle polydispersity are log-normal ones if not otherwise stated, e.g. for the nanorod with its comparable large hydrodynamic size. The mentioned concentrations of the samples in the presented measurements are either the particle or the particle iron concentration with the unit g/L.

4.2.1 Particle parameters

The principle dependencies of the phase lag and magnitude of a MNP ensemble were discussed in section 2: The phase lag is described by an inverse tangent and the magnitude by a cosine curve progression as a function of the product of RMF angular frequency and modified Brownian time constant. With respect to the specific properties of the particles, unique progressions are observed for the different investigated samples. Although two particles possess the same mean magnetic moment and hydrodynamic size, different measurement results can be obtained, if, for instance, the size distributions differ. Thus, the measurement of the phase lag and magnitude of MNPs in a RMF provides significantly particle parameter-dependent results.

Particle system comparison

The phase lag and magnitude measurements of the different particle systems in a 1 mT RMF are presented in Fig. 4.2. The effect of the different hydrodynamic sizes is clearly discernible. The nanorod sample NNR271 possesses the quickest phase rise, followed by the multi-core particles BNF100 and ENP100. The samples SHP40, ALP25 and ALP12 with the single-core particles exhibit a clearly reduced increase of the phase lag. Especially, the phase lag of ALP12 rises only up to 2°. However, this is not a result of its small hydrodynamic size. ALP12 is dominated by the Néel relaxation due to its core diameter of only 12 nm. The phase lag of multi-core particle FSR60 shows interestingly only a small maximum phase lag and crosses the one of SHP40. The corresponding magnitudes are normalized to the magnitude measured at 22 Hz. They show an analog behavior compared to the phase lags. The particle with the smallest hydrodynamic size possesses the slightest drop of the magnitude.
The principle dependencies of the phase lag and magnitude are apparent by observing these measurement results and coincide with the theory. However, some observations need to be clarified in more detail: No measured phase lag reaches 90°. The phase lags of BNF100 and ENP100 cross each other and sample FSR60 exhibits for its hydrodynamic size a comparable weak phase lag rise and magnitude drop. These findings are a direct result of the hydrodynamic size distribution, which additionally affects the curve progression [116], and the presence of small fast Néel particles in the solution with a significantly higher characteristic frequency. In the case of the multi-core particle samples the amount of these superparamagnetic MNPs increases from sample ENP100 to BNF100 and finally FSR60. The corresponding k factors (see section 2.6) amount to 0.016 and 0.0375 for ENP100 and BNF100, respectively, for FSR60 it can not be determined due to the broad size distribution and the resulting overlap of the Brownian and the Néel particle contribution in the measured ACS. In contrast, the phase lag of NNR almost saturates at 90°. This sample is totally dominated by the Brownian relaxation process due to the pronounced shape anisotropy of the nanorods and the corresponding huge anisotropy energy barrier. The phase lag of the ALP25 sample is besides its hydrodynamic size additionally reduced by its carrier liquid. The viscosity of chloroform is approximately half the value of the viscosity of water.

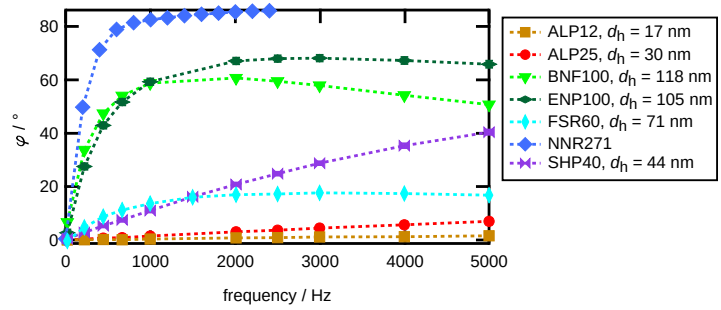

(i)

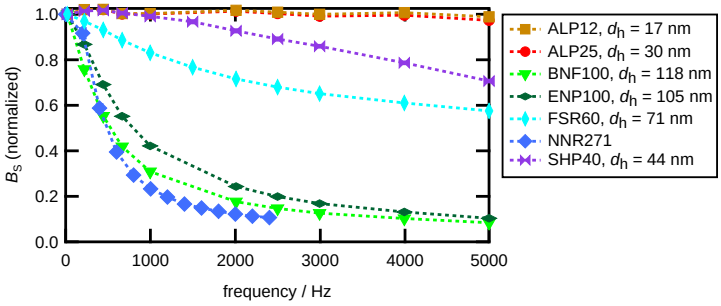

(ii)

Figure 4.2: Measured phase lags (i) and magnitudes (ii) as a function of frequency of MNPs with different shapes and hydrodynamic sizes in 1 mT RMF. The single magnitudes are normalized to the magnitude at 22 Hz. The approximately mean hydrodynamic diameters were determined for the spherical particles by DLS/PCCS measurements. The sample temperatures range between 294 K and 298 K. All samples are dissolved in an aqueous solution, except the ALP particles which are dissolved in chloroform.

Comparative simulations and measurements

In this section, the field-dependent RMF measurements of the ENP100, SHP25 and SHP40 sample are compared with simulation results based on particle parameters (magnetic moment, hydrodynamic size) which are determined with additional measurement techniques. In addition, the field-dependent RMF measurements of sample BNF80, BNF100 and NNR271 are presented and a fit with the RMF model is applied.
The average hydrodynamic diameter of the ENP100 particles was determined by DLS measurements and amounts 105 nm [140]. However, this measurement was not performed in a temporal proximity to the RMF measurements and it did not provide a reliable size distribution. Hence, the complex AC susceptibility of the sample was measured and analyzed with the corresponding model (section 1.2.4) incorporating a log-normal size distribution and taking into account the presence of the small Néel particles in solution [107]. Fig. 4.3 presents this measurement in comparison to the simulation results. The median hydrodynamic diameter $\tilde{d}_\mathrm{h}$ and the standard deviation σ_h amount to 120 nm and 0.26, respectively. The k factor was found to be 0.016. The saturation magnetization of 270 kA/m was determined with a vibrating sample magnetometer and a dried MNP powder sample. Describing the multi-core by a single sphere, a size distribution of the corresponding effective core diameter was estimated via the measurement of the sample's magnetization curve [107]. The determined distribution yields a median core diameter $\tilde{d}_\mathrm{c}$ and a corresponding standard deviation σ_c of 48 nm and 0.01, respectively. Thus, the mean magnetic moment of the ENP100 particle is around 15.6 aAm^2. With these parameters, the response to a RMF with magnitudes of 1 mT, 2.5 mT, 5 mT and 7.5 mT is simulated and compared with the measurements on the ENP100 sample. The simulation results are based on a numerical solution of the FPE [107]. As one can see in Fig. 4.4, a good match between the simulations and measurements is achieved. In addition, the influence of the field strength on the phase lag and magnitude is illustrated in the results. An increase of the field strength causes a reduced rise of the phase lag and drop of the magnitude. Thus, a spreading of the measured curve progressions with the field strength can be observed which is mainly affected by the particle magnetic moment.
The measured phase lags and magnitudes of the SHP25 and SHP40 sample in a 1 mT and 5 mT RMF are depicted in Fig. 4.5. In contrast to ENP100, the maximum phase lag is not reached in the observed frequency range, which is attributed to the smaller particle hydrodynamic size. Fur-

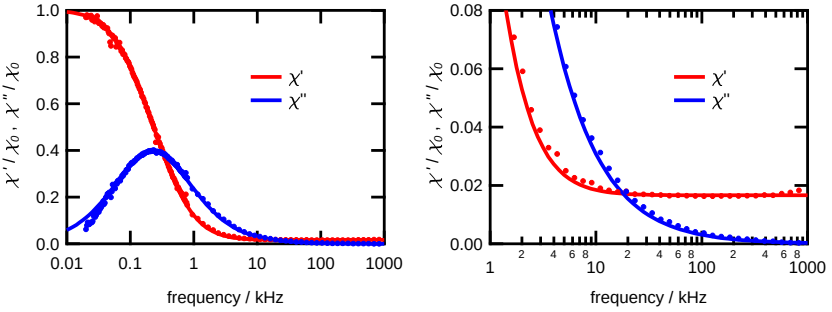

Figure 4.3: (i) Measurement of the complex AC susceptibility of ENP100 sample. The best fit between the measurements and simulation results was found for a log-normal hydrodynamic size distribution with $\tilde{d}_{\mathrm{h}}(\sigma_{\mathrm{h}}) = 120\,\mathrm{nm}(0.26)$. (ii) The k parameter amounts to 0.016 according with the ACS real part. The particle concentration is 3 g/L. [107] © 2012, AIP Publishing LLC.

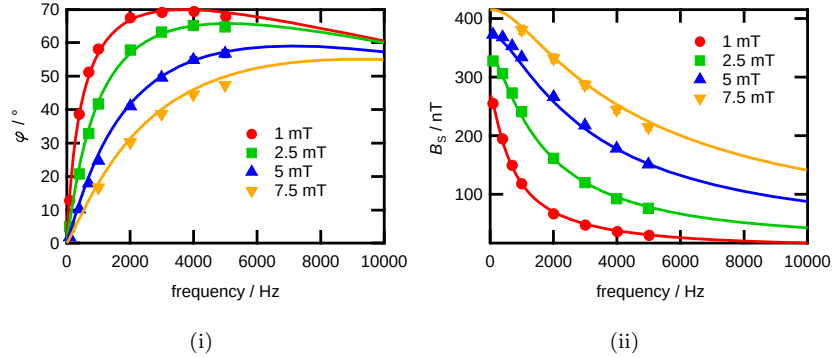

Figure 4.4: Comparison of measured and simulated phase lags (i) and magnitudes (ii) of ENP100 sample in a RMF with different magnitudes. The simulation parameters are based on the ACS and magnetization curve measurements including log-normal distributions: $\tilde{d}_{\mathrm{c}}(\sigma_{\mathrm{c}}) = 48\,\mathrm{nm}(0.01)$, $\tilde{d}_{\mathrm{h}}(\sigma_{\mathrm{h}}) = 120\,\mathrm{nm}(0.26)$, $M_s = 270\,\mathrm{kA/m}$, $T = 293\,\mathrm{K}$ and $k = 0.016$. The particle concentration is 3 g/L. [107] © 2012, AIP Publishing LLC.

thermore, the spreading with the RMF magnitude is less pronounced than for ENP100. Interestingly, for the single-core particle with the smaller core diameter, the spreading is stronger which implies a larger magnetic moment. This observation tallies with previous findings which demonstrated that reductive colloidal syntheses, e.g., iron-oleate decomposition, of iron oxide nanoparticles can lead to a deteriorated saturation magnetization with increasing particle core diameter [39]. In order to estimate the particle magnetic moment distribution of the two particle types, magnetization curves of both samples with an iron concentration of 0.42 g/L were reconstructed with the Langevin function applying SVD methodology [122]. The magnetic moment distributions resemble log-normal size distributions with a median magnetic moment $\tilde{m}_\mathrm{B}$ and a standard deviation σ_B. For SHP25 one finds $\tilde{m}_\mathrm{B}(\sigma_\mathrm{B}) = 1.6\,\mathrm{aAm^2}(0.7)$ and for SHP40 $\tilde{m}_\mathrm{B}(\sigma_\mathrm{B}) = 0.9\,\mathrm{aAm^2}(0.59)$ supporting the spreading of the measured RMF phase lags. A good fit between the RMF measurements and simulations based on the determined magnetic moments is achieved with hydrodynamic diameter distributions with the parameters $\tilde{d}_\mathrm{h}(\sigma_\mathrm{h}) = 35.6\,\mathrm{nm}(0.38)$ for SHP25 and $\tilde{d}_\mathrm{h}(\sigma_\mathrm{h}) = 44.5\,\mathrm{nm}(0.11)$ for SHP40. The k factor amounts to 0.13 (SHP25) and 0.06 (SHP40) corresponding to the drop of the ACS real parts in Fig. 4.6. These ACS measurements match additionally with simulation results based on the optimal hydrodynamic size distribution for the RMF simulations. Supplementary PCCS studies (see Fig. 4.7) yield for SHP25 and SHP40 log-normal size distributions with $\tilde{d}_\mathrm{h}(\sigma_\mathrm{h}) = 40.3\,\mathrm{nm}(0.12)$ and $\tilde{d}_\mathrm{h}(\sigma_\mathrm{h}) = 44\,\mathrm{nm}(0.13)$, respectively. Thus, the findings of the hydrodynamic sizes are supported by the optical PCCS measurements. The deviations of the hydrodynamic diameter of SHP25 is presumably the result of the necessary conversion of the intensity weighted correlation function into a number weighted particle size distribution and the related errors (see section 1.2.2). In summary, a significant match of the RMF measurements, simulations and additional characterization methods can be found for two different types of nanoparticles suspended in an aqueous solution. As a consequence the measured field-dependent response of MNPs in a RMF can be analyzed with the empirical model to estimate the magnetic moment and hydrodynamic size of an unknown MNP suspension.

Fig. 4.8 illustrates the measured phase lags of the BNF80, BNF100 and NNR271 samples for magnitudes of 1 mT to 5 mT. The most pronounced spreading is found for the nickel nanorods, which possess not the largest core volume but represent pure nickel single-core particles [144, 141]. The multicores of the BNF particles have in contrast a reduced iron oxide density and

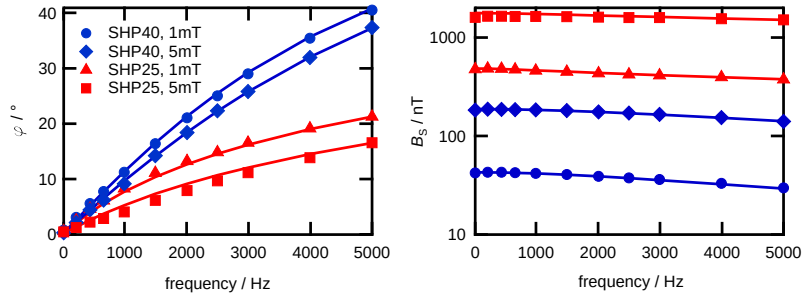

(i) (ii)

Figure 4.5: Measurement of phase lags (i) and magnitudes (ii) of SHP40 and SHP25 sample in 1 mT and 5 mT RMF. The best fit of the simulation results was found for SHP25 with $\tilde{m}_{\mathrm{B}}(\sigma_{\mathrm{B}}) = 1.6\,\mathrm{aAm}^2(0.45)$ and $\tilde{d}_{\mathrm{h}}(\sigma_{\mathrm{h}}) = 35.6\,\mathrm{nm}(0.38)$ and for SHP40 with $\tilde{m}_{\mathrm{B}}(\sigma_{\mathrm{B}}) = 0.9\,\mathrm{aAm}^2(0.38)$ and $\tilde{d}_{\mathrm{h}}(\sigma_{\mathrm{h}}) = 44.5\,\mathrm{nm}(0.11)$. The k parameters of 0.13 (SHP25) and 0.06 (SHP40) are based on ACS and the magnetic moment on magnetization curve measurements. The temperature amounts to 294.5 K and the particle iron concentration of both samples to 1.25 g/L. [122] © 2014, AIP Publishing LLC.

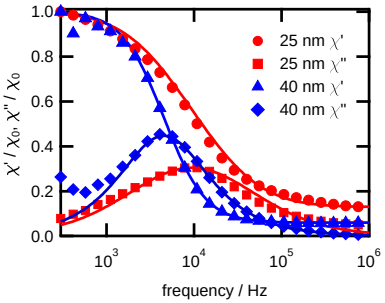

Figure 4.6: Measured ACS of sample SHP25 and SHP40. A simulation of the ACS with the parameters from the RMF simulation yields a good match with the measurements. The iron concentration of both samples amounts to 5 g/L. [122] ©2014, AIP Publishing LLC.

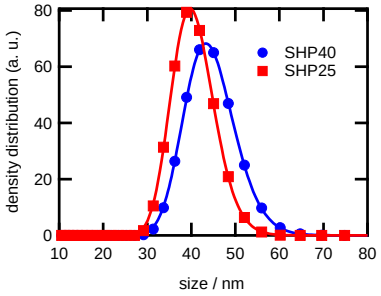

Figure 4.7: PCCS measurements of sample SHP25 and SHP40 yield log normal size distributions of hydrodynamic diameters with $\tilde{d}_{\mathrm{h}}(\sigma_{\mathrm{h}}) = 40.3\,\mathrm{nm}(0.12)$ and $\tilde{d}_{\mathrm{h}}(\sigma_{\mathrm{h}}) = 44\,\mathrm{nm}(0.13)$, respectively. The particle iron concentration of both samples is 0.15 g/L.

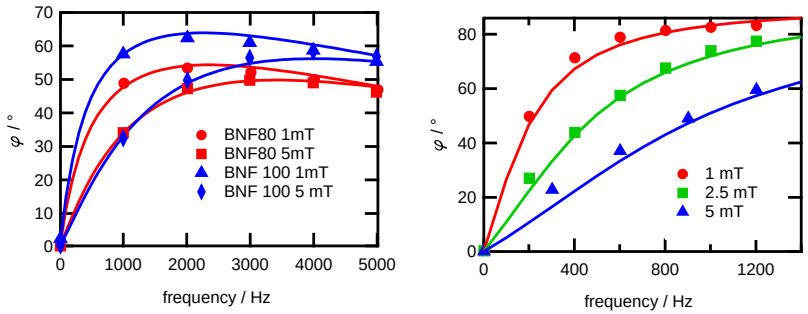

Figure 4.8: Measured phase lag of sample (i) BNF80 and BNF100 as well as (ii) NNR271 in 1 mT to 5 mT RMFs in comparison with simulation results. The corresponding parameters are listed in Table 4.2. The iron concentrations of the BNF80 and BNF100 sample amount to 13.7 g/L and 15 g/L, respectively.

consequently a deteriorated saturation magnetization. Thus, the magnetic moments $\tilde{m}_{\mathrm{B}}$ of 4.2 aAm^2, 8.8 aAm^2 and 40 aAm^2 from the RMF simulations of sample BNF80, BNF100 and NNR271, respectively, display reasonable parameters. The magnetic moment of sample NNR271 matches with magnetization curve measurements on similar nickel nanorods synthesized by the same current-pulsed electrodeposition process [44, 95]. A summary of all RMF simulation parameters is presented in Table 4.2. The k factors were determined from the real parts of the corresponding ACS measurements. The hydrodynamic sizes of BNF80 and BNF100 were additionally investigated with PCCS, which yields hydrodynamic diameters of 98 nm (BNF80) and 118 nm (BNF100) and match with the found RMF parameters. The exact hydrodynamic size determination of rod-shaped particles with photon correlation spectroscopy based methods displays a challenging task due to the indirect measurement approach via the particle diffusion coefficient [145]. Thus, this analysis was not performed for sample NNR271.

4.2.2 Temperature

The sample temperature, which can be controlled via the sample holder (see section 3.2.5), influences the dynamic response of the suspended MNPs to rotating magnetic fields via different relations: Firstly, the Langevin pa-

Table 4.2: Summary of RMF simulation parameters. The magnetic moments and hydrodynamic sizes are described by log-normal distribution functions except sample NNR271 which is described by a normal one.

sample	$\tilde{m}_{\mathrm{B}}(\sigma_{\mathrm{B}})$	$\tilde{d}_{\mathrm{h}}(\sigma_{\mathrm{h}})$	$\tilde{L}_{\mathrm{h}}(\sigma_{\mathrm{h}})$	k	T
BNF80	$4.2\,\mathrm{aAm^2}(0.17)$	$99.8\,\mathrm{nm}(0.21)$	-	0.075	298.5 K
BNF100	$8.8\,\mathrm{aAm^2}(0.14)$	$117.8\,\mathrm{nm}(0.2)$	-	0.0375	298.5 K
ENP100	$15.6\,\mathrm{aAm^2}(0.03)$	$120\,\mathrm{nm}(0.26)$	-	0.016	293 K
NNR271	$40\,\mathrm{aAm^2}(10\,\mathrm{aAm^2})$	$42\,\mathrm{nm}(13.5\,\mathrm{nm})$	$290\,\mathrm{nm}(61.3\,\mathrm{nm})$	0	298.5 K
SHP25	$1.6\,\mathrm{aAm^2}(0.45)$	$35.6\,\mathrm{nm}(0.38)$	-	0.13	294.5 K
SHP40	$0.9\,\mathrm{aAm^2}(0.38)$	$44.5\,\mathrm{nm}(0.11)$	-	0.06	294.5 K

rameter directly incorporates the temperature. For instance, an increasing temperature decreases $M(H,\omega)$ for a constant H and $\omega = 0$ in accordance with the Langevin function. In addition, the Brownian time constant is affected directly by the temperature and indirectly via the temperature dependence of the solution's viscosity. Thus, the frequency-dependent behavior of $M(H,\omega)$ is influenced by T. Fig. 4.9 displays the measured phase lag and magnitude of sample SHP25 in a 1 mT RMF for 303 K, 318 K and 333 K. One can clearly see the decrease of the magnitude with increasing T as well as the shallower phase lag rise and magnitude drop. The simulations with the RMF model show for 303 K still a good match with the measurements. However, with increasing temperature a discernible deviation is observed, especially for the phase lag measurements. This observation can be explained by the temperature-induced transition of Brownian to Néel particles which is not considered by the applied model. Fig. 4.10 (i) depicts a comparison of τ_{B} and τ_{N} as a function of T for an iron-oxide single-core particle with a core diameter d_{c} of 25 nm, a hydrodynamic diameter d_{h} of 35 nm and an effective anisotropy constant of $20\,\mathrm{kJ/m^3}$ suspended in water. In this case, the particle is dominated by the Brownian relaxation process over the whole temperature range from 270 K to 470 K due to its shorter time constant. The assumed K_{eff} of $20\,\mathrm{kJ/m^3}$ [146] represents a suitable value for spherical iron oxide single-core particles since they possess a non-perfect spherical shape, e.g. a prolate spheroid with an axial ratio larger than one. However, K_{eff} reduces significantly with decreasing axial ratio [147]. Thus, a comparison of τ_{B} and τ_{N} with a reduced K_{eff} of $5\,\mathrm{kJ/m^3}$ is shown in Fig. 4.10 (ii). In addition, the same calculation was performed for reduced d_{c} and

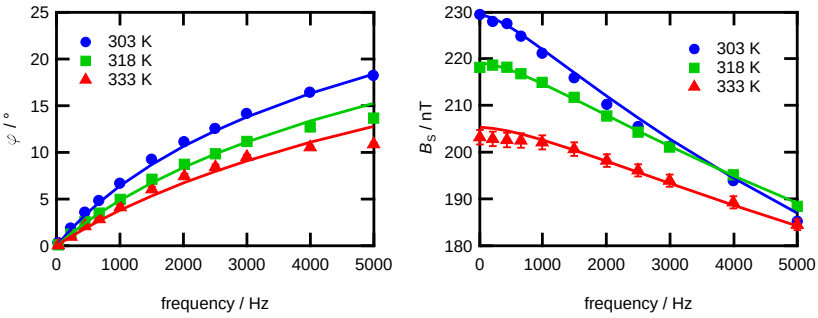

Figure 4.9: Temperature-dependent measurement of phase lag and magnitude of sample SHP25 in 1 mT RMF. The simulation parameters are listed in Table 4.2. The particle iron concentration amounts to 0.625 g/L.

d_h which can be found for such particles due to their size distribution and synthesis-dependent polydispersity (4.10 (iii)). These calculations give a reasonable explanation for the temperature-induced transition of Brownian to Néel particles.

4.2.3 Néel relaxation

The focus of this work lies on the investigation of the rotational dynamics of Brownian particles. These MNPs enable the realization of a homogeneous bioassay which is directly based on the particle dynamics. The dynamics of MNPs dominated by the Néel relaxation is not affected by target molecules which are independently bound to the particle surface. Only an induced clustering effect could have an impact on the dynamics due to interactions between the particles. Here, RMF measurements of two different ALP particles suspended in chloroform (mobile) and fixed in a matrix of gypsum (immobile) are presented (Fig. 4.11). These measurements illustrate the change of the MNP dynamics in a RMF when the Brownian rotation of the particle is totally hindered by an immobilization process and, thus, an internal rotation of the particle magnetic moment is induced by a RMF. For sample ALP12, only a slight difference is observable between the mobile and immobile measurement results. Apparently, the mobile ALP12 sample is also dominated by the Néel relaxation and only a small amount of parti-

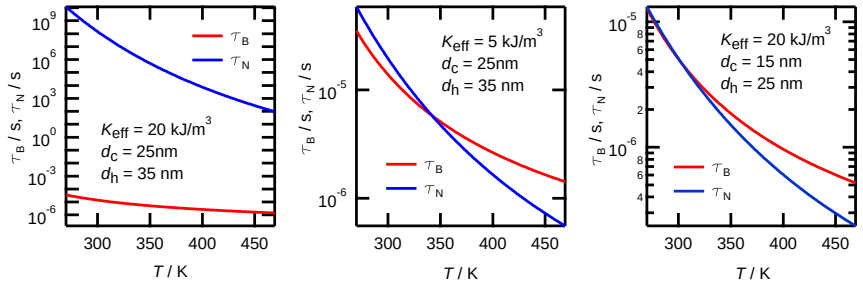

Figure 4.10: Comparison of τ_B and τ_N as a function of T for (i) common set of SHP25 parameters, (ii) reduced K_{eff} and (iii) reduced d_c and d_h.

cles in solution changes its dynamic response due to the immobilization. In contrast, significant changes occur for sample ALP25. The shallow linear phase lag rise transforms into a non-linear behavior with a stronger rise at low frequencies and a reduced rise at higher frequencies. The magnitude possesses a dramatic decrease at low frequencies which follows for higher frequencies the trend of the mobile sample's magnitude. These changes are caused by the significantly higher Néel time constant of particles which are dominated in the suspended state by the Brownian relaxation (see Fig. 4.10 (i)). The slight phase lag rise and magnitude drop of ALP25 for the higher frequencies is attributed to the amount of permanent Néel particles in solution. In the case of small Langevin parameters ($\xi \ll 1$) the dynamic response of Néel particles to rotating magnetic fields can be described by the Debye model for the AC susceptibility since it coincides with the RMF dynamics (see section 2). For larger Langevin parameters an additional analysis with the FPE or other approaches is required [119].

4.2.4 Rotating and alternating field

This section provides a comparison of measurements and simulations of the dynamic response of the ENP100 particles to alternating (ACF) and rotating magnetic fields for $\xi > 1$. The dynamic response is primarily described by the phase lag, which can be calculated for an ACF with the same formula as for a RMF (Eq. 2.27). The ENP100 sample is identical with the sample from Fig. 4.4.

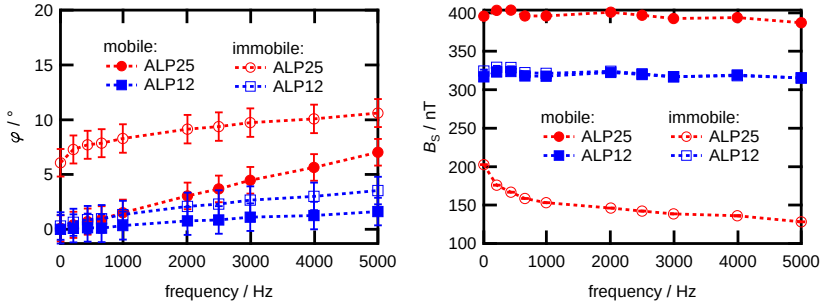

Figure 4.11: Measured phase lag and magnitude of mobile and immobile ALP12 and ALP25 sample in 1 mT RMF. The particle iron concentration amounts to 3.9 g/L.

"One general difference between the two magnetic field types is the dependence of the phase lag on the magnetic field magnitude, which is significantly larger for the rotating field mode (see Fig. 4.12 (ii)). This results in a higher spreading of the measured phase lags for different magnitudes in the rotating field. On the other hand, the measurement and simulation results for 1 mT indicate the mentioned analogy of RMF and ACF for small values of ξ since the particles show nearly the same dynamic behavior for both field types. In this case, the phase lag spectrum is solely determined by the distribution of the hydrodynamic sizes via the Brownian time constant. The observed magnitudes of the sample's magnetic flux density do not show noticeable differences for the peak value. In contrast, the time signals measured by the individual fluxgate sensors exhibit a different shape for the alternating and the rotating magnetic field type (see Fig. 4.12 (ii)). Whereas the signals in the alternating field show distinct deviations from a sinusoidal shape as a consequence of the nonlinearity of the magnetization curve [62], the rotating field components follow a sinusoidal dependence. One important difference between both field types is that the magnitude of the magnetic field vector aligning the MNPs remains constant for the rotating magnetic field, so that higher harmonics do not contribute to the signal [107].

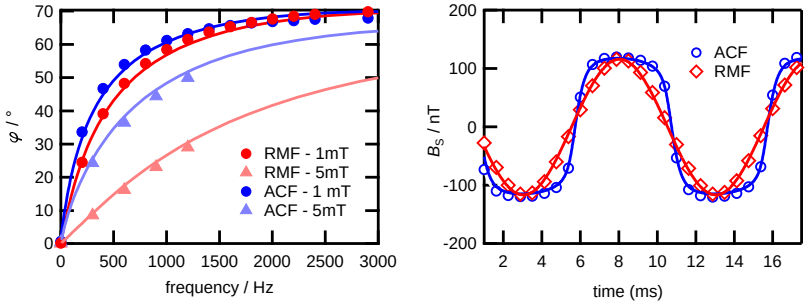

(i) (ii)

Figure 4.12: (i) Measurement results of phase lag of sample ENP100 in ACF and RMF with 1 mT and 5 mT magnitude in comparison with simulations based on parameters from Table 4.2. (ii) Measured time signal of B_S for $\omega/2\pi = 100$ Hz and $\mu_0 H = 5$ mT in ACF and RMF in comparison with normalized simulation results. [148] © 2012 IEEE.

Regarding the real and imaginary part of the sample's magnetic flux density, the change from an alternating to a rotating magnetic field is also visible. In Fig. 4.13 (i) the increase of the ACF magnitude from 1 mT to 5 mT causes a shift of the maximum in the imaginary part by about 750 Hz towards higher frequencies as well as a general increase of the real and imaginary part magnitude. For the RMF (see Fig. 4.13 (ii)) the shift is with about 2 kHz much higher than for the ACF. The measured susceptibility spectra can be well described by theory. The shift of the maximum of the imaginary part is caused by the field dependence of the Brownian time constant in the nonlinear regime [107]. Comparing the curve shapes of the real and imaginary part in the ACF and RMF with a 5 mT magnitude, a noticeable wider spreading (logarithmic scale) but lower magnitude is observed for the latter mode, indicating that MNPs can follow the rotating field to higher frequencies. These observations are valid for the different particle types. However, the effect strongly depends on the magnetic moment which is incorporated by the Langevin parameter." (Dieckhoff et al. [148] © 2012, IEEE) Thus, for the samples SHP25 and SHP40 only slight differences are observable between the ACF and RMF measurement results which were performed with the developed system.

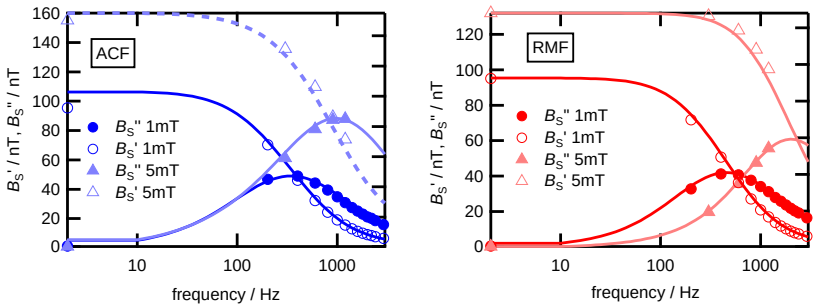

Figure 4.13: Measurement results of B'_S and B''_S of sample ENP100 in ACF (i) and RMF (ii) with 1 mT and 5 mT magnitude in comparison with simulations based on parameters from Table 4.2. [148] © 2012 IEEE.

4.3 Bioassay model system

This section provides measurements of MNPs functionalized with two different biological interaction systems. The one is based on the specific recognition and coupling of protein G to the Fc region of an immunoglobulin G (IgG), the other one is based on the specific interaction of streptavidin and biotin, which is known as one of the strongest non-covalent biological bindings. These systems are applied to investigate the general principle of a RMF based homogeneous bioassay, to compare a RMF with an ACF excitation, to demonstrate the possibilities of a quantitative target molecule detection and to analyze the influence of different particle systems. In addition, the influence of the binding reaction process on the bioassay results and the applicability of the RMF measurement for the determination of the corresponding parameters, e.g. the binding reaction's association constant, are presented. Finally, a first quantitative detection of the medical relevant biomarker HER2 with the RMF system is discussed.
The following MNPs are applied for these studies: The SHP particles functionalized with protein G (**SHP-G**) and streptavidin (**SHP-S**) are distributed by Ocean NanoTech (San Diego, CA, USA) with the product name IPG and SHS, respectively. The BNF particles with a streptavidin capped shell (**BNF-S**) are provided by micromod Partikeltechnologie GmbH (Rostock, Germany). The FSR particles functionalized with streptavidin (**FSR-**

S) are manufactured by nanoPET Pharma GmbH (Berlin, Germany). The target antibody for the protein G based experiments is the HRP goat anti-Human IgG Fc (**HRP-IgG**) with an average molecular weight of 270 kDa from ImmunoChemistry Technologies (Bloomington, MN, USA). As binding molecules for the streptavidin functionalized MNP experiments the biotinylated IgGs anti-human alpha-fetoprotein (**AFP-IgG**) and anti-human HER-2 (**HER2-IgG**) purchased from ebioscience (Frankfurt, Germany) are applied. They possess a molecular mass of approximately 150 kDa and are coated with biotin.
The constant phase offset caused by the RMF system is corrected for all figures. The error bars in the RMF measurements represent the standard deviation based on five measurements. The dynamic viscosity of the MNP suspensions is calculated based on the sample temperature. The measurement results in the figures are represented by markers. Solid lines describe simulation results based on the corresponding model. Dashed lines are guides to the eyes. All RMF simulation results are based on the empirical model except the simulations for the ENP100 and SHP35 particles. They are based on a numerical solution of the FPE. The distribution functions applied for the description of the particle polydispersity are log-normal ones. The mentioned concentrations of the samples in the presented measurements are the particle concentrations with the unit nM (nmol/L) since for the investigation of the binding effects the number of particles is important and not the iron or particle mass per sample.
The principle of the homogeneous bioassay based on the dynamics of MNPs in rotating magnetic fields was described in section 1.3.2. Fig. 4.14 (i) recalls this principle which facilitates the quantitative detection of target molecules bound to the particle surface via the measurement of the phase lag change $\Delta\varphi$. This change is the result of the subtraction of the phase lag before from the phase lag after the addition of the solution which contains the target molecules to quantify. In addition, Fig. 4.14 depicts the measurement of the phase lag as a function of time (i) and frequency (ii) for particle SHP-G40 binding to HRP-IgG antibodies in solution. The particle concentration amounts to 13 nM and the antibody concentration to 61.4 nM. The time-dependent measurement clarifies that the change of the phase lag after the addition of the target molecule solution requires some time to reach its final value. This measurement enables additionally the analysis of the binding kinetics. In the frequency-dependent measurement one can see that the phase lag change depends additionally on the exact frequency value. The analysis of the phase lag for the bioassay realization

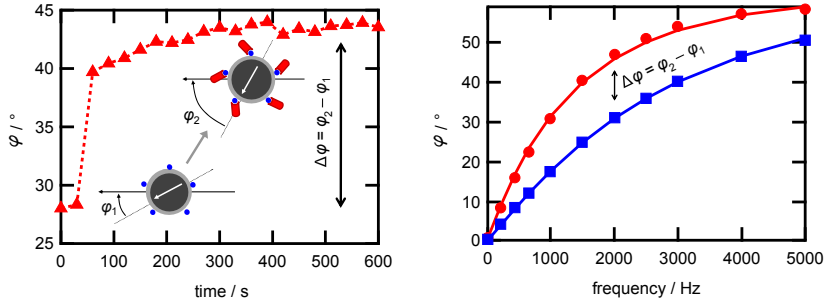

(i) (ii)

Figure 4.14: Measured phase lag as a function of time (i) and frequency (ii) for SHP-G40 particle. The phase lag changes due to bound antibodies (HRP-IgG). In the time measurement the antibody solution is injected after 30 s. The RMF frequency amounts to 2 kHz. The parameters of the frequency-dependent RMF simulations are $\tilde{m}_{\mathrm{B}}(\sigma_{\mathrm{B}}) = 0.9\,\mathrm{aAm^2}(0.38)$, $k = 0.06$ and $T = 294.5\,\mathrm{K}$. The hydrodynamic diameter is changing from $\tilde{d}_{\mathrm{h},1}(\sigma_{\mathrm{h},1}) = 52.2\,\mathrm{nm}(0.11)$ to $\tilde{d}_{\mathrm{h},2}(\sigma_{\mathrm{h},2}) = 66.8\,\mathrm{nm}(0.15)$. The particle and the IgG concentration amount to 13 nM and 61.4 nM, respectively.

is beneficial since it does not depend on the particle concentration, which can change due to the addition of the target molecule solution.

4.3.1 Excitation field dependence

The different responses of MNPs to alternating and rotating magnetic fields (see section 4.2.4) consequently results in differing physical effects ($\Delta\varphi$) of the phase lag based bioassay principle. Simulations carried out for two different particle systems clarify these differences:
"A highly sensitive homogeneous bioassay requires a strong effect of the binding molecules on the dynamic behavior of the particles. In our case, a high phase lag change is desirable, which is influenced by the change of the particle's hydrodynamic diameter. In order to model a binding assay where small biomolecules such as tumor-specific markers are detected, a 5 nm increase of the hydrodynamic diameter is assumed caused by an equally distributed specific binding of several biomolecules to the MNPs functionalized shell. In Fig. 4.15, the related phase lag change caused by the increase of the particle shell is shown for the parameters of the ENP100

sample under ideal conditions ($\sigma_B = 0$, $\sigma_h = 0$, $k = 0$) and various ACF and RMF magnitudes. Each curve has a maximum value at a specific frequency corresponding to a maximum sensitivity of the binding detection. Whereas the curves of the alternating and rotating magnetic field for 0.13 mT do not show a noticeable difference, for higher field amplitudes the curve maxima differ more and more in their height and frequency position. For 5.2 mT, the RMF exhibits a maximum phase lag change of 18° at 1.9 kHz, whereas for the ACF a maximum phase lag change of 9° at 0.9 kHz is obtained. In addition to the advantage of the measurement of the phase lag as a quantity which is ideally independent of the MNP concentrations, measurements in the RMF offer a higher sensitivity for the realization of bioassays. Due to the fact that smaller magnetic nanoparticles are more affected by the change of their hydrodynamic diameter, simulations of the phase lag change for the parameters of the SHP35 sample are depicted in Fig. 4.16 (caption displays particle parameters). The magnetic field dependence of the phase lag for these particles is relatively weak caused by their small magnetic moments. However, the particles possess under ideal conditions ($\sigma_B = 0$, $\sigma_h = 0$, $k = 0$) already for 5 mT a relatively large phase lag change, which has a maximum of about 20° and differs for the rotating and alternating magnetic field by more than 2°. By assuming a lognormal size distribution and a contribution of fast small Néel particles in the sample solution, the phase lag changes of the particles in both field types decrease, but still exhibits a well measurable value and a noticeable difference in their maxima. The frequency position of the maximum phase lag change, which is important for the realization of the bioassay, is almost not affected by the introduction of a size distribution." (Dieckhoff et al. [148] © 2012, IEEE)

These simulated findings are supported by measurements on SHP-G particles with core diameters of 25 nm, 30 nm and 40 nm interacting with antibodies (HRP-IgG) in solution. The protein-to-MNP ratio r represents the relation of the antibody to the MNP concentration.

"The phase lag changes $\Delta\varphi$ of the three MNP types caused by bound IgG with r values of 3.7 and 4.7 are calculated from the φ curvatures, which are measured in a RMF and ACF with 1 mT and 5 mT magnitudes (Fig. 4.17). These $\Delta\varphi$ curvatures possess a different width, maximum value $\Delta\varphi_{max}$ and frequency position depending on the particle type. The differences between the MNPs are mainly caused by the varying magnetic moments and hydrodynamic sizes. In addition, especially for the 25 nm particles, a small particle size can cause a transition from the Brownian to the Néel relaxation process due to the increased Brownian time constant after binding. A

detailed description of the influence of the various parameters is given by Dieckhoff et al. [122] (see section 4.3.2).
In a 1 mT RMF and ACF, the $\Delta\varphi$ curvatures of each particle size barely differ from each other. Here, the ξ parameters based on m_B determined by RMF fits with the empirical model are smaller or around one: $\xi_{25nm,1mT} = 0.4$, $\xi_{30nm,1mT} = 1.33$ and $\xi_{40nm,1mT} = 0.22$. Consequently, no significant difference between the RMF and ACF is expected. The small $\xi_{40nm,1mT}$ and therefore decreased saturation magnetization of single core MNPs with increasing core size coincides with previous findings [39]. By increasing the field amplitude to 5 mT, differences are observable between the RMF and ACF (Fig. 4.17 (ii)), at least for the 25 nm and 30 nm particles. This is also reflected by the corresponding ξ parameters: $\xi_{25nm,5mT} = 2$, $\xi_{30nm,5mT} = 6.65$ and $\xi_{40nm,5mT} = 1.1$. For the 25 nm MNP, $\Delta\varphi_{max}$ rises from ACF to RMF only by 0.5°, whereas the 30 nm MNPs exhibit a stronger rise of more than 1.5°. The exact value for the 30 nm MNPs cannot be determined with the RMF setup since the measurement range is limited to 5 kHz caused by the fluxgate bandwidth. Another observable effect in a RMF, that was predicted in [148], is the shift of $\Delta\varphi_{max}$ to higher frequencies compared to an ACF. The crossing of the ACF and RMF $\Delta\varphi$ curvatures for the same MNP type (Fig. 4.17 (ii)) represents a direct consequence of this shift. The frequently used air coils for the measurement of MNP dynamics significantly benefit from higher frequencies since their signal-to-noise ratio increases with frequency. Moreover, the growing width of $\Delta\varphi_{max}$ enables a wider range of RMF frequencies with a $\Delta\varphi$ close to $\Delta\varphi_{max}$. The apparent negative phase lag changes for the 30 nm particles at low frequencies (Fig. 4.17 (ii)) are caused by experimental errors." (Dieckhoff et al. [149])
Another question that was discussed in the same context is the further improvement of the bioassay's physical effect with increasing RMF magnitude and frequency:
"The arising question, how far the sensitivity can be improved by increasing H is answered by simulations of $\Delta\varphi$. These simulations are performed for the parameters of the 30 nm particle, which shows the best capability to further increase $\Delta\varphi$. Fig. 4.18 (i) depicts the contour plot of the simulated $\Delta\varphi$ as a function of the RMF frequency and magnitude. The highest sensitivity is found around 4 mT at 7.5 kHz and decreases with further increasing H. This effect is explained by the broad hydrodynamic size distribution of the functionalized MNPs. Assuming a MNP sample with the same set of parameters but a narrower hydrodynamic size distribution, $\sigma_{h,1} = \sigma_{h,2} = 0.15$, a

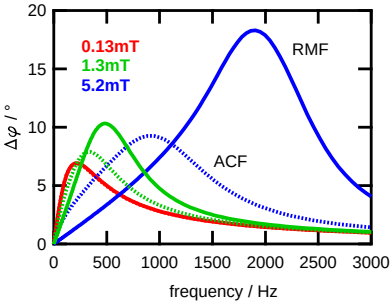

Figure 4.15: Simulated phase lag change due to homogeneous increase of particle shell by 5 nm for monodisperse MNP with $m_B = 15.6\,aAm^2$, $d_h = 120\,nm$, $k = 0$ and $T = 293\,K$ in ACF (dotted lines) and RMF (solid lines) with 0.13 mT, 1.3 mT and 5.2 mT magnitude. [148] © 2012 IEEE.

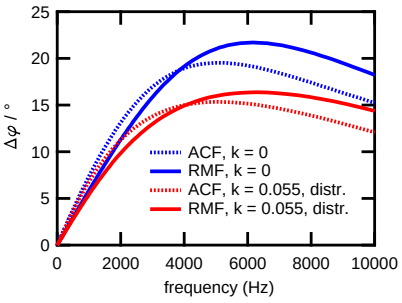

Figure 4.16: Simulated phase lag change due to homogeneous increase of particle shell by 5 nm for MNP with $\tilde{m}_B = 2.01\,aAm^2$, $\sigma_B = 0.15$, $\tilde{d}_h = 40.8\,nm$, $\sigma_h = 0.16$, $k = 0.055$ and $T = 293\,K$ in 5 mT ACF (dotted lines) and RMF (solid lines) with and without considering log-normal size distributions and contribution of fast Néel particles in solution. [148] © 2012 IEEE.

further increase of the sensitivity can be observed (4.18 (ii)). The phase lag change in general rises and the change of $\Delta\varphi_{max}$ with H becomes more pronounced. Here, the highest sensitivity is found around 7 mT at 12.25 kHz. Similar findings were simulated and measured with an optical detection system for nickel nanorods in rotating magnetic fields [95]." (Dieckhoff et al. [149] © 2014, AIP Publishing LLC)

4.3.2 Quantitative detection

The aim of the RMF bioassay principle is not only to detect the target molecules but also to quantify the amount in solution. Hence, measurements with the SHP-G25 and SHP-G40 particles and different concentrations of the HRP-IgG were performed. This section provides a summary of these results:

"In order to verify the quantitative detection of proteins with this detection approach, two IgG concentration series with the 40 nm and 25 nm protein G functionalized nanoparticles (Table 4.3 and Table 4.4) were measured with the RMF setup. Fig. 4.19 (i) and Fig. 4.20 (i) depict for each sample the

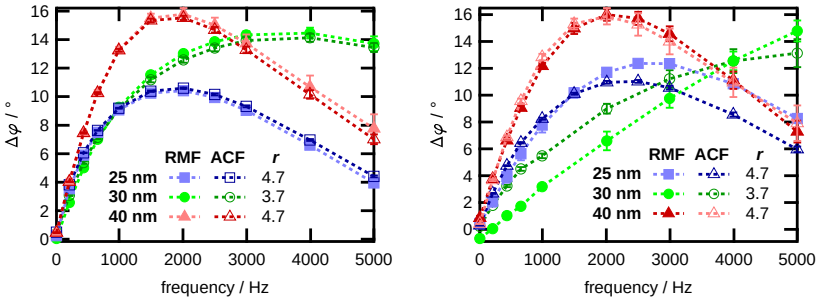

Figure 4.17: Measurement of $\Delta\varphi$ in 1 mT (i) and 5 mT (ii) ACF and RMF with SHP-G25, SHP-G30 and SHP-G40 and protein-to-MNP ratios r of 3.7 as well as 4.7. [149] © 2014, AIP Publishing LLC.

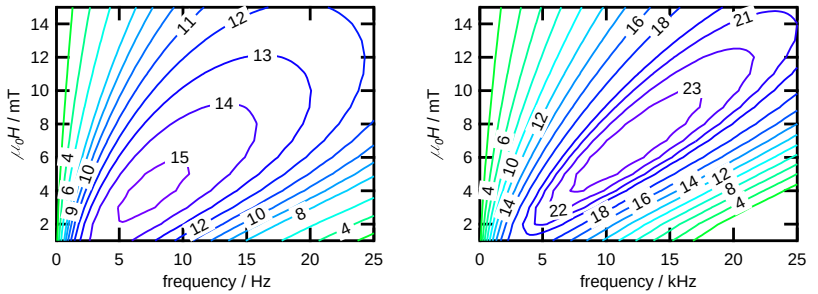

Figure 4.18: Contour plot of $\Delta\varphi$ (°) as a function of RMF frequency and magnitude based on simulations for SHP30 sample with protein G functionalization. (i) The particle parameters are based on RMF measurements: $\tilde{m}_{\mathrm{B}}(\sigma_{\mathrm{B}}) = 5.5\,\mathrm{aAm^2}(0.05)$, $k = 0.055$ and $T = 300\,\mathrm{K}$. The hydrodynamic diameter d_{h} increases from $\tilde{d}_{\mathrm{h},1}(\sigma_{\mathrm{h},1}) = 44.3\,\mathrm{nm}(0.3)$ to $\tilde{d}_{\mathrm{h},2}(\sigma_{\mathrm{h},2}) = 60\,\mathrm{nm}(0.29)$. (ii) Simulation with narrower hydrodynamic size distribution: $\tilde{d}_{\mathrm{h},1}(\sigma_{\mathrm{h},1}) = 44.3\,\mathrm{nm}(0.15)$ and $\tilde{d}_{\mathrm{h},2}(\sigma_{\mathrm{h},2}) = 60\,\mathrm{nm}(0.15)$. [149] © 2014, AIP Publishing LLC.

measured phase lag spectrum in a 1 mT rotating magnetic field. The shallowest rise can be seen for the bare particles without protein G because of their smaller hydrodynamic size. The functionalized particles exhibit a rise of the phase lag curvatures with increasing IgG concentration indicating the rising number of bound antibodies. Finally, this growth begins to saturate indicating the maximum possible protein binding to the particle surface. By comparing the 40 nm and 25 nm particles, one can observe that the 25 nm samples (Fig. 4.20 (i)) possess an overall shallower phase lag curvature, because their mean hydrodynamic size is smaller and the magnetic moment is bigger.

Fitting these phase lag measurement results with the theoretical model and the magnetic moment parameters from the particle characterization, a reasonable agreement is achieved for the 40 nm samples (Fig. 4.19 (i)) and at least up to 2.5 kHz for the 25 nm samples (Fig. 4.20 (i)). The deviations above 2.5 kHz for the 25 nm particle samples with a high IgG concentration can be caused by Brownian particles undergoing a transition to Néel particles which is not taken into account by the model. Here, the growing hydrodynamic size increases the Brownian time constant τ_B which can exceed τ_N. The 40 nm particles are less affected by this possible transition because their Néel time constant τ_N is several orders of magnitude higher due to the exponential dependence on the magnetic core volume. In general, the theoretical description of the magnetization's rotational dynamics for nanoparticles exhibiting an effective time constant τ_eff (influenced by Brownian and Néel relaxation) is still an ongoing research. The fitting parameters of the hydrodynamic sizes including a log-normal size distribution well represent the hydrodynamic growth. For the 40 nm samples the median hydrodynamic diameter $\tilde{d}_\mathrm{h}(\sigma_\mathrm{h})$ rises from 44.5 nm(0.11) to 76.5 nm(0.10). In contrast, the 25 nm samples exhibit a $\tilde{d}_\mathrm{h}(\sigma_\mathrm{h})$ increasing from 35.6 nm(0.38) to 63.0 nm(0.41). In Table 4.5 and Table 4.6 the hydrodynamic diameters of all samples are listed and compared with the hydrodynamic diameters determined by a PCCS analysis of the corresponding samples. The PCCS hydrodynamic size distribution is converted into a number-weighted one and fitted with a log-normal size distribution allowing a direct comparison of the PCCS and RMF results. The determined hydrodynamic median values of both methods show the same trend for the growth of the hydrodynamic diameter. They differ from each other in the range of some nanometers reflecting the measurement uncertainties. Only the 40 nm sample with the highest antibody concentration shows a significant deviation of about 10 nm. Regarding the width of the size distribution, the PCCS and RMF results

are in accordance for the 40 nm samples, the widths of the 25 nm samples obtained from the RMF measurements are significantly wider. Here, the deviation between the RMF measurement and simulation results above 2.5 kHz (Fig. 4.20 (i)) is one explanation. In addition, the necessary conversion of the intensity weighted correlation function into a number weighted particle size distribution [67] causes errors in the PCCS results regarding the determination of size distributions.
For the realization of a bioassay, the phase lag change $\Delta\varphi = \varphi_2 - \varphi_1$ is the measurement effect. Fig. 4.19 (ii) and Fig. 4.20 (ii) illustrate the spectra of this value based on the previously described phase lag measurement and simulation results. The reference sample for each series representing the initial phase lag φ_1 is the protein G particle with a protein concentration of 0 nM (G0). Each $\Delta\varphi$ curve possesses a maximum $\Delta\varphi_{\max}$ that reduces with decreasing IgG concentration. For the 40 nm particle samples, the maxima are located at 1.5 kHz and range up to 25°. In the case of the 25 nm particle samples, the maxima range only up to 12° and shift with a decreasing IgG concentration from 1.5 kHz to 5 kHz, whereas the frequency range of the $\Delta\varphi$ curves becomes much wider than for the 40 nm particle. This provides the possibility to perform binding experiments at a single frequency without a frequency sweep and nevertheless achieving a high measurement effect ($\Delta\varphi$). The observed phase lag changes even for target protein concentrations lower than the particle concentrations are well measureable except for G0.02 and G0.19 (both SHP-G40)." (Dieckhoff et al. [122])

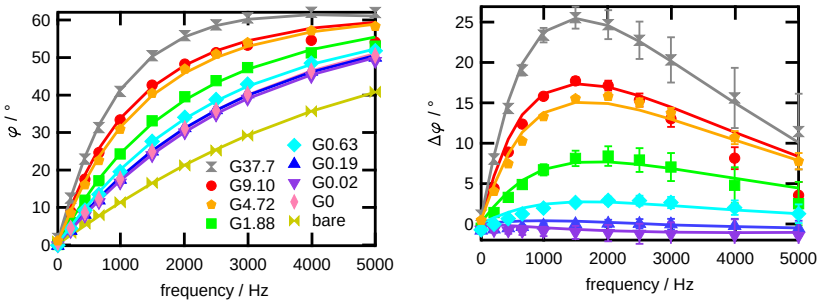

(i) (ii)

Figure 4.19: Measurement results of phase lag (i) and corresponding phase lag change (ii) for protein functionalized SHP40 with different IgG concentrations for a 1 mT RMF. Simulations are based on following parameters: $\tilde{m}_{\mathrm{B}} = 0.9\,\mathrm{aAm}^2$, $\sigma_{\mathrm{B}} = 0.38$, $k = 0.06$ and $T = 294.5\,\mathrm{K}$. The median hydrodynamic diameters and standard deviations are listed in Table 4.5. The legend displays the protein-to-MNP ratios. [122] © 2014, AIP Publishing LLC.

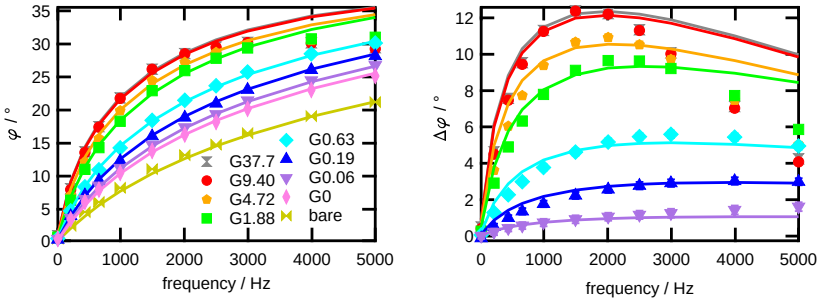

(i) (ii)

Figure 4.20: Measurement results of phase lag (i) and corresponding phase lag change (ii) for protein functionalized SHP25 with different IgG concentrations for a 1 mT RMF. Simulations are based on following parameters: $\tilde{m}_{\mathrm{B}} = 1.6\,\mathrm{aAm}^2$, $\sigma_{\mathrm{B}} = 0.45$, $k = 0.13$ and $T = 294.5\,\mathrm{K}$. The median hydrodynamic diameters and standard deviations are listed in Table 4.6. The legend displays the protein-to-MNP ratios. [122] © 2014, AIP Publishing LLC.

Table 4.3: Parameters of protein G functionalized 40 nm iron oxide particle samples with different protein-to-MNP ratios. [122] ©2014, AIP Publishing LLC.

40 nm	c(MNP)	c(IgG)	ratio	c(Fe)
G37.7	6.5 nM	247 nM	37.7	0.46 $\frac{\text{mg}}{\text{mL}}$
G9.1	13.5 nM	123 nM	9.10	0.96 $\frac{\text{mg}}{\text{mL}}$
G4.7	13 nM	61.4 nM	4.72	0.93 $\frac{\text{mg}}{\text{mL}}$
G1.88	13 nM	24.4 nM	1.88	0.93 $\frac{\text{mg}}{\text{mL}}$
G0.63	13 nM	8.2 nM	0.63	0.93 $\frac{\text{mg}}{\text{mL}}$
G0.19	13 nM	2.5 nM	0.19	0.93 $\frac{\text{mg}}{\text{mL}}$
G0.02	13 nM	0.26 nM	0.02	0.93 $\frac{\text{mg}}{\text{mL}}$
G0	17.5 nM	-	-	1.25 $\frac{\text{mg}}{\text{mL}}$

Table 4.4: Parameters of protein G functionalized 25 nm iron oxide particle samples with different protein-to-MNP ratios. [122] ©2014, AIP Publishing LLC.

25 nm	c(MNP)	c(IgG)	ratio	c(Fe)
G37.7	13 nM	494 nM	37.7	0.22 $\frac{\text{mg}}{\text{mL}}$
G9.4	13 nM	123 nM	9.40	0.22 $\frac{\text{mg}}{\text{mL}}$
G4.7	13 nM	61.4 nM	4.72	0.22 $\frac{\text{mg}}{\text{mL}}$
G1.88	13 nM	24.4 nM	1.88	0.22 $\frac{\text{mg}}{\text{mL}}$
G0.63	13 nM	8.2 nM	0.63	0.22 $\frac{\text{mg}}{\text{mL}}$
G0.19	13 nM	2.5 nM	0.19	0.22 $\frac{\text{mg}}{\text{mL}}$
G0.06	13 nM	0.81 nM	0.06	0.22 $\frac{\text{mg}}{\text{mL}}$
G0	73.9 nM	-	-	1.25 $\frac{\text{mg}}{\text{mL}}$

Table 4.5: Median hydrodynamic diameter and standard deviation $\tilde{d}_{\text{h}}(\sigma_{\text{h}})$ of IgG concentration series with 40 nm particle determined by RMF and PCCS measurements. [122] © 2014, AIP Publishing LLC.

40 nm	RMF	PCCS
G37.7	76.5 nm(0.10)	66.3 nm(0.14)
G9.4	69.5 nm(0.16)	63.4 nm(0.14)
G4.7	66.8 nm(0.15)	63.3 nm(0.12)
G1.88	59.3 nm(0.15)	53.7 nm(0.13)
G0.63	54.7 nm(0.14)	51.0 nm(0.11)
G0.19	52.5 nm(0.13)	47.5 nm(0.13)
G0.06	51.6 nm(0.12)	49.2 nm(0.12)
G0	52.2 nm(0.11)	47.3 nm(0.13)
bare	44.5 nm(0.11)	44.0 nm(0.13)

Table 4.6: Median hydrodynamic diameter and standard deviation $\tilde{d}_{\text{h}}(\sigma_{\text{h}})$ of IgG concentration series with 25 nm particle determined by RMF and PCCS measurements. [122] © 2014, AIP Publishing LLC.

25 nm	RMF	PCCS
G37.7	63 nm(0.41)	66.4 nm(0.13)
G9.4	62.5 nm(0.41)	63.2 nm(0.13)
G4.7	59.1 nm(0.41)	58.6 nm(0.13)
G1.88	55.6 nm(0.39)	55.0 nm(0.13)
G0.63	48.4 nm(0.39)	49.3 nm(0.13)
G0.19	44.0 nm(0.40)	47.2 nm(0.12)
G0.06	42.2 nm(0.38)	43.3 nm(0.13)
G0	40.8 nm(0.38)	45.2 nm(0.13)
bare	35.6 nm(0.38)	40.3 nm(0.12)

In addition, a discussion of these results based on a fit with a logistic function (see section 1.3.4) was presented:
"Fig. 4.21 depicts the phase lag change $\Delta\varphi_{2\,\mathrm{kHz}}$ measured at 2 kHz as a function of the target protein-to-MNP ratio r for the two MNP types. The data points are fitted with a logistic function given by

$$\Delta\varphi_{2\,\mathrm{kHz}} = \frac{\Delta\varphi_{\mathrm{low}} - \Delta\varphi_{\mathrm{high}}}{1 + \left(\frac{r}{r_{\mathrm{half}}}\right)^{\alpha}} + \Delta\varphi_{\mathrm{high}}. \tag{4.1}$$

The ratio r reflects the protein concentration since almost all measurements were performed at the same MNP concentration. The symbols $\Delta\varphi_{\mathrm{low}}$ and $\Delta\varphi_{\mathrm{high}}$ are the minimum and the maximum values of $\Delta\varphi_{2\,\mathrm{kHz}}$, respectively. For the fitting, $\Delta\varphi_{\mathrm{low}}$ is set to 0°. The r value at the half of the maximum phase lag change $\Delta\varphi = (\Delta\varphi_{\mathrm{high}} - \Delta\varphi_{\mathrm{low}})/2$ is represented by r_{half}. The fit results for both particles are displayed in Fig. 4.21 and the parameters are given in the figure caption. These fits demonstrate the calibration of the proposed bioassay, which enables the quantitative determination of the target protein concentration via the measurement of $\Delta\varphi$. With both particle types a quantitative detection of the investigated protein concentrations lower than the MNP concentrations is demonstrated. However, some differences between the two MNP types are visible.
By comparing the two logistic functions, one can see that the phase lag change $\Delta\varphi_{\mathrm{sat}} = \Delta\varphi_{\mathrm{low}} - \Delta\varphi_{\mathrm{high}}$ of the 25 nm particles is half the value of the 40 nm particles. This decreased phase lag change $\Delta\varphi_{\mathrm{sat}}$ is plausible due to the broader size distribution of the 25 nm particles and their more probable transition from a Brownian to a Néel relaxation dominated particle. The negative effect of a broader size distribution on the phase lag change was demonstrated by simulations [148]. In addition, Néel particles do not change their phase lag due to bound proteins, but still contribute to the measured B_{S} signal. So, the higher amount of nanocrystals (higher k factor) in the 25 nm particle suspension further decreases $\Delta\varphi_{\mathrm{sat}}$. Taking into account the half-logarithmic presentation of the logistic functions, the 40 nm particles possess also the broader measurement range with respect to r. The larger particle surface and consequently increased number of binding sites on the bigger particles still enable the binding of target proteins when the small particles are already fully covered by proteins. On the other hand, the logistic function of the 25 nm particles is shifted towards lower r values reflected by the five times smaller r_{half} parameter ($r_{\mathrm{half,40\,nm}} = 4.3$,

$r_{\mathrm{half,25\,nm}} = 0.8$). Considering the logarithmic representation of r in Fig. 4.21, the highest sensitivity is found in the logistic function of the 25 nm particles for r values around r_{half}. The smaller hydrodynamic volume, which in average grows stronger with an increasing r, explains the shift and the higher sensitivity. In this context, Fig. 4.22 presents the change of the hydrodynamic diameter Δd_{h} as a function of the phase lag change $\Delta\varphi_{2\,\mathrm{kHz}}$ for the two IgG concentration series. In a first approximation, Δd_{h} increases linearly with $\Delta\varphi_{2\,\mathrm{kHz}}$ and the 25 nm particle possesses the stronger increase. Consequently, the stronger growth of Δd_{h} with an increasing r for the 25 nm particle can be seen in Fig. 4.21.
In summary, Brownian nanoparticles with a time constant $\tau_{\mathrm{B}} \ll \tau_{\mathrm{N}}$ and a narrow hydrodynamic size distribution are favorable as a test system for the proposed bioassay. This can be achieved by single cores with high K_{eff} and high d_{c} resulting in an increased τ_{N}. However, high d_{c} also causes large d_{h}. Thereby, the sensitivity decreases and the lowest measureable r increases. In the case of the investigated single core iron oxide MNPs, the optimal d_{c} lies between the analyzed 25 nm and 40 nm. The particle magnetic moment has no direct influence on the measurement range regarding r, but affects the height of the measurement effect and the corresponding optimal RMF frequency [148]." (Dieckhoff et al. [122] © 2014, AIP Publishing LLC)
In addition to the published frequency-dependent measurement results [122] presented in the previous paragraph, real-time measurements of the phase lag during the injection of the antibody solutions were performed. Fig. 4.23 displays these measurements for the (i) SHP-G40 and (ii) SHP-G25 IgG concentration series in a RMF with a magnitude of 1 mT and frequency of 2 kHz. For both samples a rise of the phase lag after the injection of the IgG solution is observed. Thereby, the final value of the phase lag change increase with the IgG concentration. For SHP-G40 no significant difference between the samples G0, G0.02 and G0.19 exists which is in accordance with the frequency-dependent measurements. For SHP-G25 a saturation of the phase lag rise and maximum value can be seen for G37.7 and G9.40. The average time constant of the binding kinetics of these experiments is in the range of a few minutes. This enables a quick quantitative detection of the bound target molecules.

4.3.3 Binding reaction analysis

In the previous sections the influence of the magnetic field excitation and varying target molecule concentrations on the phase lag change was inves-

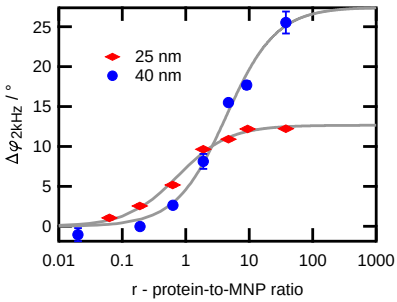

Figure 4.21: Measured phase lag change in a 2 kHz RMF with 1 mT magnitude as a function of the ratio r for the 25 nm and 40 nm particle IgG concentration series. Fit with logistic function with parameters: $\Delta\varphi_{\mathrm{low,40\,nm}} = 0°$, $\Delta\varphi_{\mathrm{high,40\,nm}} = 27.4°$, $r_{\mathrm{half,40\,nm}} = 4.3$, $\alpha_{40\,\mathrm{nm}} = 1.1$, $\Delta\varphi_{\mathrm{low,25\,nm}} = 0°$, $\Delta\varphi_{\mathrm{high,25\,nm}} = 12.7°$, $r_{\mathrm{half,25\,nm}} = 0.8$ and $\alpha_{25\,\mathrm{nm}} = 1.1$.[122] © 2014, AIP Publishing LLC.

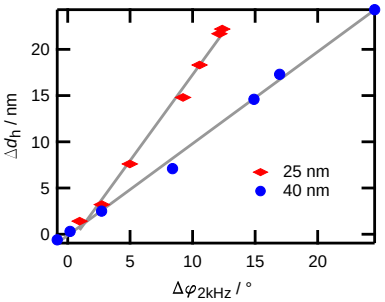

Figure 4.22: Hydrodynamic diameter growth as a function of the phase lag change in a 2 kHz RMF with 1 mT magnitude for the 25 nm and 40 nm particle IgG concentration series. The hydrodynamic growth and phase lag change are based on simulations from Fig. 4.20 and Fig. 4.19. The lines represent a linear regressions of the hydrodynamic growth as a function of the phase lag change. [122] © 2014, AIP Publishing LLC.

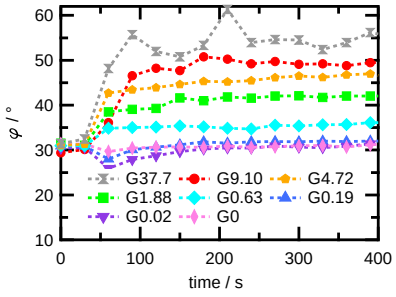

(i)

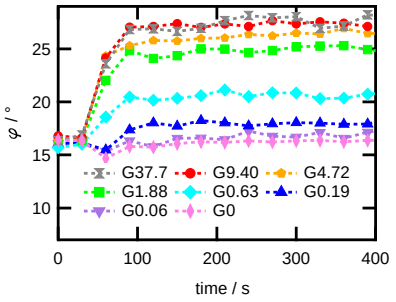

(ii)

Figure 4.23: Measured phase lag as a function of time for SHP-G40 (i) and SHP-G25 (ii) IgG concentration series (Table 4.3 and Table 4.4) in a RMF with a magnitude of 1 mT and frequency of 2 kHz. The antibody solutions are injected after 30 s.

tigated. In this section, the impact of the particle concentration on $\Delta\varphi$ is studied, which is directly influenced by the underlying binding reaction. Finally, this bioassay principle is applied to estimate the association constant K_a of the given binding reaction and the number of receptor proteins on the particle surface N_cov. Therefore, RMF measurements of SHP-G30 samples with different particle and increasing HRP-IgG concentrations published by Dieckhoff et al. [150] were performed.
The logistic function enables the calibration of a bioassay, which is presented in Fig. 4.21 for one particle concentration of each particle size. Here, three IgG concentration series with a 30 nm MNP (SHP-G30) and particle concentrations of 9.06 nM, 2.26 nM and 566 pM are discussed. Fig. 4.24 displays for these samples the peak values of the phase lag change $\Delta\varphi_\mathrm{peak}$ as a function of the initial IgG concentration $c_0(\mathrm{IgG})$. The quantity $\Delta\varphi_\mathrm{peak}$ represents the maximum value of each $\Delta\varphi$ curve and lies in the frequency range of 2.5 kHz to 5 kHz for the investigated 1 mT RMF. Each curve is fitted with a logistic function described by

$$\Delta\varphi_\mathrm{peak} = \Delta\varphi_\mathrm{high} - \frac{\Delta\varphi_\mathrm{high}}{1 + \left(\frac{c_0(\mathrm{IgG})}{c_{0,\mathrm{half}}(\mathrm{IgG})}\right)^{\alpha}} \tag{4.2}$$

with the initial antibody concentration $c_{0,\mathrm{half}}(\mathrm{IgG})$ which is required to cause a phase lag change of $\Delta\varphi_\mathrm{high}/2$. Thus, $c_{0,\mathrm{half}}(\mathrm{IgG})$ represents the case that approximately one eighth of the receptor proteins on the particle surface are bound to an IgG since the concentration $c(\mathrm{IgG_{bound}})$ is, as a first approximation, proportional to $(\Delta\varphi)^3$. The displayed logistic functions shift with a decreasing particle concentration to lower values of $c_0(\mathrm{IgG})$. However, this shift is non-linear, which is also reflected by the fit parameters for the three particle concentrations listed in Table 4.7. The concentration $c_{0,\mathrm{half}}(\mathrm{IgG})$ amounts to 15.20 nM for a $c(\mathrm{MNP})$ of 9.06 nM and reduces to 5.84 nM for a four times smaller $c(\mathrm{MNP})$ of 2.26 nM. However, an again four times smaller particle concentration of 566 pM results only in a reduction of $c_{0,\mathrm{half}}(\mathrm{IgG})$ to 4.66. This non-linear shift implies that for a reduced particle a higher target molecule concentration is required to achieve the same amount of bound target molecules per particle. This finding is explained by the law of mass action presented in section 1.3.3 because the particle and the corresponding receptor protein concentrations reach the range of the inverse association constant K_a of the applied binding reaction between protein G

and IgG [151]. The maximum value of the phase lag change $\Delta\varphi_{\mathrm{high}}$ of each IgG concentration series is affected by residual buffer components from the particle and antibody stock solutions since $\Delta\varphi_{\mathrm{high}}$ decreases with increasing particle concentration.
The law of mass action, as it is expressed by Eq. 1.45, facilitates a determination of the binding reaction's association constant by fitting it for known initial concentrations of the two reactants (here: protein G and IgG) to the measured product of the two reactants with K_{a} as a free fit parameter. For this investigation, the initial protein G concentration is replaced by the product of the particle concentration and the average number of protein G per particle N_{cov}

$$c_0(\mathrm{proteinG}) = c(\mathrm{MNP})N_{\mathrm{cov}}, \tag{4.3}$$

thus, N_{cov} displays a second free fit parameter. The concentration of the products, which is expressed by the concentration of bound IgG, is determined as follows: Based on the parameters of a fit of the empirical model to the RMF measurement results, the change of the hydrodynamic diameter Δd_{h} is calculated. The resulting change of the hydrodynamic volume ΔV_{h} is defined by

$$\Delta V_{\mathrm{h}} = \frac{\pi}{6}(\Delta d_{\mathrm{h}})^3 \tag{4.4}$$

and defines the amount of antibodies bound to the particle

$$N_{\mathrm{IgG,bound}} = \Delta V_{\mathrm{h}} \frac{\varrho_{\mathrm{P}}}{m_{\mathrm{P}}} \tag{4.5}$$

via the average protein density ϱ_{P} of $1.35\,\mathrm{g/cm^3}$ [152] and molecular mass m_{P} of 270 kDa for the HRP-IgG antibody. The resulting concentration of bound antibodies $c(\mathrm{IgG_{bound}})$ in each sample is finally calculated with the particle concentration

$$c(\mathrm{IgG_{bound}}) = c(\mathrm{MNP})\Delta V_{\mathrm{h}} \frac{\varrho_{\mathrm{P}}}{m_{\mathrm{P}}}. \tag{4.6}$$

The underlying assumption that the mass of a protein in solution is directly proportional to its hydrodynamic volume was proofed by Krouglova et al. [153] by performing diffusion coefficient measurements. In addition, Röcker et al. [154] successfully applied this relation to describe the hydrodynamic growth of nanoparticles caused by the adsorption of proteins to the particle surface in solution.
The results of the described conversion of $\Delta\varphi_{\mathrm{peak}}$ to $c(\mathrm{IgG_{bound}})$ for the three IgG concentration series are illustrated in Fig. 4.25. The curves are shifted to higher initial antibody concentrations due to the cubic dependence of $c(\mathrm{IgG_{bound}})$ on $\Delta\varphi$. The heights of the curves ($c(\mathrm{IgG_{bound}})$ for large $c_0(\mathrm{IgG})$) significantly differ from each other since the absolute concentrations are shown. However, they do not reflect the relation of the particle concentrations which is a direct consequence of the different $\Delta\varphi_{\mathrm{high}}$ values of the logistic functions. Fits of Eq. 1.45 to the conversion results yield for the IgG concentration series with the particle concentrations of 9.06 nM and 2.26 nM an estimation of K_{a} and N_{cov} (see Table 4.8). For the 566 pM IgG concentration series no converging fit could be performed due to the limited number of points in the important concentration range. The found association constants of $2.39 \times 10^8\,\mathrm{M^{-1}}$ and $5.38 \times 10^8\,\mathrm{M^{-1}}$ for a particle concentration of 9.06 nM and 2.26 nM, respectively, are within the range of literature values for the applied binding reaction between protein G and IgG ($1 \times 10^8\,\mathrm{M^{-1}}$ to $8 \times 10^8\,\mathrm{M^{-1}}$ [151]) and the numbers of protein G per MNP (18.62 and 12.12) lie in a reasonable range since the manufacturer of the SHP-G30 particles specifies a N_{cov} of 15.
The measurements of the IgG concentration series with particle concentrations of 2.26 nM and 566 pM were repeated with an increased number of samples and two other batches of the SHP-G30 particle (B1 and B2). Moreover, each sample was prepared with an additional amount of bovine serum albumin (BSA) in solution ($c(\mathrm{BSA}) = 3.76\,\mu\mathrm{M}$), which is known for its pronounced unspecific adsorption. The measured $\Delta\varphi_{\mathrm{peak}}$ values of these samples as a function of $c_0(\mathrm{IgG})$ are displayed in Fig. 4.26 including fits with the logistic function. In comparison to the first measurements (Fig. 4.24) for the samples with a 2.26 nM particle concentration higher values of $c_{0,\mathrm{half}}(\mathrm{IgG})$ are found and for all samples $\Delta\varphi_{\mathrm{high}}$ is reduced (Table 4.7). This can be explained by the unspecific adsorption and the competitive behavior of the additional BSA in solution. The estimated association constants (Table 4.8) are consequently diminished.

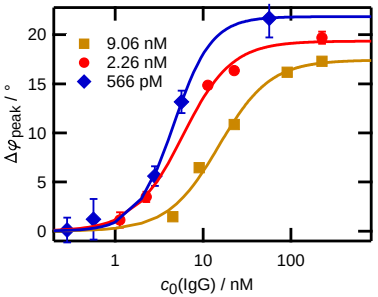

Figure 4.24: Measured $\Delta\varphi_{\mathrm{peak}}$ as a function of c_0(IgG) for IgG concentration series with SHP-G30 particle concentrations of 9.06 nM, 2.26 nM and 566 pM. Lines represent fit with logistic function (Eq. 4.2). [150] © 2015, ELSEVIER.

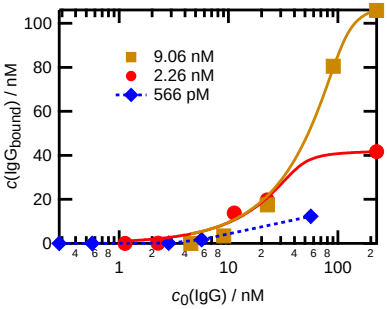

Figure 4.25: Determined concentration of antibody bound to MNPs as a function of c_0(IgG) for SHP-G30 particle concentrations of 9.06 nM, 2.26 nM and 566 pM. Solid lines represent fit with Eq. 1.45. [150] © 2015, ELSEVIER.

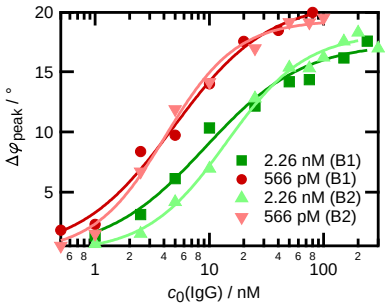

Figure 4.26: Measured $\Delta\varphi_{\mathrm{peak}}$ as a function of c_0(IgG) for IgG concentration series with SHP-G30 particle concentrations of 2.26 nM and 566 pM from two other particle batches (B1 and B2). Lines represent fit with logistic function (Eq. 4.2).

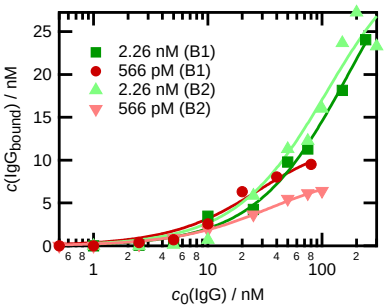

Figure 4.27: Determined concentration of antibody bound to MNPs as a function of c_0(IgG) for SHP-G30 particle concentrations of 2.26 nM and 566 pM from two other particle batches (B1 and B2). Lines represent fits with Eq. 1.45.

Table 4.7: Fit parameters of $\Delta\varphi_{\mathrm{peak}}$ as a function of the initial target molecule concentration with a logistic function for particle concentrations of 9.06 nM, 2.26 nM and 566 pM with addition of BSA (B1 and B2).

series	$\Delta\varphi_{\mathrm{high}}$ / °	$c_{0,\mathrm{half}}(\mathrm{IgG})$ / nM	α
9.06 nM	17.42(±1.05)	15.20(±2.56)	1.49(±0.33)
2.26 nM	19.34(±0.83)	5.84(±0.80)	1.56(±0.20)
566 pM	21.84(±0.7)	4.66(±0.92)	1.79(±0.29)
2.26 nM (B1)	18.21(±0.57)	14.05(±1.40)	1.25(±0.12)
566 nM (B1)	19.28(±0.54)	4.12(±0.38)	1.39(±0.16)
2.26 nM (B2)	17.39(±0.89)	9.16(±1.61)	1.01(±0.15)
566 nM (B2)	20.82(±1.22)	4.86(±0.86)	1.05(±0.15)

Table 4.8: Fit parameters of $c(\mathrm{IgG_{bound}})$ with Eq. 1.45 for IgG concentration series with particle concentrations of 9.06 nM, 2.26 nM and 566 pM and addition of BSA (B1 and B2).

series	K_{a} / M^{-1}	N_{cov}
9.06 nM	$2.39(\pm1.76)\cdot10^{8}$	12.12(±0.69)
2.26 nM	$5.38(\pm4.70)\cdot10^{8}$	18.62(±1.09)
566 pM	-	-
2.26 nM (B1)	$1.11(\pm0.57)\cdot10^{7}$	15.78(±2.27)
566 nM (B1)	$3.40(\pm0.5)\cdot10^{7}$	15.32(±0.82
2.26 nM (B2)	$6.68(\pm1.36)\cdot10^{6}$	17.74(±1.90)
566 nM (B2)	$4.91(\pm1.78)\cdot10^{7}$	22.40(±3.02)

4.3.4 Particle system comparison

The investigation of the phase lag change in the previous sections was based on measurements on single-core particles with core diameters in the range of 25 nm to 40 nm since their dynamics is still noticeably affected by proteins with a comparable low mass ($m < 150\,\mathrm{kDa}$) bound to the particle surface. Here, measurements of single- and multi-core particle systems functionalized with streptavidin (SHP-S30, BNF-S80, BNF-S100, FSR-S60) and their interaction with biotinylated antibodies (AFP-IgG) are presented. The change of the dynamics due to the bound IgG is investigated with the RMF measurement system. A detailed comparison with additional dynamic magnetic (ACS and MRX) and optical (PCCS) measurement techniques can be found in a publication of Remmer et al. [155].
For each particle type measurements before and after the addition of the biotinylated antibody were performed. The antibody concentrations were chosen with respect to the hydrodynamic particle surface according to the relation

$$\frac{\pi d_{\mathrm{h}}^2 c(\mathrm{MNP})}{c(\mathrm{IgG})} = 1.7 \times 10^{-16}\,\mathrm{m}^2 \tag{4.7}$$

to facilitate an equal coverage of IgG per particle. In order to achieve comparable signals with the dynamic magnetic measurement techniques all samples possess an iron concentration of 3.98 mM.
Table 4.9 provides a summary of the hydrodynamic sizes of the four applied particle types analyzed with ACS and PCCS before the addition of AFP-IgG. These results coincide with the investigations of the different unfunctionalized particle samples in section 4.2.1. A comparison of the hydrodynamic diameters determined by PCCS reflects the general growth of the particle size due to the functionalization. An analysis of the MRX measurement results of liquid and freeze-dried samples of the four particle types supports the previous finding that the FSR multi-core particles are less dominated by the Brownian relaxation process [155]. For the SHP and BNF samples a distinct domination of the Brownian relaxation is found. This was also reflected by the ACS measurements and the k factor determined from the ACS real part (see section 2.6), which takes into account the presence of fast Néel particles in solution.
The change of the samples hydrodynamic sizes due to the addition of AFP-IgG is well measurable with MRX, ACS, RMF and PCCS only for the

single-core particle sample SHP-S30. The change of the relaxation curves of the multi-core particles interacting with the biotinylated antibodies is significantly reduced and for the FSR-S60 sample almost not discernible. In addition, the hydrodynamic size change of FSR-S60 induces only slight effects in the RMF and ACS results, e.g. a shift of the imaginary part or a rise of the phase lag. This observation is mainly a consequence of the comparably large hydrodynamic size and the partly significant contribution of Néel particles in solution. Fig. 4.28 displays the phase lags of the single samples with and without AFP-IgG and the resulting phase lag changes in a RMF with a magnitude of 1 mT. Here, the described difference between the single- and multi-core particles regarding the change of the dynamics can be observed. Whereas the phase lag change of SHP-S30 exhibits a clear $\Delta\varphi_{\mathrm{peak}}$ of more than 12°, for the multi-core particles no positive $\Delta\varphi_{\mathrm{peak}}$ is visible. In fact, comparably small positive $\Delta\varphi$ are found for frequencies below 200 Hz, which become negative for higher frequencies. Here, BNF-S100 shows the strongest change of more than −10°. These negative $\Delta\varphi$ reflect the crossing of the phase lag spectra of the multi-core particles with and without AFP-IgG. Presumably, a similar behavior can be discovered for the SHP-S30 particle for much higher frequencies ($\omega \gg 2\pi \cdot 5\,\mathrm{kHz}$) since they possess also a slight amount of fast Néel particles in solution, which finally cause the drop of the phase lag curves at high frequencies. However, the strong negative phase lag changes measured for the multi-core particles are not only attributed to the presence of these Néel particles. In this case, a partly clustering of the particles due to the presence of multiple binding sites on the particles and the antibodies supports the described effect. The hydrodynamic sizes of the SHP-S30 samples determined with all applied techniques (Table 4.10) additionally indicate the mentioned clustering of the particles. The significant increase of d_{h} and the width of the size distribution can not be explained by single binding events. They would only form one layer of antibodies around the particle which is in the range of some nanometers recalculated from the average protein density [152] or compared to similar studies with proteins binding unspecified [95, 154] and specifically [8] to the surface of nanoparticles. Whereas the hydrodynamic sizes before the addition of AFP-IgG determined with the different measurement techniques match reasonably, after the addition distinct differences are visible. This is explained by the different models of the techniques that do not reflect the multimodality caused by the clustering or are not unambiguously solvable in this case.

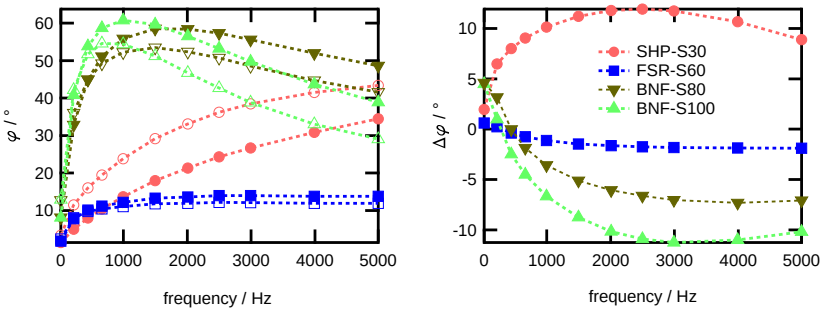

(i) (ii)

Figure 4.28: (i) Measured phase lag spectra for 1 mT rotating magnetic field of SHP-S30, FSR-S60, BNF-S80 and BNF-S100 in suspension without (filled symbols) and with AFP-IgG (empty symbols). (ii) Phase lag change upon binding of AFP-IgG. [155] © 2015, ELSEVIER.

Table 4.9: Hydrodynamic diameters of single- and multi-core particle samples determined with ACS and PCCS. For the PCCS measurements the samples were thirty times diluted. [155] © 2015, ELSEVIER.

technique	SHP-S30	BNF-S80	BNF-S100	FSR-S60
ACS	(48 ± 18)nm	(128 ± 42)nm	(179 ± 68)nm	(110 ± 56)nm
PCCS	(52 ± 10)nm	(103 ± 18)nm	(136 ± 25)nm	(86 ± 16)nm

Table 4.10: Hydrodynamic diameter of SHP-S30 sample with and without addition of AFP-IgG determined with various techniques. For the PCCS measurements the samples were thirty times diluted. [155] © 2015, ELSEVIER.

sample	PCCS	ACS	RMF	MRX
-	(52 ± 10)nm	(48 ± 18)nm	(48 ± 15)nm	(47 ± 28)nm
AFP-IgG	(103 ± 19)nm	(78 ± 70)nm	(66 ± 26)nm	(76 ± 149)nm

4.3.5 Tumor marker detection

In this section, the principle and preliminary measurement results of the quantitative detection of the medical relevant biomarker HER2 with the SHP-S30 particles and HER2-IgG antibodies in water-based test samples are presented. HER2 is a tumor-specific biomarker which can be overexpressed in the case of breast cancer ($> 30\,\%$) [156]. A quick and reliable quantification of this marker in patient serum plays an important role in the cancer therapy. For the test samples the recombinant human HER2 protein is purchased from ebioscience (Frankfurt, Germany). The non-quantitative detection of HER2 with functionalized ALP particles was reported by Lak [37].
Since the SHP-S30 particles are not directly functionalized with a receptor protein for HER2 a further step is introduced in the sample preparation and measurement process. The principle is illustrated in Fig. 4.29: Six samples with HER2 concentrations ranging from 0 nM to 74.12 nM are prepared, the pure SHP-S30 particles are added and the phase lag φ_1 is measured. In a next step, a HER2-IgG solution with a concentration of 10 nM is injected into each sample. Then φ_2 is determined and the phase lag change $\Delta\varphi$ is calculated. Here, it has to be taken into account that the increase of the hydrodynamic volume is based on pairs of HER2-IgG and HER2. Thus, in the measurement results of $\Delta\varphi$ (Fig. 4.30) the phase lag change of the sample without HER2 is subtracted from the phase lag changes of the other samples. This measurement series was performed for two particle concentrations: 1 nM and 2 nM. Interestingly, a clear difference is observed in Fig. 4.30 for the two particle concentrations. Whereas for $c(\mathrm{MNP}) = 1\,\mathrm{nM}$ the two lowest HER2 concentrations cause no significant $\Delta\varphi$, for $c(\mathrm{MNP}) = 2\,\mathrm{nM}$ all HER2 concentrations can be detected and an overall increase of $\Delta\varphi$ is observed. In addition, the $\Delta\varphi$ curves for the higher particle concentration are much narrower. This behavior can be explained by the formation of clusters with increasing particle concentration since again multiple binding sites are present. Apparently, $\Delta\varphi$ becomes negative for higher frequencies which is in accordance with the results from the previous section.
The medical relevant cutoff value for the concentration determination of HER2 in serum during a breast cancer therapy is in the range of 150 pM to 200 pM (15 ng/mL [156]). Although this threshold is not achieved by the presented configuration of measurement system and nanoparticles, the potential of the RMF based concept for the quantitative detection of small

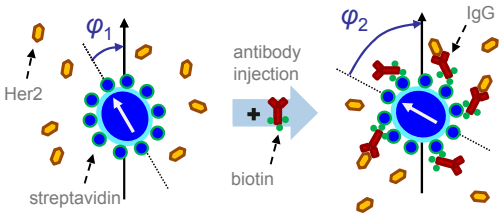

Figure 4.29: Principle of Her2 biomarker detection with streptavidin functionalized particles and biotinylated antibody.

biomolecules directly in solution could be highlighted, especially with respect to an optical detection scheme that detects even lower particle concentrations. In addition, the capability of the reference system, which was mainly developed for the principle investigation of the MNPs' RMF dynamics, in combination with the applied single-core particles to detect biomolecules in the nanomolar range is sufficient for other clinical biomarkers, e.g. the C-reactive protein (CRP) in the field of cardiovascular diseases [157].

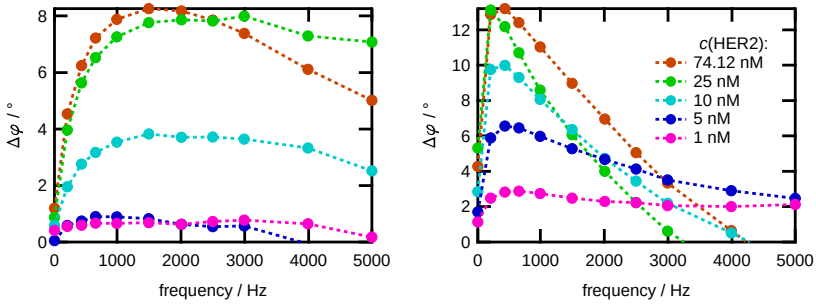

(i) (ii)

Figure 4.30: Measurement of phase lag change due to HER2 biomarker bound to SHP-S30 particles after injection of 10 nM HER2-IgG with particle concentrations of (i) $c(\mathrm{MNP}) = 1\,\mathrm{nM}$ and (ii) $c(\mathrm{MNP}) = 2\,\mathrm{nM}$. The phase lag change of a reference sample without HER2 is subtracted from the displayed phase lag change spectra.

Conclusion and outlook

The dynamic response of suspended magnetic nanoparticles to rotating magnetic fields was subject of this work. A measurement system based on a magnetic detection was developed and utilized for measurements on different magnetic nanoparticle systems. The physical quantity for the characterization of this dynamics is the phase lag between the MNP ensemble magnetization and the RMF. This work was carried out in the course of the NAMDIATREAM project and supported the investigation and realization of a homogeneous bioassay concept based on a sensitive optical biomolecule detection with rod-shaped magnetic nanoparticles in rotating magnetic fields.

The detection unit of the RMF system presented in this work comprises a gradiometric arrangement of fluxgate magnetometers, thus, enabling a comparably robust detection of the stray field of MNP suspensions outside a magnetically shielded room. The possible parameter variations of the RMF generation unit ($\mu_0 H \leq 9.1\,\mathrm{mT}$, $\omega/2\pi \leq 5\,\mathrm{kHz}$) enable an investigation of different magnetic nanoparticle systems with hydrodynamic diameters ranging from 35 nm to several 100 nm, and the sensitive fluxgate magnetometers facilitate a detection of 150 µL MNP suspensions with iron concentrations even below 0.005 g/L.

Different physical models for the description of the magnetization dynamics of magnetic nanoparticle ensembles in rotating magnetic fields were introduced. The results of a numerical solution of the Fokker-Planck equation adopted for magnetic nanoparticles in a RMF matched perfectly the measurement results of different particle systems. Furthermore, an empirical model was derived which is well applicable for the design and analysis of RMF based magnetic nanoparticle measurements. This model exhibits significantly reduced phase and magnitude errors for large Langevin parameters ($\xi \gg 1$) compared to other magnetization equation models.

The influence of the particle parameters could be studied with measurements on spherical single- and multi-core as well as rod-shaped magnetic nanoparticles. The predicted inverse tangent dependence of the phase lag on the RMF frequency was found for all particle systems. The rise of this

phase lag as a function of the frequency depends significantly on the particle and suspension parameters in accordance with the modified Brownian time constant $\tau_\perp$. In this context, the effect of the hydrodynamic size, the magnetic moment, the corresponding size distributions and the temperature could be illustrated with measurements. Additional particle characterization techniques (e.g. ACS and PCCS) supported the particle parameters obtained by simulating the measured phase lags. A comparison of the RMF with the alternating field excitation resulted in significant differences of the MNP dynamics for large Langevin parameters ($\xi \gg 1$), e.g. a more pronounced spreading of the phase lag with the field magnitude was found for the RMF.
The concept of the RMF bioassay which is based on a phase lag change induced by biomolecules binding to the particle surface and affecting the MNP dynamics could be proofed with two different particle functionalizations. For instance, sample series with protein G functionalized single-core particles and varying antibody concentrations enabled the successful investigation of a quantitative biomolecule detection. In this case, well measurable phase lag changes of up to 25° were caused. Recorded calibration curves could be successfully fitted with logistic functions and enabled a comparison of the influence of the particle parameters on the bioassay results. For the applied single-core particles, a core diameter of 30 nm was identified to be the optimum since this particle is clearly dominated by the Brownian relaxation, possesses a comparably high magnetic moment but its hydrodynamic size is still noticeably influenced by small biomolecules. Multi-core particles turned out to be unsuitable for the detection of biomolecules based on single binding events, instead detection schemes resulting in a clustering of the particles are appropriate. Furthermore, the identified differences between the RMF and alternating field excitation resulted in an increased phase lag change for binding experiments with single-core particles in rotating magnetic fields. In this context, simulations supported the finding that a wide hydrodynamic size distribution reduces significantly the phase lag change caused by bound biomolecules. Finally, the underlying binding reactions could be reasonably analyzed and a medical relevant biomarker could be quantitatively detected.

For the modeling of RMF bioassay results obtained with rod-shaped nanoparticles, a physical model incorporating only the Brownian particle dynamics is completely sufficient. Due to their pronounced shape anisotropy, they are clearly dominated by the Brownian relaxation process, even with larger pro-

teins bound to their surface. For spherical particles, such a clear domination is not given in all cases. For some particles, a modeling with the discussed theories resulted in insufficient matches. Here, a model incorporating the Brownian and Néel relaxation as well as their overlap for the description of the rotational dynamics with $\xi > 1$ would solve the problem.
Regarding the biomedical application of the RMF concept clinical investigations need to be carried out, especially with respect to the specificity of the biomolecule recognition and unspecific bindings in serum. The magnetic detection scheme can be improved with optimized MNP size distributions and increased field frequencies and magnitudes while utilizing air coils for the detection. Further applications based on magnetic nanoparticles in rotating magnetic fields are even possible. For instance, the impact of a RMF excitation of MNPs in hyperthermia applications is discussed [158].

A Appendix

A.1 Residual RMF component error

A residual component of the RMF excitation (φ_R and B_R) in the measurement signal, expressed by φ_M and B_M, cause errors since the phase lag φ and magnitude B_S of a MNP sample in the RMF can not be distinguished from the residual components. Here, a mathematical description of the deviation of φ_M and B_M from φ and B_S, respectively, as a function of the residual RMF and MNP sample components is presented.
In general, φ_M and B_M can be expressed as:

$$\varphi_\mathrm{M} = \arctan\left(\frac{B_\mathrm{S}\sin(\varphi) + B_\mathrm{R}\sin(\varphi_\mathrm{R})}{B_\mathrm{S}\cos(\varphi) + B_\mathrm{R}\cos(\varphi_\mathrm{R})}\right) \tag{A.1}$$

and

$$B_\mathrm{M} = \sqrt{\left(B_\mathrm{S}\sin(\varphi) + B_\mathrm{R}\sin(\varphi_\mathrm{R})\right)^2 + \left(B_\mathrm{S}\cos(\varphi) + B_\mathrm{R}\cos(\varphi_\mathrm{R})\right)^2}. \tag{A.2}$$

For the calculation of the deviation $\varphi_\mathrm{M} - \varphi$ and the relation $B_\mathrm{M}/B_\mathrm{S}$ as a function of the residual RMF and MNP sample components, φ_R can be set to zero since one rotation of φ covers all possible angles between φ and φ_R. Finally, the formulas are defined as:

$$\varphi_\mathrm{M} - \varphi = \arctan\left(\frac{\sin(\varphi)}{B_\mathrm{R}/B_\mathrm{S} + \cos(\varphi)}\right) - \varphi \tag{A.3}$$

and

$$B_\mathrm{M}/B_\mathrm{S} = \sqrt{\left(\sin(\varphi)\right)^2 + \left(B_\mathrm{R}/B_\mathrm{S} + \cos(\varphi)\right)^2}. \tag{A.4}$$

Table A.1: Iron concentration c(Fe) of BNF80 and SHP30 concentrations series samples. The phase lag and magnitude are measured for each sample in a 1 mT RMF with frequencies of 222 Hz and 5 kHz. The corresponding mean values and standard deviations are based on ten measurements.

particle	c(Fe) / g/L	$\varphi_{\mathrm{M,222\,Hz}}$ / °	$B_{\mathrm{M,222\,Hz}}$ / nT	$\varphi_{\mathrm{M,5\,kHz}}$ / °	$B_{\mathrm{M,5\,kHz}}$ / nT
BNF80	8	27.16 ± 0.01	2179.34 ± 0.33	54.02 ± 0.18	340.73 ± 0.13
BNF80	3.2	26.93 ± 0.01	878.70 ± 0.25	54.38 ± 0.11	137.18 ± 0.16
BNF80	1.067	26.81 ± 0.02	293.188 ± 0.07	54.72 ± 0.22	45.89 ± 0.06
BNF80	0.533	26.7104 ± 0.04	147.40 ± 0.14	54.91 ± 0.51	23.27 ± 0.10
BNF80	0.133	27.32 ± 0.14	35.55 ± 0.05	56.63 ± 1.19	5.65 ± 0.07
BNF80	0.053	28.54 ± 0.36	13.70 ± 0.09	62.20 ± 4.00	2.25 ± 0.07
BNF80	0.013	34.16 ± 3.56	3.01 ± 0.24	70.36 ± 25.40	0.71 ± 0.09
BNF80	0.0053	67.46 ± 15.19	0.86 ± 0.09	114.46 ± 28.96	0.50 ± 0.17
SHP30	5	5.51 ± 0.01	3469.88 ± 0.58	30.23 ± 0.01	2631.67 ± 0.55
SHP30	1.667	5.53 ± 0.01	1125.67 ± 0.77	30.18 ± 0.01	857.19 ± 0.56
SHP30	0.667	5.38 ± 0.01	454.97 ± 0.13	29.98 ± 0.02	346.44 ± 0.08
SHP30	0.333	5.41 ± 0.02	216.82 ± 0.20	30.11 ± 0.05	165.65 ± 0.17
SHP30	0.133	5.55 ± 0.05	86.70 ± 0.17	30.30 ± 0.14	66.14 ± 0.17
SHP30	0.05	5.54 ± 0.12	31.716 ± 0.09	30.18 ± 0.39	24.29 ± 0.09
SHP30	0.0167	5.40 ± 0.46	8.20 ± 0.09	31.08 ± 1.19	6.36 ± 0.10
SHP30	0.0083	5.50 ± 0.89	4.80 ± 0.07	32.22 ± 2.48	3.78 ± 0.07
SHP30	0.0033	4.88 ± 1.42	1.77 ± 0.08	28.21 ± 4.86	1.524 ± 0.09
SHP30	0.00167	9.52 ± 4.60	0.76 ± 0.12	39.95 ± 9.86	0.68 ± 0.078

A.2 Concentration series

In this section further measurement values of the BNF80 and SHP30 concentration series (see section 3.4) in a 1 mT RMF are presented. The values for a RMF frequency of 222 Hz and 5 kHz are shown in Table A.1. The displayed mean values and standard deviations are based on ten measurement repetitions.

Publications and presentations

Publications

(1) H. Remmer, J. Dieckhoff, M. Schilling, and F. Ludwig, Suitability of magnetic single- and multi-core nanoparticles to detect protein binding with dynamic magnetic measurement techniques, Journal of Magnetism and Magnetic Materials, vol. 380, pp. 236–240, Apr. 2015.

(2) J. Dieckhoff, S. Schrittwieser, J. Schotter, H. Remmer, M. Schilling, and F. Ludwig, Single-core magnetic markers in rotating magnetic field based homogeneous bioassays and the law of mass action, Journal of Magnetism and Magnetic Materials, vol. 380, pp. 205–208, Apr. 2015.

(3) F. Ludwig, C. Kuhlmann, T. Wawrzik, J. Dieckhoff, A. Lak, A. P. Kandhar, R. M. Ferguson, S. J. Kemp, and K. M. Krishnan, Dynamic Magnetic Properties of Optimized Magnetic Nanoparticles for Magnetic Particle Imaging, IEEE Transactions on Magnetics, vol. 50, no. 11, pp. 1–4, Nov. 2014.

(4) J. Dieckhoff, S. Schrittwieser, J. Schotter, H. Remmer, M. Schilling, and F. Ludwig, Single-core magnetic markers in rotating magnetic field based homogeneous bioassays and the law of mass action, Journal of Magnetism and Magnetic Materials, Oct. 2014.

(5) J. Dieckhoff, M. Schilling, and F. Ludwig, Magnetic marker based homogeneous bioassays utilizing rotating magnetic fields, Journal of Applied Physics, vol. 115, no. 17, p. 17B304, May 2014.

(6) J. Dieckhoff, A. Lak, M. Schilling, and F. Ludwig, Protein detection with magnetic nanoparticles in a rotating magnetic field, Journal of Applied Physics, vol. 115, no. 2, p. 024701, Jan. 2014.

(7) S. Schrittwieser, F. Ludwig, J. Dieckhoff, A. Tschoepe, A. Guenther, M. Richter, A. Huetten, H. Brueckl, and J. Schotter, Direct Protein Detection in the Sample Solution by Monitoring Rotational Dynamics of Nickel Nanorods, Small, vol. 10, no. 2, pp. 407–411, Jan. 2014.

(8) A. Lak, F. Ludwig, J. M. Scholtyssek, J. Dieckhoff, K. Fiege, and M. Schilling, Size Distribution and Magnetization Optimization of Single-Core Iron Oxide Nanoparticles by Exploiting Design of Experiment Methodology, IEEE Transactions on Magnetics, vol. 49, no. 1, pp. 201–207, Jan. 2013.

(9) A. Lak, J. Dieckhoff, F. Ludwig, J. M. Scholtyssek, O. Goldmann, H. Lünsdorf, D. Eberbeck, A. Kornowski, M. Kraken, F. J. Litterst, K. Fiege, P. Mischnick, and M. Schilling, Highly stable monodisperse PEGylated iron oxide nanoparticle aqueous suspensions: a nontoxic tracer for homogeneous magnetic bioassays, Nanoscale, vol. 5, no. 23, p. 11447, 2013.

(10) J. Dieckhoff, T. Yoshida, K. Enpuku, M. Schilling, and F. Ludwig, Homogeneous Bioassays Based on the Manipulation of Magnetic Nanoparticles by Rotating and Alternating Magnetic Fields - A Comparison, IEEE Transactions on Magnetics, vol. 48, no. 11, pp. 3792–3795, Nov. 2012.

(11) S. Schrittwieser, F. Ludwig, J. Dieckhoff, K. Soulantica, G. Viau, L.-M. Lacroix, S. M. Lentijo, R. Boubekri, J. Maynadié, A. Huetten, H. Brueckl, and J. Schotter, Modeling and Development of a Biosensor Based on Optical Relaxation Measurements of Hybrid Nanoparticles, ACS Nano, vol. 6, no. 1, pp. 791–801, Jan. 2012.

(12) T. Yoshida, K. Enpuku, F. Ludwig, J. Dieckhoff, T. Wawrzik, A. Lak, and M. Schilling, Characterization of Resovist® Nanoparticles for Magnetic Particle Imaging, in Magnetic Particle Imaging, vol. 140, T. M. Buzug and J. Borgert, Eds. Berlin, Heidelberg: Springer Berlin Heidelberg, 2012, pp. 3–7.

(13) T. Yoshida, K. Enpuku, J. Dieckhoff, M. Schilling, and F. Ludwig, Magnetic fluid dynamics in a rotating magnetic field, Journal of Applied Physics, vol. 111, no. 5, p. 053901, 2012.

(14) J. Dieckhoff, M. Schilling, and F. Ludwig, Fluxgate based detection of magnetic nanoparticle dynamics in a rotating magnetic field, Applied Physics Letters, vol. 99, no. 11, p. 112501, 2011.

Presentations

(1) J. Dieckhoff, T. Yoshida, M. Schilling, F. Ludwig, Response of spherical magnetic nanoparticles to rotating magnetic fields (Oral), 11th German Ferrofluid Workshop, Benediktbeuern (2011).

(2) J. Dieckhoff, T. Yoshida, K. Enpuku, M. Schilling, and F. Ludwig, Homogeneous Bioassays Based on the Manipulation of Magnetic Nanoparticles by Rotating and Alternating Magnetic Fields – a Comparison (Oral), IEEE International Magnetics Conference, Vancouver (2012).

(3) J. Dieckhoff, M. Schilling, and F. Ludwig, Magnetic nanoparticle binding experiments in rotating magnetic fields (Poster), 12th German Ferrofluid Workshop, Benediktbeuern (2012).

(4) J. Dieckhoff, M. Schilling, and F. Ludwig, Homogeneous bioassay based on specifically labeled magnetic nanoparticles in a rotating magnetic field (Poster/Oral), NAMDIATREAM Winter School, Villars-sur-Ollon (2013).

(5) J. Dieckhoff, M. Schilling, and F. Ludwig, Bioassay based on the response of magnetic nanoparticles to rotating magnetic fields (Oral), Frühjahrstagung des Arbeitskreises Festkörperphysik der DPG, Regensburg (2013).

(6) J. Dieckhoff, M. Schilling, and F. Ludwig, Homogeneous bioassay development based on magnetic nanoparticles in rotating magnetic fields (Poster), 3rd P^3AGI Imaging Workshop, Göttingen (2013).

(7) J. Dieckhoff, M. Schilling, and F. Ludwig, Magnetic marker based homogeneous bioassays utilizing rotating magnetic fields (Oral), 58th Annual Conference on Magnetism and Magnetic Materials, Denver (2013).

(8) J. Dieckhoff, S. Schrittwieser, J. Schotter, H. Remmer, M. Schilling, and F. Ludwig, Single-core magnetic markers in rotating magnetic field based homogeneous bioassays and the law of mass action (Poster/Oral), 10th International Conference on the Scientific and Clinical Applications of Magnetic Carriers, Dresden (2014).

(9) J. Dieckhoff, H. Remmer, M. Schilling, and F. Ludwig, Quantitative biomarker detection with magnetic nanoparticles (Oral), 48th DGBMT Annual Conference, Hannover (2014).

Bibliography

[1] L. Néel, Théorie du trainage magnétique des ferromagnétiques au grains fin avec applications aux terres cuites, Annales Geophysicae 5 (1949) 99–136.

[2] W. F. Brown, Thermal fluctuations of a single-domain particle, Physical Review 130 (1963) 1677–1686.

[3] S. Schrittwieser, F. Ludwig, J. Dieckhoff, K. Soulantica, G. Viau, L.-M. Lacroix, S. M. Lentijo, R. Boubekri, J. Maynadié, A. Huetten, H. Brueckl, J. Schotter, Modeling and development of a biosensor based on optical relaxation measurements of hybrid nanoparticles, ACS Nano 6 (1) (2012) 791–801.

[4] P. Yager, G. J. Domingo, J. Gerdes, Point-of-Care Diagnostics for Global Health, Annual Review of Biomedical Engineering 10 (1) (2008) 107–144.

[5] W. Weitschies, R. Kötitz, T. Bunte, L. Trahms, Determination of relaxing or remanent nanoparticle magnetization provides a novel binding-specific technique for the evaluation of immunoassays, Pharmaceutical and Pharmacological Letters (7) (1997) 1–4.

[6] E. Heim, F. Ludwig, M. Schilling, Binding assays with streptavidin-functionalized superparamagnetic nanoparticles and biotinylated analytes using fluxgate magnetorelaxometry, Journal of Magnetism and Magnetic Materials 321 (10) (2009) 1628–1631.

[7] J. Connolly, T. G. St Pierre, Proposed biosensors based on time-dependent properties of magnetic fluids, Journal of Magnetism and Magnetic Materials 225 (1-2) (2001) 156–160.

[8] S.-H. Chung, A. Hoffmann, K. Guslienko, S. D. Bader, C. Liu, B. Kay, L. Makowski, L. Chen, Biological sensing with magnetic nanoparticles using Brownian relaxation (invited), Journal of Applied Physics 97 (10) (2005) 10R101.

[9] C.-Y. Hong, C. C. Wu, Y. C. Chiu, S. Y. Yang, H. E. Horng, H. C. Yang, Magnetic susceptibility reduction method for magnetically labeled immunoassay, Applied Physics Letters 88 (21) (2006) 212512.

[10] L. Tu, Y. Jing, Y. Li, J.-P. Wang, Real-time measurement of Brownian relaxation of magnetic nanoparticles by a mixing-frequency method, Applied Physics Letters 98 (21) (2011) 213702.

[11] B. H. McNaughton, R. R. Agayan, R. Clarke, R. G. Smith, R. Kopelman, Single bacterial cell detection with nonlinear rotational frequency shifts of driven magnetic microspheres, Applied Physics Letters 91 (22) (2007) 224105.

[12] A. Ranzoni, G. Sabatte, L. J. van IJzendoorn, M. W. J. Prins, One-Step Homogeneous Magnetic Nanoparticle Immunoassay for Biomarker Detection Directly in Blood Plasma, ACS Nano 6 (4) (2012) 3134–3141.

[13] F. Wittbracht, B. Eickenberg, A. Weddemann, A. Hütten, Towards a programmable microfluidic valve: Formation dynamics of two-dimensional magnetic bead arrays in transient magnetic fields, Journal of Applied Physics 109 (11) (2011) 114503.

[14] J.-C. Bacri, A. Cebers, R. Perzynski, Behavior of a magnetic fluid microdrop in a rotating magnetic field, Physical Review Letters 72 (17) (1994) 2705–2708.

[15] Q. A. Pankhurst, N. T. K. Thanh, S. K. Jones, J. Dobson, Progress in applications of magnetic nanoparticles in biomedicine, Journal of Physics D: Applied Physics 42 (22) (2009) 224001.

[16] S. Miltenyi, W. Müller, W. Weichel, A. Radbruch, High gradient magnetic cell separation with MACS, Cytometry 11 (2) (1990) 231–238.

[17] A. Frenzel, C. Bergemann, G. Köhl, T. Reinard, Novel purification system for 6xhis-tagged proteins by magnetic affinity separation, Journal of Chromatography B 793 (2) (2003) 325–329.

[18] I. Safarik, M. Safarikova, Magnetic techniques for the isolation and purification of proteins and peptides, BioMagnetic Research and Technology 2 (2004) 7.

[19] A. S. Lübbe, C. Alexiou, C. Bergemann, Clinical Applications of Magnetic Drug Targeting, Journal of Surgical Research 95 (2) (2001) 200–206.

[20] Y. Okuhata, Delivery of diagnostic agents for magnetic resonance imaging, Advanced Drug Delivery Reviews 37 (1-3) (1999) 121–137.

[21] M. K. Yu, J. Park, S. Jon, Magnetic nanoparticles and their applications in image-guided drug delivery, Drug Delivery and Translational Research 2 (1) (2012) 3–21.

[22] J. Zhang, R. Misra, Magnetic drug-targeting carrier encapsulated with thermosensitive smart polymer: Core–shell nanoparticle carrier and drug release response, Acta Biomaterialia 3 (6) (2007) 838–850.

[23] P. Wust, B. Hildebrandt, G. Sreenivasa, B. Rau, J. Gellermann, H. Riess, R. Felix, P. Schlag, Hyperthermia in combined treatment of cancer, The Lancet Oncology 3 (8) (2002) 487–497.

[24] B. Thiesen, A. Jordan, Clinical applications of magnetic nanoparticles for hyperthermia, International Journal of Hyperthermia 24 (6) (2008) 467–474.

[25] B. Gleich, J. Weizenecker, Tomographic imaging using the nonlinear response of magnetic particles, Nature 435 (7046) (2005) 1214–1217.

[26] J. Weizenecker, B. Gleich, J. Rahmer, H. Dahnke, J. Borgert, Three-dimensional real-time in vivo magnetic particle imaging, Physics in Medicine and Biology 54 (5) (2009) L1–L10.

[27] J. Borgert, J. D. Schmidt, I. Schmale, C. Bontus, B. Gleich, B. David, J. Weizenecker, J. Jockram, C. Lauruschkat, O. Mende, M. Heinrich, A. Halkola, J. Bergmann, O. Woywode, J. Rahmer, Perspectives on clinical magnetic particle imaging, Biomedizinische Technik/Biomedical Engineering 58 (6).

[28] R. Kotitz, H. Matz, L. Trahms, H. Koch, W. Weitschies, T. Rheinlander, W. Semmler, T. Bunte, SQUID based remanence measurements for immunoassays, IEEE Transactions on Appiled Superconductivity 7 (2) (1997) 3678–3681.

[29] Y. Mitamura, S. Takahashi, K. Kano, E. Okamoto, S. Murabayashi, I. Nishimura, T.-a. Higuchi, Sealing Performance of a Magnetic Fluid Seal for Rotary Blood Pumps, Artificial Organs 33 (9) (2009) 770–773.

[30] K. Raj, R. Moskowitz, Commercial applications of ferrofluids, Journal of Magnetism and Magnetic Materials 85 (1-3) (1990) 233–245.

[31] M. Pinho, J. Génevaux, N. Dauchez, B. Brouard, P. Collas, H. Mézière, Damping induced by ferrofluid seals in ironless loudspeaker, Journal of Magnetism and Magnetic Materials 356 (2014) 125–130.

[32] H. R. Youn, D. J. Lee, J. R. Youn, Y. S. Song, Ferrohydrodynamic energy harvesting based on air droplet movement, Nano Energy

[33] D. Faika, Modifikation magnetischer Nanoträger für den Einsatz in enzymatisch katalysierten Reaktionen, Ph.D. thesis, Technische Universität Hamburg-Harburg, Denickestr. 22, 21071 Hamburg (2013).

[34] S. Laurent, D. Forge, M. Port, A. Roch, C. Robic, L. Vander Elst, R. N. Muller, Magnetic Iron Oxide Nanoparticles: Synthesis, Stabilization, Vectorization, Physicochemical Characterizations, and Biological Applications, Chemical Reviews 108 (6) (2008) 2064–2110.

[35] R. Blakemore, Magnetotactic bacteria, Science 190 (4212) (1975) 377–379.

[36] A.-H. Lu, E. Salabas, F. Schüth, Magnetic Nanoparticles: Synthesis, Protection, Functionalization, and Application, Angewandte Chemie International Edition 46 (8) (2007) 1222–1244.

[37] A. Lak, Synthesis and Characterization of Magnetic Iron Oxide Nanoparticles, Mensch & Buch, Berlin, 2014.

[38] N. L. Adolphi, D. L. Huber, H. C. Bryant, T. C. Monson, D. L. Fegan, J. Lim, J. E. Trujillo, T. E. Tessier, D. M. Lovato, K. S. Butler, P. P. Provencio, H. J. Hathaway, S. A. Majetich, R. S. Larson, E. R. Flynn, Characterization of single-core magnetite nanoparticles for magnetic imaging by SQUID relaxometry, Physics in Medicine and Biology 55 (19) (2010) 5985–6003.

[39] A. Lak, F. Ludwig, J. M. Scholtyssek, J. Dieckhoff, K. Fiege, M. Schilling, Size Distribution and Magnetization Optimization of Single-Core Iron Oxide Nanoparticles by Exploiting Design of Experiment Methodology, IEEE Transactions on Magnetics 49 (1) (2013) 201–207.

[40] F. Ludwig, A. Guillaume, M. Schilling, N. Frickel, A. M. Schmidt, Determination of core and hydrodynamic size distributions of CoFe[sub 2]O[sub 4] nanoparticle suspensions using ac susceptibility measurements, Journal of Applied Physics 108 (3) (2010) 033918.

[41] T. T. Thuy, S. Maenosono, N. T. K. Thanh, Next generation magnetic nanoparticles for biomedical applications, in: N. T. K. Thanh (Ed.), Magnetic nanoparticles: from fabrication to clinical applications: theory to therapy, chemistry to clinic, bench to bedside, CRC Press, Boca Raton, FL, 2012, pp. 99–126.

[42] V. F. Puntes, K. M. Krishnan, A. P. Alivisatos, Colloidal Nanocrystal Shape and Size Control: The Case of Cobalt, Science 291 (5511) (2001) 2115–2117.

[43] K. A. Atmane, C. Michel, J.-Y. Piquemal, P. Sautet, P. Beaunier, M. Giraud, M. Sicard, S. Nowak, R. Losno, G. Viau, Control of the anisotropic shape of cobalt nanorods in the liquid phase: from experiment to theory... and back, Nanoscale 6 (5) (2014) 2682.

[44] A. Günther, P. Bender, A. Tschöpe, R. Birringer, Rotational diffusion of magnetic nickel nanorods in colloidal dispersions, Journal of Physics: Condensed Matter 23 (32) (2011) 325103.

[45] M. A. M. Gijs, Magnetic bead handling on-chip: new opportunities for analytical applications, Microfluidics and Nanofluidics

[46] V. Schaller, G. Wahnström, A. Sanz-Velasco, S. Gustafsson, E. Olsson, P. Enoksson, C. Johansson, Effective magnetic moment of magnetic multicore nanoparticles, Physical Review B 80 (9).

[47] I. Safarik, M. Safarikova, Magnetic Nanoparticles for In Vitro Biological and Medical Applications, in: N. T. K. Thanh (Ed.), Magnetic nanoparticles: from fabrication to clinical applications: theory to therapy, chemistry to clinic, bench to bedside, CRC Press, Boca Raton, FL, 2012, pp. 215–242.

[48] Structure and Magnetism in Magnetic Nanoparticles, in: N. T. K. Thanh, D. Ortega (Eds.), Magnetic nanoparticles: from fabrication to clinical applications: theory to therapy, chemistry to clinic, bench to bedside, CRC Press, Boca Raton, FL, 2012, pp. 3–44.

[49] B. Kozissnik, L. A. W. Green, K. A. Chester, N. T. K. Thanh, Strategies for functionalisation of magnetic nanoparticles for biological targets, in: N. T. K. Thanh (Ed.), Magnetic nanoparticles: from fabrication to clinical applications: theory to therapy, chemistry to clinic, bench to bedside, CRC Press, Boca Raton, FL, 2012, pp. 129–150.

[50] R. E. Rosensweig, Ferrohydrodynamics, Dover Publications, 1997.

[51] S. Odenbach, L. M. Pop, A. Y. Zubarev, Rheological properties of magnetic fluids and their microstructural background, GAMM-Mitteilungen 30 (1) (2007) 195–204.

[52] S. Blundell, Magnetism in condensed matter, Oxford University Press, Oxford; New York, 2001.

[53] D. L. Leslie-Pelecky, R. D. Rieke, Magnetic Properties of Nanostructured Materials, Chemistry of Materials 8 (8) (1996) 1770–1783.

[54] X. Batlle, A. Labarta, Finite-size effects in fine particles: magnetic and transport properties, Journal of Physics D: Applied Physics 35 (6) (2002) R15–R42.

[55] F. Ludwig, E. Heim, M. Schilling, Characterization of superparamagnetic nanoparticles by analyzing the magnetization and relaxation dynamics using fluxgate magnetometers, Journal of Applied Physics 101 (11) (2007) 113909.

[56] C. P. Bean, J. D. Livingston, Superparamagnetism, Journal of Applied Physics 30 (4) (1959) S120.

[57] E. F. Kneller, F. E. Luborsky, Particle Size Dependence of Coercivity and Remanence of Single-Domain Particles, Journal of Applied Physics 34 (3) (1963) 656.

[58] S. Gudoshnikov, B. Liubimov, A. Popova, N. Usov, The influence of a demagnetizing field on hysteresis losses in a dense assembly of superparamagnetic nanoparticles, Journal of Magnetism and Magnetic Materials 324 (22) (2012) 3690–3694.

[59] M. M. Tirado, J. G. de la Torre, Rotational dynamics of rigid, symmetric top macromolecules. Application to circular cylinders, The Journal of Chemical Physics 73 (4) (1980) 1986.

[60] P. C. Fannin, Measurement of the Neel relaxation of magnetic particles in the frequency range 1 kHz to 160 MHz, Journal of Physics D: Applied Physics 24 (1) (1991) 76–77.

[61] R. Chantrell, B. Tanner, S. Hoon, Determination of the magnetic anisotropy of ferrofluids from torque magnetometry data, Journal of Magnetism and Magnetic Materials 38 (1) (1983) 83–92.

[62] T. Yoshida, K. Enpuku, Simulation and Quantitative Clarification of AC Susceptibility of Magnetic Fluid in Nonlinear Brownian Relaxation Region, Japanese Journal of Applied Physics 48 (12) (2009) 127002.

[63] A. Pshenichnikov, V. Mekhonoshin, A. Lebedev, Magnetogranulometric analysis of concentrated ferrocolloids, Journal of Magnetism and Magnetic Materials 161 (1996) 94–102.

[64] M. Kühlmeyer, Statistische Auswertungsmethoden für Ingenieure: mit Praxisbeispielen, Springer, Berlin, 2001.

[65] D. V. Berkov, P. Görnert, N. Buske, C. Gansau, J. Mueller, M. Giersig, W. Neimann, D. Su, New method for the determination of the particle magnetic moment distribution in a ferrofluid, Journal of Physics D: Applied Physics (33) (2000) 331–337.

[66] D. Chescoe, Royal Microscopical Society (Great Britain), The operation of transmission and scanning electron microscopes, no. 20 in Microscopy handbooks, Oxford University Press ; Royal Microscopical Society, Oxford ; New York : Oxford, 1990.

[67] R. Finsy, Particle sizing by quasi-elastic light scattering, Advances in Colloid and Interface Science 52 (1994) 79–143.

[68] C. F. Bohren, D. R. Huffman, Absorption and scattering of light by small particles, Wiley, New York, 1983.

[69] L. H. Hanus, H. J. Ploehn, Conversion of Intensity-Averaged Photon Correlation Spectroscopy Measurements to Number-Averaged Particle Size Distributions. 1. Theoretical Development, Langmuir 15 (9) (1999) 3091–3100.

[70] P. J. Patty, B. J. Frisken, Direct determination of the number-weighted mean radius and polydispersity from dynamic light-scattering data, Applied Optics 45 (10) (2006) 2209.

[71] V. Filipe, A. Hawe, W. Jiskoot, Critical Evaluation of Nanoparticle Tracking Analysis (NTA) by NanoSight for the Measurement of Nanoparticles and Protein Aggregates, Pharmaceutical Research 27 (5) (2010) 796–810.

[72] W. Lämmle, Nanometre particle sizing and stability measurement using a table-top PCCS system, Lab-Plus international (2005) 19–24.

[73] D. Eberbeck, F. Wiekhorst, S. Wagner, L. Trahms, How the size distribution of magnetic nanoparticles determines their magnetic particle imaging performance, Applied Physics Letters 98 (18) (2011) 182502.

[74] A. Lak, M. Kraken, F. Ludwig, A. Kornowski, D. Eberbeck, S. Sievers, F. J. Litterst, H. Weller, M. Schilling, Size dependent structural and magnetic properties of FeO–Fe3o4 nanoparticles, Nanoscale 5 (24) (2013) 12286.

[75] P. C. Fannin, B. K. P. Scaife, S. W. Charles, The measurement of the frequency dependent susceptibility of magnetic colloids, Journal of Magnetism and Magnetic Materials 72 (1988) 95–108.

[76] P. Debye, Polar molecules, Dover, New York, 1929.

[77] T. Yoshida, K. Enpuku, Nonlinear Behavior of Magnetic Fluid in Brownian Relaxation: Numerical Simulation and Derivation of Empirical Model, in: T. M. Buzug, J. Borgert (Eds.), Magnetic Particle Imaging, Vol. 140, Springer Berlin Heidelberg, Berlin, Heidelberg, 2012, pp. 9–13.

[78] A. Lak, A. F. Thünemann, M. Schilling, F. Ludwig, Resolving particle size modality in bi-modal iron oxide nanoparticle suspensions, Journal of Magnetism and Magnetic Materials 380 (2015) 140–143.

[79] R. Chantrell, S. Hoon, B. Tanner, Time-dependent magnetization in fine-particle ferromagnetic systems, Journal of Magnetism and Magnetic Materials 38 (2) (1983) 133–141.

[80] D. Eberbeck, S. Hartwig, U. Steinhoff, L. Trahms, Description of the magnetisation decay in ferrofluids with a narrow particle size distribution, Magnetohydrodynamics (39) (2003) 77–83.

[81] D. Eberbeck, F. Wiekhorst, U. Steinhoff, L. Trahms, Aggregation behaviour of magnetic nanoparticle suspensions investigated by magnetorelaxometry, Journal of Physics: Condensed Matter 18 (38) (2006) S2829–S2846.

[82] F. Ludwig, E. Heim, M. Schilling, K. Enpuku, Characterization of superparamagnetic Fe[sub 3]O[sub 4] nanoparticles by fluxgate magnetorelaxometry for use in biomedical applications, Journal of Applied Physics 103 (7) (2008) 07A314.

[83] E. A. Heim, Fluxgate-Magnetrelaxometrie magnetischer Nanopartikel in der Bioanalytik, Ph.D. thesis, mbv, Mensch-und-Buch-Verl., Berlin (2009).

[84] G. Wu, Assay development: fundamentals and practices, Wiley, Hoboken, N.J, 2010.

[85] F. W. Scheller, U. Wollenberger, A. Warsinke, F. Lisdat, Research and development in biosensors, Current Opinion in Biotechnology 12 (1) (2001) 35–40.

[86] D. R. Thévenot, K. Toth, R. A. Durst, G. S. Wilson, Electrochemical biosensors: recommended definitions and classification, Biosensors and Bioelectronics 16 (1-2) (2001) 121–131.

[87] A. P. F. Turner, Biosensors: sense and sensibility, Chemical Society Reviews 42 (8) (2013) 3184.

[88] C. Johnson, N. L. Adolphi, K. L. Butler, D. M. Lovato, R. Larson, P. D. Schwindt, E. R. Flynn, Magnetic relaxometry with an atomic magnetometer and SQUID sensors on targeted cancer cells, Journal of Magnetism and Magnetic Materials 324 (17) (2012) 2613–2619.

[89] N. L. Adolphi, K. S. Butler, D. M. Lovato, T. E. Tessier, J. E. Trujillo, H. J. Hathaway, D. L. Fegan, T. C. Monson, T. E. Stevens, D. L. Huber, J. Ramu, M. L. Milne, S. A. Altobelli, H. C. Bryant, R. S. Larson, E. R. Flynn, Imaging of Her2-targeted magnetic nanoparticles for breast cancer detection: comparison of SQUID-detected magnetic

relaxometry and MRI, Contrast Media & Molecular Imaging 7 (3) (2012) 308–319.

[90] S.-H. Chung, M. Grimsditch, A. Hoffmann, S. D. Bader, J. Xie, S. Peng, S. Sun, Magneto-optic measurement of Brownian relaxation of magnetic nanoparticles, Journal of Magnetism and Magnetic Materials 320 (3-4) (2008) 91–95.

[91] C. C. Yang, S. Y. Yang, H. H. Chen, W. L. Weng, H. E. Horng, J. J. Chieh, C. Y. Hong, H. C. Yang, Effect of molecule-particle binding on the reduction in the mixed-frequency alternating current magnetic susceptibility of magnetic bio-reagents, Journal of Applied Physics 112 (2) (2012) 024704.

[92] S. Y. Yang, C. C. Yang, H. E. Horng, B. Y. Shih, J. J. Chieh, C. Y. Hong, H. C. Yang, Experimental Study on Low-Detection Limit for Immunomagnetic Reduction Assays by Manipulating Reagent Entities, IEEE Transactions on NanoBioscience 12 (2) (2013) 65–68.

[93] P. I. Nikitin, P. M. Vetoshko, T. I. Ksenevich, New type of biosensor based on magnetic nanoparticle detection, Journal of Magnetism and Magnetic Materials 311 (1) (2007) 445–449.

[94] H.-J. Krause, N. Wolters, Y. Zhang, A. Offenhäusser, P. Miethe, M. H. Meyer, M. Hartmann, M. Keusgen, Magnetic particle detection by frequency mixing for immunoassay applications, Journal of Magnetism and Magnetic Materials 311 (1) (2007) 436–444.

[95] S. Schrittwieser, F. Ludwig, J. Dieckhoff, A. Tschoepe, A. Guenther, M. Richter, A. Huetten, H. Brueckl, J. Schotter, Direct Protein Detection in the Sample Solution by Monitoring Rotational Dynamics of Nickel Nanorods, Small 10 (2) (2014) 407–411.

[96] T. Aytur, J. Foley, M. Anwar, B. Boser, E. Harris, P. R. Beatty, A novel magnetic bead bioassay platform using a microchip-based sensor for infectious disease diagnosis, Journal of Immunological Methods 314 (1-2) (2006) 21–29.

[97] P. Hawkins, R. Luxton, Magnetic Nanoparticles in Immunoassays, in: Magnetic nanoparticles: from fabrication to clinical applications: theory to therapy, chemistry to clinic, bench to bedside, CRC Press, Boca Raton, FL, 2012, pp. 243–276.

[98] H. Bannwarth, B. P. Kremer, A. Schulz, Basiswissen Physik, Chemie und Biochemie, Springer Berlin Heidelberg, Berlin, Heidelberg, 2013.

[99] M. O'Connell, B. Belanger, P. Haaland, Calibration and assay development using the four-parameter logistic model, Chemometrics and Intelligent Laboratory Systems 20 (2) (1993) 97–114.

[100] J. N. Weiss, The Hill equation revisited: uses and missuses, The FASEB Journal 11 (11) (1997) 835–841.

[101] M. I. Shliomis, Effective viscosity of magnetc suspensions, Soviet Physics JETP 34 (6).

[102] K. Keshoju, H. Xing, L. Sun, Magnetic field driven nanowire rotation in suspension, Applied Physics Letters 91 (12) (2007) 123114.

[103] M. I. Shliomis, Ferrohydrodynamics: retrospective and issues, in: Ferrofluids: magnetically controllable fluids and their applications, Springer, New York, 2002, pp. 85–111.

[104] M. I. Shliomis, Comment on "magnetoviscosity and relaxation in ferrofluids", Physical Review E 64 (6).

[105] M. A. Martsenyuk, Y. L. Raikher, M. I. Shliomis, On the kinetics of magnetization of suspensions of ferromagnetic particles, Soviet Physics JETP 38 (2) (1974) 413.

[106] Y. L. Raikher, M. I. Shliomis, The Effective Field Method in the Orientational Kinetics of Magnetic Fluids and Liquid Crystals, in: W. Coffey (Ed.), Advances in Chemical Physics, Vol. 87, John Wiley & Sons, Inc., Hoboken, NJ, USA, 1994, pp. 595–751.

[107] T. Yoshida, K. Enpuku, J. Dieckhoff, M. Schilling, F. Ludwig, Magnetic fluid dynamics in a rotating magnetic field, Journal of Applied Physics 111 (5) (2012) 053901.

[108] V. M. Zaitsev, M. I. Shliomis, Entrainment of ferromagnetic suspension by a rotating field, J. Appl. Mech. Tech. Phys. 10 (5).

[109] L. Sun, K. Keshoju, H. Xing, Magnetic field mediated nanowire alignment in liquids for nanocomposite synthesis, Nanotechnology 19 (40) (2008) 405603.

[110] H. Lamb, Hydrodynamics, Dover Publications, New York, 1945.

[111] J.-C. Bacri, R. Perzynski, M. Shliomis, G. Burde, "Negative-viscosity" effect in a magnetic fluid, Physical Review Letters 75 (11) (1995) 2128–2131.

[112] B. M. Heegaard, J.-C. Bacri, R. Perzynski, M. I. Shliomis, Magneto-vortical birefringence in a ferrofluid, Europhysics Letters (EPL) 34 (4) (1996) 299–304.

[113] J. Embs, H. Müller, C. Wagner, K. Knorr, M. Lücke, Measuring the rotational viscosity of ferrofluids without shear flow, Physical Review E 61 (3) (2000) R2196–R2199.

[114] M. I. Shliomis, T. P. Lyubimova, D. V. Lyubimov, Ferrohydrodynamics: an essay on the progress of ideas, Chemical Engineering Communications 67 (1) (1988) 275–290.

[115] H. C. Weng, C.-K. Chen, M.-H. Chang, Magnetoviscosity in magnetic fluids: testing different models of the magnetization equation, Smart Science 1 (1) (2013) 51–58.

[116] J. Dieckhoff, M. Schilling, F. Ludwig, Fluxgate based detection of magnetic nanoparticle dynamics in a rotating magnetic field, Applied Physics Letters 99 (11) (2011) 112501.

[117] M. Wang, G. Uhlenbeck, On the Theory of the Brownian Motion II, Reviews of Modern Physics 17 (2-3) (1945) 323–342.

[118] V. I. Klyatskin, Stochastic equations through the eye of the physicist basic concepts, exact results and asymptotic approximations, Elsevier, Amsterdam; Boston, 2005.

[119] W. T. Coffey, P. J. Cregg, Y. U. P. Kalmykov, On the Theory of Debye and Néel Relaxation of Single Domain Ferromagnetic Particles, in: I. Prigogine, S. A. Rice (Eds.), Advances in Chemical Physics, Vol. 83, John Wiley & Sons, Inc., Hoboken, NJ, USA, 1992, pp. 263–464.

[120] D. Meeker, Finite Element Method Magnetics 4.2, http://www.femm.info (2014).

[121] R. Kröger, R. Unbehauen, Elektrodynamik, Teubner, Stuttgart, 1993.

[122] J. Dieckhoff, A. Lak, M. Schilling, F. Ludwig, Protein detection with magnetic nanoparticles in a rotating magnetic field, Journal of Applied Physics 115 (2) (2014) 024701.

[123] Bartington Instruments Limited, http://www.bartington.com (2011).

[124] P. Ripka (Ed.), Magnetic sensors and magnetometers, Artech House remote sensing library, Artech House, Boston, 2001.

[125] H. W. Ott, Noise reduction techniques in electronic systems, 2nd Edition, Wiley, New York, 1988.

[126] R. Rosensweig, J. Popplewell, R. Johnston, Magnetic fluid motion in rotating field, Journal of Magnetism and Magnetic Materials 85 (1-3) (1990) 171–180.

[127] B. H. McNaughton, K. A. Kehbein, J. N. Anker, R. Kopelman, Sudden Breakdown in Linear Response of a Rotationally Driven Magnetic Microparticle and Application to Physical and Chemical Microsensing, The Journal of Physical Chemistry B 110 (38) (2006) 18958–18964.

[128] A. V. Lebedev, A. Engel, K. I. Morozov, H. Bauke, Ferrofluid drops in rotating magnetic fields, New Journal of Physics 5 (2003) 57–57.

[129] E. Huber, M. Urban, Helmholtzspulen zur Kalibrierung von Magnetfeldsensoren, Wissenschaftliche Berichte / Forschungszentrum Karlsruhe, Karlsruhe, 1995.

[130] N. M. Markiewicz, Automatisierte Probenpositionierung für die Untersuchung magnetischer Nanopartikel im rotierenden Magnetfeld, Bachelorarbeit, Institut für Elektrische Messtechnik und Grundlagen der Elektrotechnik, Technische Universität Braunschweig (2013).

[131] A. Streibel, Temperaturabhängigkeit magnetischer Nanopartikel im rotierenden Magnetfeld, Bachelorarbeit, Institut für Elektrische Messtechnik und Grundlagen der Elektrotechnik, Technische Universität Braunschweig (2014).

[132] National Instruments, http://www.ni.com (2014).

[133] A. V. Oppenheim, R. W. Schafer, J. R. Buck, Discrete-time signal processing, Prentice Hall, Upper Saddle River, N.J., 1999.

[134] D.-X. Chen, V. Skumryev, B. Bozzo, Calibration of ac and dc magnetometers with a Dy2o3 standard, Review of Scientific Instruments 82 (4) (2011) 045112.

[135] D.-X. Chen, C. Gu, AC susceptibilities of conducting cylinders and their applications in electromagnetic measurements, IEEE Transactions on Magnetics 41 (9) (2005) 2436–2446.

[136] H. Remmer, Spektroskopie magnetischer Nanopartikel - Charakterisierung des Messaufbaus und Anwendung in der Bioanalytik, Bachelorarbeit, Institut für Elektrische Messtechnik und Grundlagen der Elektrotechnik, Technische Universität Braunschweig (2010).

[137] M. Hoyer, Messaufnehmer für den Rotationsfeld-Nanopartikel-Analysator, Bachelorarbeit, Institut für Elektrische Messtechnik und Grundlagen der Elektrotechnik, Technische Universität Braunschweig (2014).

[138] F. Adunka, Messunsicherheiten: Theorie und Praxis, 3rd Edition, Vulkan-Verl, Essen, 2007.

[139] micromod Partikeltechnologie GmbH, http://www.micromod.de (2014).

[140] K. Enpuku, T. Tanaka, T. Matsuda, F. Dang, N. Enomoto, J. Hojo, K. Yoshinaga, F. Ludwig, F. Ghaffari, E. Heim, M. Schilling, Properties of magnetic nanoparticles in the Brownian relaxation range for liquid phase immunoassays, Journal of Applied Physics 102 (5) (2007) 054901.

[141] A. Günther, P. Bender, A. Tschöpe, R. Birringer, Rotational diffusion of magnetic nickel nanorods in colloidal dispersions, Journal of Physics: Condensed Matter 23 (32) (2011) 325103.

[142] Ocean NanoTech, http://www.oceannanotech.com (2014).

[143] C. Nguyen, F. Desgranges, G. Roy, N. Galanis, T. Maré, S. Boucher, H. Angue Mintsa, Temperature and particle-size dependent viscosity data for water-based nanofluids – Hysteresis phenomenon, International Journal of Heat and Fluid Flow 28 (6) (2007) 1492–1506.

[144] P. Bender, A. Günther, A. Tschöpe, R. Birringer, Synthesis and characterization of uniaxial ferrogels with Ni nanorods as magnetic phase, Journal of Magnetism and Magnetic Materials 323 (15) (2011) 2055–2063.

[145] H. Liu, N. Pierre-Pierre, Q. Huo, Dynamic light scattering for gold nanorod size characterization and study of nanorod–protein interactions, Gold Bulletin 45 (4) (2012) 187–195.

[146] R. Kötitz, W. Weitschies, L. Trahms, W. Brewer, W. Semmler, Determination of the binding reaction between avidin and biotin by relaxation measurements of magnetic nanoparticles, Journal of Magnetism and Magnetic Materials 194 (1-3) (1999) 62–68.

[147] U. Hartmann, H. Mende, Experimental investigation of Néel relaxation effects on magnetostatic properties of a ferrofluid, Journal of Magnetism and Magnetic Materials 45 (2-3) (1984) 409–414.

[148] J. Dieckhoff, T. Yoshida, K. Enpuku, M. Schilling, F. Ludwig, Homogeneous Bioassays Based on the Manipulation of Magnetic Nanoparticles by Rotating and Alternating Magnetic Fields - A Comparison, IEEE Transactions on Magnetics 48 (11) (2012) 3792–3795.

[149] J. Dieckhoff, M. Schilling, F. Ludwig, Magnetic marker based homogeneous bioassays utilizing rotating magnetic fields, Journal of Applied Physics 115 (17) (2014) 17B304.

[150] J. Dieckhoff, S. Schrittwieser, J. Schotter, H. Remmer, M. Schilling, F. Ludwig, Single-core magnetic markers in rotating magnetic field based homogeneous bioassays and the law of mass action, Journal of Magnetism and Magnetic Materials 380 (2015) 205–208.

[151] K. Saha, F. Bender, E. Gizeli, Comparative Study of IgG Binding to Proteins G and A: Nonequilibrium Kinetic and Binding Constant Determination with the Acoustic Waveguide Device, Analytical Chemistry 75 (4) (2003) 835–842.

[152] H. Fischer, I. Polikarpov, A. F. Craievich, Average protein density is a molecular-weight-dependent function, Protein Science 13 (10) (2009) 2825–2828.

[153] T. Krouglova, J. Vercammen, Y. Engelborghs, Correct Diffusion Coefficients of Proteins in Fluorescence Correlation Spectroscopy. Application to Tubulin Oligomers Induced by Mg2+ and Paclitaxel, Biophysical Journal 87 (4) (2004) 2635–2646.

[154] C. Röcker, M. Pötzl, F. Zhang, W. J. Parak, G. U. Nienhaus, A quantitative fluorescence study of protein monolayer formation on colloidal nanoparticles, Nature Nanotechnology 4 (9) (2009) 577–580.

[155] H. Remmer, J. Dieckhoff, M. Schilling, F. Ludwig, Suitability of magnetic single- and multi-core nanoparticles to detect protein binding with dynamic magnetic measurement techniques, Journal of Magnetism and Magnetic Materials 380 (2015) 236–240.

[156] V. Ludovini, S. Gori, M. Colozza, L. Pistola, E. Rulli, I. Floriani, E. Pacifico, F. R. Tofanetti, A. Sidoni, C. Basurto, A. Rulli, L. Crino, Evaluation of serum HER2 extracellular domain in early breast cancer patients: correlation with clinicopathological parameters and survival, Annals of Oncology 19 (5) (2008) 883–890.

[157] J. Salazar, M. S. Martínez, M. Chávez, A. Toledo, R. Añez, Y. Torres, V. Apruzzese, C. Silva, J. Rojas, V. Bermúdez, C-Reactive Protein: Clinical and Epidemiological Perspectives, Cardiology Research and Practice 2014 (2014) 1–10.

[158] M. Beković, M. Trlep, M. Jesenik, A. Hamler, A comparison of the heating effect of magnetic fluid between the alternating and rotating magnetic field, Journal of Magnetism and Magnetic Materials 355 (2014) 12–17.

List of Figures

List of Tables

Acknowledgments

I would like to thank all the people that contributed to my work and supported me during my time as a PhD student at the Institut für elektrische Messtechnik and Grundlagen der Elektrotechnik.

First, I would like to thank Prof. Dr. Meinhard Schilling, the head of the department, and especially Dr. Frank Ludwig for giving me the opportunity to work as a scientific research assistant on this fascinating topic in the course of the NAMDIATREAM project. I was given the opportunity to conduct this research under their advice with a lot of freedom for own ideas while significantly increasing my knowledge.

The NAMDIATREAM project was funded by the European Community's 7th Framework Programme under grant number n° NMP4-LA-2010-246479.

I would like to thank my project partners for the fruitful collaborations that we had throughout this interdisciplinary project. Especially, I thank Jörg Schotter and Stefan Schrittwieser from the Austrian Institute of Technology (Vienna, Austria) for the discussions, the support and the organization of our project. It was every time a pleasure to work with them and I appreciate their great hospitality and the time besides the project work. Furthermore, I acknowledge the support from Frauke Alves and Julia Bode from the Max Planck Institute for Experimental Medicine (Göttingen, Germany) for their biological advice and antibody support.

I would like to thank Prof. Keiji Enpuku and especially Dr. Takashi Yoshida from Kyushu University (Fukuoka, Japan) for our fruitful collaboration. Dr. Takashi Yoshida performed the numerical solution of the FPE and developed the empirical model.

I would like to thank Andreas Hütten from Bielefeld University for examining my PhD thesis and Prof. Erwin Peiner from Technische Universität Braunschweig for leading the examination board.

I would like to thank Dr. Dietmar Eberbeck and Dr. Sibylle Sievers from Physikalisch-Technische Bundesanstalt for the magnetization curve measurements.

I would like to thank Dr. Andreas Tschöpe and his group from Saarland University (Saarbrücken, Germany) for the nanorod supply.

I acknowledge the nanoparticle support from Cordula Grüttner and micromod Partikeltechnologie GmbH (Rostock, Germany), the team from Ocean NanoTech (San Diego, CA, USA) as well as Nicole Gehrke and nanoPET Pharma GmbH (Berlin, Germany).

Many thanks go to the members of my department for the discussions and support. Especially, I thank my friend Aidin Lak for the time we could spent together to elaborate on our research ideas and results, support each other and discover the life outside the department. Furthermore, I thank Jan M. Scholtyssek for the TEM images, Hilke Remmer for our collaborations and Thilo Viereck, Erik Heim, Christian Kuhlmann and Christof Wehrmann for their technical advices. For the administrative and media related support I thank Gabriele Weise, Gabriela Kurbach, Kerstin Franke, Ralf Behme, Tanja Coenen and Georg Dornig. In addition, I specially acknowledge the mechanical work performed by Harald Schmidt, Hartmut Müller, Jan Pförtner and the workshop trainees.

I also thank Lutz Hermann, Sebasitan Stankowitz, Nicolai Markiewicz, Christos Itsios, Alexander Streibel and Mark Hoyer who I could supervise throughout their theses and in return supported me by improving the RMF measurement system and conducting helpful investigations.

I acknowledge the allowance of AIP Publishing LLC, ELSEVIER and IEEE to reuse my published results in my PhD thesis.

Finally I would like to thank my family, friends and girl friend for their support and patience. Especially, I thank Laura and Tobi.